NTNU – Trondheim
Norwegian University of
Science and Technology

Wind-induced Dynamic Response and Aeroelastic Stability of a Suspension Bridge crossing Sognefjorden

Trine Hollerud Odden
Henrik Skyvulstad

Civil and Environmental Engineering (2 year)
Submission date: June 2012
Supervisor: Ole Andre Øiseth, KT
Co-supervisor: Ragnar Sigbjörnsson, KT

Norwegian University of Science and Technology
Department of Structural Engineering

Department of Structural Engineering

Faculty of Engineering Science and Technology

NTNU- Norwegian University of Science and Technology

ACCESSIBILITY

Open

MASTER THESIS 2012

SUBJECT AREA:	DATE:	NO. OF PAGES:
Dynamic of structures	11.07.2012	18+72+24

TITLE:

Wind-induced dynamic response and aeroelastic stability of a suspension bridge crossing Sognefjorden

Vindindusert dynamisk respons og aeroelastisk stabilitet av hengebro over Sognefjorden

BY:

Trine Hollerud Odden and Henrik Skyvulstad

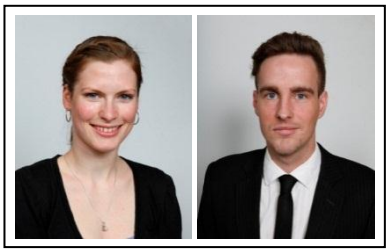

SUMMARY: This thesis is a feasibility study, with regards to aerodynamic stability, about the possibility of constructing a suspension bridge with a main span of 3700m over the Sogne Fjord in Norway. The design wind velocity for the Sogne Bridge is 64.2 m/s.
A preliminary design is conducted to find the approximate dimensions for the bridge models with different cross sections. These bridges are then modeled in Abaqus in order to find the natural frequencies, vibration modes and mass properties.
The key to calculating the critical velocity of the models is to include the aerodynamic derivatives of the cross sections. A Matlab program has the aerodynamic derivatives, natural frequencies, vibration modes and mass properties as input. With this information the program is able to calculate the multimode flutter velocity of the models.
Also, a response calculation is executed in order to see how the different models behave under serviceability wind velocity. This gives a better picture of which models are most applicable.
The results show that to apply a slotted box girder improves the flutter velocity, and all the models with this type of cross-section have a stability limit above the design velocity. For a single box girder, the structural measure of using a mono-cable instead of the traditional two-cable bridge geometry increases the critical wind velocity to above the design velocity. All the models satisfy the serviceability response requirements.

RESPONSIBLE TEACHER: Ole Øiseth

SUPERVISOR(S) Ole Øiseth, Ragnar Sigbjörnsson

CARRIED OUT AT: NTNU Department of Structural Engineering

Masteroppgave våren 2012 for stud. techn. Trine Hollerud Odden og Henrik Skyvulstad:

Vindindusert dynamisk respons og aeroelastisk stabilitet av hengebro over Sognefjorden
Wind-induced dynamic response and aeroelastic stability of a suspension bridge crossing Sognefjorden

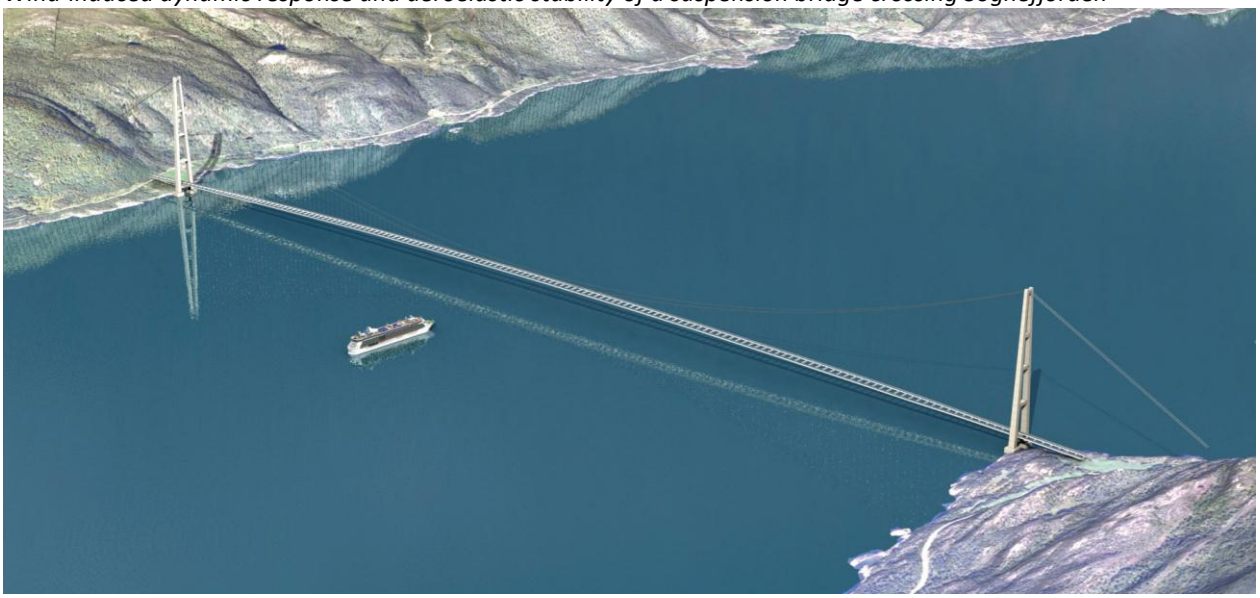

Statens vegvesen planlegger en ombygning av E39 slik at det blir mulig å reise fra Trondheim til Kristiansand ferjefritt. Dette innebærer at det skal bygges en rekke brokonstruksjoner. En av disse bruene vil krysse Sognefjorden. Denne oppgaven dreier seg om hengebroalternativet.

Oppgavens formål er å:
- Utføre overslagsdimensjonering av en hengebro over Sognefjorden
- Bestemme den vindinduserte dynamiske responsen for den valgte utformingen
- Bestemme den aeroelastiske stabilitetsgrensen.

Løsningen av oppgaven bør inneholde følgende:
- Valg av tverrsnittsform og søk i litteraturen etter lastkoeffisienter og aerodynamiske deriverte.
- Overslagsdimensjonering av konstruksjonen.
- Etablering av en abaqus modell
- Bestemmelse av egenfrekvenser og svingeformer
- Beregning av aeroelastisk stabilitetsgrense
- Beregning av vindindusert dynamisk respons i frekvens eller tidsplanet.

Oppgaven skal utføres i henhold til retningslinjer for utførelse av prosjektoppgave ved Institutt for konstruksjonsteknikk (se Instituttets hjemmeside).

Faglærer: Ole Andre Øiseth
Veiledere: Ragnar Sigbjörnsson
Besvarelsen skal leveres til Institutt for konstruksjonsteknikk innen 11. juni 2012.

Ole Andre Øiseth
Faglærer

Abstract

This thesis is a feasibility study, with regards to aerodynamic stability, about the possibility of constructing a suspension bridge with a main span of 3700m over the Sogne Fjord in Norway. The design wind velocity for the Sogne Bridge is 64.2 m/s.

A preliminary design is conducted to find the approximate dimensions for the bridge models with different cross sections. These bridges are then modeled in Abaqus in order to find the natural frequencies, vibration modes and mass properties.

The key to calculating the critical velocity of the models is to include the aerodynamic derivatives of the cross sections. A Matlab program has the aerodynamic derivatives, natural frequencies, vibration modes and mass properties as input. With this information the program is able to calculate the multimode flutter velocity of the models.

Also, a response calculation is executed in order to see how the different models behave under serviceability wind velocity. This gives a better picture of which models are most applicable.

The results show that to apply a slotted box girder improves the flutter velocity, and all the models with this type of cross-section have a stability limit above the design velocity. For a single box girder, the structural measure of using a mono-cable instead of the traditional two-cable bridge geometry increases the critical wind velocity to above the design velocity. All the models satisfy the serviceability response requirements.

Sammendrag

Denne masteroppgaven er en mulighetsstudie rundt aerodynamisk stabilitet i sammenheng med å bygge en hengebru med et hovedspenn på 3700m for å krysse Sognefjorden. Dimensjonerende vindhastighet for Sognebrua er 64.2 m/s.

En overslagsdimensjonering er utført for å finne dimensjonene for brumodellene med ulike kassetverrsnitt. Disse modellene er modellert i Abaqus for å finne egenfrekvenser, svingemoder og massestørrelser.

Nøkkelen for å beregne kritisk vindhastighet for modellene av Sognebrua er å inkludere de aerodynamiske deriverte tilhørende de ulike kassetverrsnittene. Et Matlab program som kan regne ut ved hvilken vindhastighet et instabilitetsfenomen kalt flutter oppstår, har de aerodynamiske deriverte, egenfrekvensene, svingemodene og massestørrelsene som inndata. Med denne informasjonen er programmet i stand til å regne seg fram til den kritiske vindhastigheten på grunn av multimode flutterinstabilitet.

Det er også utført responsberegninger på de ulike brumodellene. Disse resultatene gir et bedre bilde på hvilke modeller som er mest anvendbare til videre arbeid.

Resultatene viser at å anvende et delt kassetverrsnitt for brubanen forbedrer den kritiske flutterhastigheten, og alle modellene med denne type tverrsnitt har en stabilitetsgrense over den dimensjonerende vindhastigheten. For et enkelt kassetverrsnitt kan det bygnings-messige tiltaket ved å konstruere en monokabel istedenfor den tradisjonelle to-kabel utformingen øke den kritiske vindhastigheten til over den dimensjonerende. Alle modellene tilfredsstiller bruksgrensekravene for respons.

Preface

We would like to thank Associate Professor Ole Andre Øiseth, Associate Professor Anders Rönnquist and Professor Ragnar Sigbjörnsson for their open doors and guidance. Special thanks to Ole Andre Øiseth for letting us use his multimode-flutter calculation program.

We would also like to thank Statens Veivesen for providing us the computational report of the Hardanger Bridge and the wind-tunnel test results for Brusymfonien.

Henrik Skyvulstad and Trine Hollerud Odden

Table of Contents

List of figures

FIGURE 6.20 SPECTRAL ACCELERATION DENSITY FOR VERTICAL DIRECTION, AT MID-SPAN FOR V=30 M/S, HM 67

List of tables

1 Introduction

Statens Veivesen is conducting a feasibility study regarding the possibility of crossing the Sogne Fjord without ferries. This thesis focuses on the alternative of constructing a suspension bridge with a main span of 3700m. Because of the depth of the fjord the pylons supporting the bridge have to be placed ashore. The longest suspension bridge built today is the Akashi Kaikyo Bridge in Japan, with a main span of 1991m. If the Sogne Bridge is built, it would represent an increase of span length by a factor of 1.86.

One of the main structural challenges for a super slender suspension bridge is the aerodynamic stability, and one of the biggest fears for bridge engineers is the dynamic instability phenomenon called flutter that can occur at high wind velocities. Flutter happens because of coupling between vibration-modes. Coupling occurs due to the motion-induced effects caused by the motion of the structure when it is subjected to strong wind. The famous collapse of Tacoma Bridge happened because of flutter. The consequence of structural failure of a super structure like a long-spanned suspension bridge represents an economic catastrophe, so flutter has been one of the main research topics in relation to increasing the span of suspension bridges. There are two main ways to improve the aerodynamic stability of a suspension bridge; structural improvements and aerodynamic improvements. For the latter, the aerodynamic characteristics of the bridge girder play a significant role.

The approach used to find the dynamic design forces and the serviceability of a structure is calculating the response with buffeting theory. For the design forces, the displacements need to be found, and for the serviceability both displacements and acceleration of the structure is needed. The buffeting theory is based on a handful of simplifications that make the calculation of response easier. Vortex shedding is not included.

The objective of this thesis is to find the wind-induced dynamic response and the aeroelastic stability of a suspension bridge crossing the Sogne Fjord.

The first stage of this thesis is to conduct a literary study to find an appropriate type of cross section with aerodynamic derivatives. The bridge is then modeled in Abaqus in order to obtain the vibration modes, natural frequencies and mass properties of the structure. Six different bridge models are then created. A Matlab program is made to help make these models. The program generates the layout of the bridge with a few input parameters. The structural properties obtained from Abaqus are used in other Matlab programs that calculate the critical velocity and the response in frequency domain for the models. The Matlab programs use the aerodynamic derivatives of the cross-sections. A Matlab program provided by Ole Øiseth is used to calculate multimode flutter. A two-mode flutter program is also made to understand the solving of flutter equations and verify the results from the multimode flutter program. A response program is made to calculate the dynamic response of the models in frequency domain. The static wind response from the mean wind velocity is

calculated in Abacus. The responses from the different cross-sections are tested against serviceability requirements.

This report starts with an introduction of the theory used throughout this thesis. The theory in the second chapter involves aerodynamic derivatives, aerodynamic instabilities and buffeting response. In chapter three the preliminary design of the bridge alternatives are carried out and the chosen cross-sections for the models are presented. These cross-sections include a single box section and three different slotted box sections. The aerodynamic measures applied to the models include using a slotted box girder, adding guide vanes to the cross-section and having a vertical plate in between the two box girders. For structural improvements a mono cable is applied to two of the models. The aerodynamic derivatives and the static force coefficients for the different girder sections are put forth at the end of the chapter. In the fourth chapter the modeling choices for the Abaqus models are described. Here, the way to describe the mass and stiffness properties are presented, and the simplifications of the models are mentioned. How information is transferred between Abaqus and Matlab is also made known in the fourth chapter. The fifth chapter gives a description of the Matlab programs used to calculate critical wind velocity and response. In the sixth chapter the results of the critical velocities and response for all the models are presented and discussed. The last chapter, the seventh, contains a conclusion and suggestions about further work.

2 Theory

All dynamic calculations start with the equation of motion. This is an equilibrium equation according to Newton's second law. For a structure with one degree of freedom the equation of motion is given by equation (2.1).

$$m\ddot{r}(t) + c\dot{r}(t) + kr(t) = p(t) \tag{2.1}$$

Here m is the mass, c the damping and k the stiffness property, r is the displacement as a function of time and the dots represent time derivatives; one dot gives the velocity and two dots the acceleration. p(t) is the external force on the system (Chopra, 2007). By assuming $r=a_r e^{i\omega t}$, $p=a_p e^{i\omega t}$ and dividing on k ($k=\omega_n^2 * m$), equation (2.1) is transformed to (2.2).

$$\begin{gathered}(-\frac{\omega^2}{\omega_n^2} + 2i\varsigma\frac{\omega}{\omega_n} + 1)a_r = \hat{H}(\omega)^{-1}a_r = a_{\hat{p}} \\ a_r = \hat{H}(\omega)a_{\hat{p}}\end{gathered} \tag{2.2}$$

Here ω_n is the natural frequency of the system, ω is the varying circular frequency dependent on the load and ζ is the damping ratio. From equation (2.2) it is clear that when $\omega=\omega_n$, $\hat{H}(\omega)$ is only limited by the damping term from growing to infinity. When $\hat{H}(\omega)$, the frequency-response-function, grows to infinity the response will get very large and the phenomenon known as resonance occurs.

The buffeting theory is applied to describe the wind forces on the structure. The wind load equals the p(t) term in equation (2.1). The general assumptions are that the bridge can be considered a line-like structure, the wind field is stationary and homogenous and it is possible to divide the wind load in a mean part and a fluctuating part. The fluctuating part of the wind is considered small compared to the mean wind; the same goes for the structural displacements and rotations. It is assumed that the wind load on the structure can be calculated from the instantaneous velocity pressure, giving the equations in (2.3).

$$\begin{aligned}q_D(x,t) &= \frac{1}{2}\rho V_{rel}^2 \cdot D \cdot C_D(\alpha) \\ q_L(x,t) &= \frac{1}{2}\rho V_{rel}^2 \cdot B \cdot C_L(\alpha) \\ q_M(x,t) &= \frac{1}{2}\rho V_{rel}^2 \cdot B^2 \cdot C_M(\alpha)\end{aligned} \tag{2.3}$$

Here q is the total drag, lift and moment forces in y, z and θ direction, respectively, see figure 2.1. x gives the location in the longitudinal direction of the structure, ρ is the air density, and D and B the height and width of the girder section. $V_{rel}{}^2 = (V+u-\dot{y})^2 + (w-\dot{z})^2$ is the felt wind on the structure where V is the mean wind velocity, u and w is the fluctuating wind velocity (see figure 2.1), and $\dot{y}$ and $\dot{z}$ are the velocity of the structure. C_i are the static

load coefficients given by the outline of the cross section; these are a function of the attack angle of the oncoming flow, α (Strømmen, 2010).

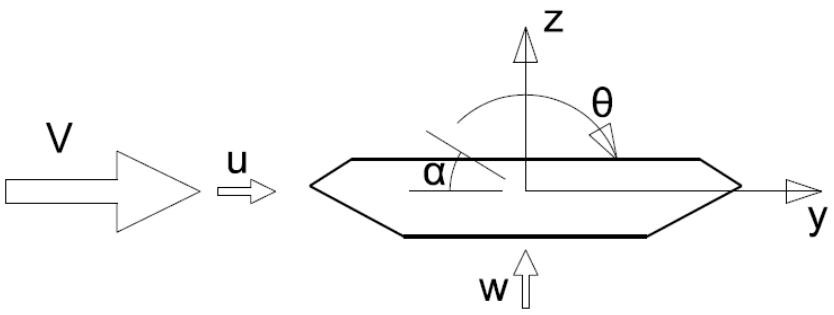

Figure 2.1. The oncoming wind direction and orientation of the cross section.

There are two linearization assumptions for the load:

1. Since it is assumed that the fluctuating components and the structures velocity are small compared to the mean wind velocity, all the second order terms with a combination of these values are considered negligible.
2. The static load coefficients can be describes in a linearized manner:

$$C_i(\alpha) = C_i(\bar{\alpha}) + \alpha_f \cdot C_i'(\bar{\alpha}) \text{ where i=D,L or M} \qquad \textbf{(2.4)}$$

α is the angle of incidence, $\bar{\alpha}$ is the mean value of angle of incidence, and $\alpha_f = \theta + w/V - \dot{z}/V$ is the fluctuating part of the angle of incidence.

From the assumptions above the load can be divided into a mean (static) load and a dynamic load. The dynamic load consists of a part associated with turbulence and a motion-induced part associated with the displacement and velocity of the structure itself, see equation (2.5) (Strømmen, 2010).

$$\begin{aligned}\mathbf{q}_{tot} &= \begin{bmatrix}\bar{q}_y \\ \bar{q}_z \\ \bar{q}_\theta\end{bmatrix} + \begin{bmatrix}q_y(x,t) \\ q_z(x,t) \\ q_\theta(x,t)\end{bmatrix} = \bar{\mathbf{q}} + \mathbf{B}_q \cdot \begin{bmatrix}u(x,t) \\ w(x,t)\end{bmatrix} + \mathbf{C}_{ae} \cdot \begin{bmatrix}\dot{y}(x,t) \\ \dot{z}(x,t) \\ \dot{\theta}(x,t)\end{bmatrix} + \mathbf{K}_{ae} \cdot \begin{bmatrix}y(x,t) \\ z(x,t) \\ \theta(x,t)\end{bmatrix} \\ &= \frac{\rho V^2}{2}\begin{bmatrix}D\bar{C}_D \\ B\bar{C}_L \\ B^2\bar{C}_M\end{bmatrix} + \frac{\rho V}{2}\begin{bmatrix}2D\bar{C}_D & DC_D' - B\bar{C}_L \\ 2B\bar{C}_L & BC_L' + D\bar{C}_D \\ 2B^2\bar{C}_M & B^2C_M'\end{bmatrix}\begin{bmatrix}u(x,t) \\ w(x,t)\end{bmatrix} \\ &- \frac{\rho V}{2}\begin{bmatrix}2D\bar{C}_D & DC_D' - B\bar{C}_L & 0 \\ 2B\bar{C}_L & BC_L' + d\bar{C}_D & 0 \\ 2B^2\bar{C}_M & B^2C_M' & 0\end{bmatrix}\begin{bmatrix}\dot{y}(x,t) \\ \dot{z}(x,t) \\ \dot{\theta}(x,t)\end{bmatrix} + \frac{\rho V^2}{2}\begin{bmatrix}0 & 0 & DC_D' \\ 0 & 0 & BC_L' \\ 0 & 0 & B^2C_M'\end{bmatrix}\begin{bmatrix}y(x,t) \\ z(x,t) \\ \theta(x,t)\end{bmatrix}\end{aligned} \qquad \textbf{(2.5)}$$

If a person rides a bicycle in a mean wind velocity of 10 m/s and he rides the bike at 10 m/s, the person would not feel any wind. This phenomenon is taken into account with the aerodynamic damping and stiffness.

When calculating the response of the structure, all the force components in equation (2.5) must be taken into account, but when calculating the critical velocity for the structure, only the motion induced variables need to be considered. In the buffeting theory quasi-static values may be used, these are functions of the static load coefficients, but as will be seen later in this chapter, a better approximation for the motion induced loads are needed at high velocities.

2.1 Aeroelastic stability

The change in static and dynamic response will normally be fairly proportional with increasing mean wind velocity, but at some critical wind velocity, the change in response will increase rapidly for small changes in the mean wind velocity. This may be identified as an instability limit.

The motion induced instabilities can be described mathematically by the impedance matrix, see equation (2.6). When the determinant of the impedance matrix becomes zero, the response goes towards infinity. The impedance matrix is derived from the equation of motion. It is the same principle as shown in equation (2.2), but with more degrees of freedom and with the aerodynamic forces included in the load term.

$$\hat{\mathbf{E}}_{\eta}(\omega,V)=\left[\mathbf{I}-\boldsymbol{\kappa}_{ae}-\left(\omega\cdot diag\left[\frac{1}{\omega_i}\right]\right)^2+2i\omega\cdot diag\left[\frac{1}{\omega_i}\right]\cdot(\zeta-\zeta_{ae})\right] \qquad \textbf{(2.6)}$$

Here $\boldsymbol{\kappa}_{ae}$ is the aerodynamic stiffness matrix divided by the structural stiffness matrix and $\boldsymbol{\zeta}_{ae}$ is the aerodynamic damping ratio matrix. In order to explain the different stability limits it is necessary to look into the motion induced contribution that must be included in the equation of motion when the structural system is subjected to strong wind.

2.1.1 Motion induced effects

When a slender structure is subjected to strong wind, it will be set in motion. This motion will interact with the wind flow and alter the load on the structure. A challenge with dynamic calculations of structures subjected to wind load is that there is no perfect formula for describing the motion induced forces. Dissimilar cross sections will behave differently to the same wind load due to different outlines. This is because the air flow around the cross section is influenced by the outline and the movement of the structure. The aerodynamic derivatives are used to describe the dynamic behavior of different cross sections subjected to wind. These parameters are described below.

2.1.2 Aerodynamic derivatives

The theory of aerodynamic derivatives (AD) is developed through the study of the behavior of a thin airfoil subjected to wind (Scanland RH, 1971).The structural properties, stiffness (K-K_{ae}) and damping (C-C_{ae}), will change as a function of the wind velocity. The change in mass properties is considered negligible. This gives a change to the natural frequencies ($\omega(V)^2=K_{tot}/M$) and the mode shapes. As a consequence the response of a structure subjected to wind cannot be calculated correctly with the still air structural properties. The content of the aerodynamic stiffness matrix and damping matrix are given by the aerodynamic derivatives. There are 18 ADs, P_i*, H_i* and A_i*, i=1,2…6. P* is related to the equilibrium equation in horizontal direction, H* to the vertical direction and A* to the rotation.

$$C_{ae} = \frac{\rho B^2}{2}\omega \begin{bmatrix} P_1^* & P_5^* & BP_2^* \\ H_5^* & H_1^* & BH_2^* \\ BA_5^* & BA_1^* & B^2A_2^* \end{bmatrix} \quad \textbf{(2.7)}$$

$$K_{ae} = \frac{\rho B^2}{2}\omega^2 \begin{bmatrix} P_4^* & P_6^* & BP_3^* \\ H_6^* & H_4^* & BH_3^* \\ BA_6^* & BA_4^* & B^2A_3^* \end{bmatrix} \quad \textbf{(2.8)}$$

The theory developed to calculate the ADs is based on a specific section, a thin airfoil, and this theory does not directly apply to other cross sections with different shapes. To obtain better results for calculations of critical wind velocity, a better approximation is needed. This is possible through wind tunnel tests of relevant cross-section models.

It is feasible to obtain eight ADs through wind tunnel tests, Ai* and Hi*, i=1,2,3,4. These are associated with the vertical and torsional degrees of freedom. A1* and A4* give the contribution from the vertical movement to the torsional response, while H2* and H3* give the contribution from torsional movement to vertical response, see equation (2.9) and (2.10) (Matsumoto, 2004).

$$L = \frac{1}{2}\rho BV^2\left(kH_1^*\frac{\dot{z}}{V} + kH_2^*\frac{B\dot{\theta}}{V} + k^2H_3^*\theta + k^2H_4^*\frac{z}{B}\right) \quad \textbf{(2.9)}$$

$$M = \frac{1}{2}\rho B^2V^2\left(kA_1^*\frac{\dot{z}}{V} + kA_2^*\frac{b\dot{\theta}}{V} + k^2A_3^*\theta + k^2A_4^*\frac{z}{b}\right) \quad \textbf{(2.10)}$$

Here L represents the lift force in the vertical direction while M is the moment force in torsion. z is the vertical displacement and θ the torsional rotation. The dots symbolize time

derivatives. ω is the circular frequency, ρ is the air density, B is the girder width, k is the reduced frequency (= Bω/V) and V is the mean wind velocity.

To test a girder section in a wind tunnel, the sections being tested are scaled down. To apply the test results to a for a full size bridge, the aerodynamic derivatives are obtained as a function of the reduced velocity, Vred=V/(ωB). With the reduced velocity the aerodynamic derivatives for a specific section can be applied to a sized up mode,l using the velocity, frequency and width for that particular model.

The reason only eight of the eighteen aerodynamic derivatives are found through wind tunnel tests, is because of the difficulty of simulating the horizontal vibration in the wind tunnel. All the P*s are related to the dynamic force equilibrium in horizontal direction, and $H_{5,6}$* and $A_{5,6}$* give the contribution from horizontal movement to vertical and torsional response, respectively. The usual approach for including the P*s, $H_{5,6}$* and $A_{5,6}$* is to calculate them with quasi static theory, that means they are expressed with static force coefficients. The quasi-static aerodynamic stiffness and damping matrixes are given in equation (2.5).

Several studies have been carried out to find out how much the different aerodynamic derivatives influence the flutter velocity. It is now agreement on that H1*, A1*, A2*, A3* and H3* are the most influential (Ole Øiseth, 2011), (Matsumoto, 2008). One study concludes that A1 is the most important aerodynamic derivative to stabilize the coupled flutter instability (Matsumoto, 2008). The role of the different aerodynamic derivatives according to a Step-by-Step analysis developed by Matsumoto is shown in (Trein, 2011).

Table 2.1. Role of the aerodynamic derivatives in coupled flutter, according to step-by-step analysis.

Derivative	Stabilization	Destabilization
A_1*	Low absolute values	High absolute values
A_2*	Negative values	Positive values
A_3*	Low absolute values	High absolute values
H_1*	Negative values	Positive values, low absolute values
H_3*	Low absolute values	High absolute values
A_1*×H_3*	Negative values	Positive values

Since the use of aerodynamic derivatives is developed through the airfoil theory, the same theory applied on a slotted box section can give uncertain results. There will be more turbulence around a slotted box section than a thin airfoil or a streamlined single box because of the slot. It is therefore not given that the same approach on this type of cross-sections will render as good results as for a single streamlined cross-section.

2.1.3 Flutter

Flutter is an aeroelastic instability phenomenon at high wind velocities where coupling effects between two or more vibration modes makes them interact and the structure starts to oscillate. The two main modes that interact are usually the lowest symmetrical vertical mode and the lowest torsional mode. The critical velocity is found by setting the determinant of the impedance matrix, equation (2.6), equal to zero. The coupling occurs via the off diagonal terms in $\boldsymbol{\kappa}_{ae}$, se equation (2.11). Shape-wise similarity and the separation of the natural frequencies are important for the modes to couple (Øiseth R. S., Volume 98, Issue 12, December 2010,). Equation (2.11) shows that the off diagonal terms will be zero for no shape-wise similarity, giving no coupling between the modes. The aerodynamic contribution to the impedance matrix comes from the motion induced load given in equation (2.9) and (2.10). The terms multiplied with displacement and rotation give the aerodynamic stiffness matrix, while the terms multiplied with the time derivatives of the displacement and rotation give the aerodynamic damping matrix.

$$\begin{aligned}
\kappa_{aezz} &= \frac{\rho B^2}{2\tilde{m}_z}\left(\frac{\omega_r}{\omega_z}\right)^2 H_4^* \frac{\int_{L\exp} \phi_z^2 dx}{\int_L \phi_z^2 dx}, \quad \kappa_{aez\theta} = \frac{\rho B^3}{2\tilde{m}_z}\left(\frac{\omega_r}{\omega_z}\right)^2 H_3^* \frac{\int_{L\exp} \phi_z \phi_\theta dx}{\int_L \phi_z^2 dx} \\
\kappa_{ae\theta z} &= \frac{\rho B^3}{2\tilde{m}_\theta}\left(\frac{\omega_r}{\omega_\theta}\right)^2 A_4^* \frac{\int_{L\exp} \phi_\theta \phi_z dx}{\int_L \phi_\theta^2 dx}, \quad \kappa_{ae\theta\theta} = \frac{\rho B^4}{2\tilde{m}_\theta}\left(\frac{\omega_r}{\omega_\theta}\right)^2 A_3^* \frac{\int_{L\exp} \phi_\theta^2 dx}{\int_L \phi_\theta^2 dx}
\end{aligned} \tag{2.11}$$

The aerodynamic derivatives in the damping- and stiffness matrixes are functions of the mean wind velocity, this gives that also the natural frequency is a function of the mean wind velocity and the flutter calculation will need iterations. This gives a new equation system for every step in the velocity. The solution of this equation system will give new modes and natural frequencies from the updated eigenvalue solution. The flutter velocity is reached when the solution of the equation system includes a mode that has zero damping. From the coupling terms, interaction effects between the vertical mode and torsional mode will influence this new mode that is mainly torsional movement, but also have some vertical movement contribution. The more shape-wise similar the starting modes are, the more they will interact.

Bi-modal flutter

The bi-modal flutter calculation uses the assumption of pure one-directional mode shapes. Since the impedance matrix in general contains complex values, setting the determinant of the impedance matrix to zero implies setting the real part and the imaginary part of the determinant equal to zero:

$$\left|\det(\hat{\mathbf{E}}_\eta(\omega,V))\right| = 0 \qquad \textbf{(2.12)}$$

$$\mathrm{Re}(\det(\hat{\mathbf{E}}_\eta)) = 0 \text{ and } \mathrm{Im}(\det(\hat{\mathbf{E}}_\eta)) = 0 \qquad \textbf{(2.13)}$$

After the assumption of bi-modal flutter with one-directional mode-shapes the solution is greatly simplified, making it possible to calculate the imaginary and real roots of the determinant directly. The roots will vary with both mean wind and eigenfrequencies so iterations are needed. The simplifications of bi-modal flutter enable the roots to be plotted in a 2D diagram dependent on eigenfrequency and mean wind. The imaginary roots and real roots have the same value when they intersect, making the determinant of the impedance matrix zero. The intersection at the lowest mean wind velocity gives the critical flutter velocity. All the other intersections are only theoretical and will never occur in real life.

Multimode flutter

For multimode flutter calculation, the flutter velocity is reached when the real part of S goes to zero, that means when the total damping of a mode is zero, see equation (2.14). S is the eigenvalue for a mode, found from the homogenous solution to the equation of motion when assuming the solution can be written as $r(t)=e^{St}$ (Chopra, 2007). Since the motion-induced forces are associated with the vibration of the structure, they are included in the homogenous solution. The particular solution from the wind-flow will only give a small contribution to the total response compared to the motion induced response close to an instability limit, and is not necessary to include when finding the critical velocity.

$$S = -\zeta_n\omega_n \pm i\omega_n\sqrt{1-\zeta_n^{\,2}}, \qquad \omega_n = |S|, \qquad \zeta_n = \frac{\mathrm{Re}(S)}{|S|} \qquad \textbf{(2.14)}$$

Here ω_n is the natural frequency of the n-th vibration mode dependent on the aerodynamic derivatives and wind velocity, ζ_n is the damping ratio of the n-th mode including both structural and aerodynamic damping and i is the imaginary unit. When the real part of S is zero, the total damping of the mode is zero, and there is nothing to dissipate the energy given to the structure from the load. Since the wind specter contains values for all frequencies a mode with zero damping will always experience resonanse.

The solution of a two mode eigenvalue problem, equation (2.14), for a 1000 m bridge for increasing wind velocities is plotted in figure 2.2 and figure 2.3 with a Matlab program that can calculate multimode flutter by the eigenvalue solution. The still air mode shapes are assumed as two perfect half sinusoidal shapes, pure torsional and pure vertical. This means they are completely shape-wise similar. The torsional still air natural frequency is 2 rad/s and the vertical 1 rad/s. The aerodynamic derivatives are taken from the cross section of the Hardanger Bridge. The imaginary part of the eigenvalue shows how the eigenfrequencies

changes, the “torsional” mode loses stiffness with increasing velocities and as a result the frequency decreases. The vertical mode has a quite constant value, but since the imaginary part of the eigenvalues includes the square root term with the damping properties of the mode, the imaginary part decreases when the damping increases as shown in figure 2.3. The damping of the “torsional” mode goes to zero at a velocity of 74 m/s. This gives no resistance in the structure to the load matching the eigenfrequency of this mode, and the bridge will eventually collapse from the forces in the bridge given by the big displacements. The critical flutter frequency can be found in figure 2.2, the value at the end of the red graph will only represent the circular frequency since the damping is zero, see equation (2.14). If altering the torsional natural frequency to 1.5 rad/s, the same example as above gives a critical velocity of 54 m/s. This shows the influence of the natural frequency separation for the flutter velocity.

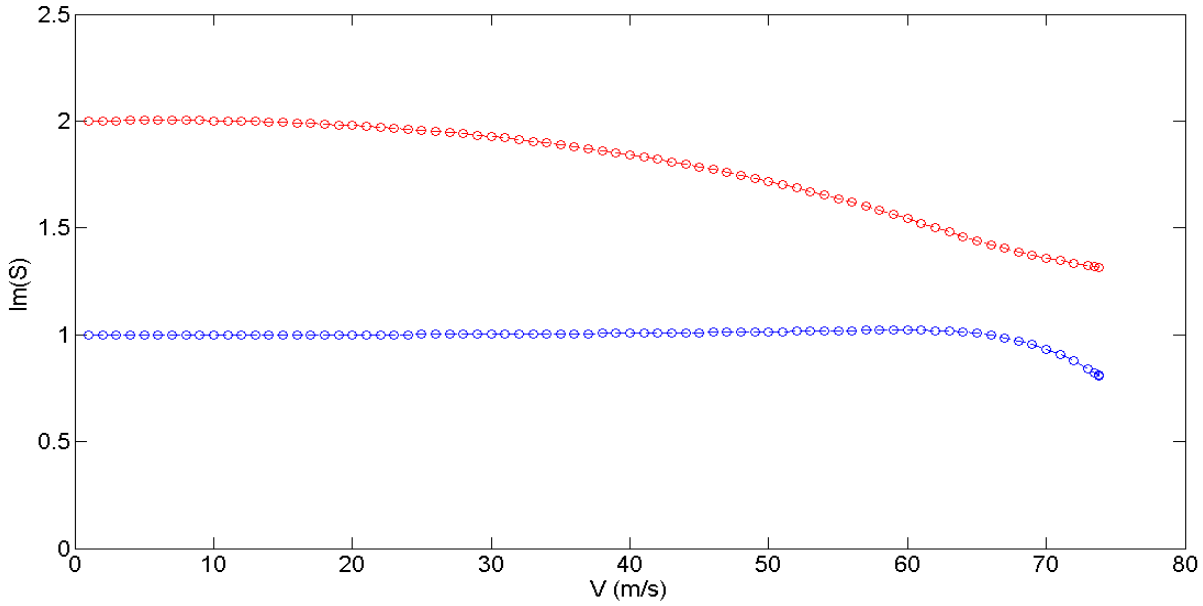

Figure 2.2 The imaginary parts of the eigenvalues (frequencies)

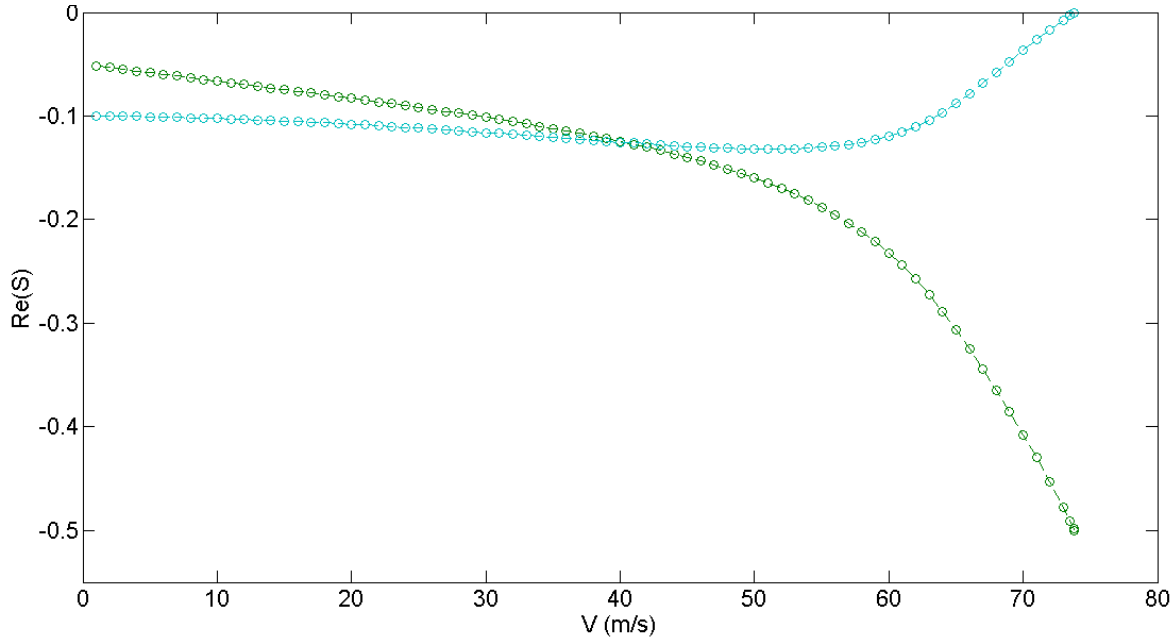

Figure 2.3 The real parts of the eigenvalues (damping)

From the study of the critical flutter velocity of the Hardanger Bridge, it is shown that the lowest flutter velocity is found with a combination of three modes (Ole Øiseth, 2011). With the bimodal flutter-routine derived from the impedance matrix, it is only possible to calculate for two modes and the critical velocity found would not be correct.

2.1.4 Other motion induced instabilities

Static divergence

Static divergence is, as the name states, a static instability limit making the critical frequency zero, $\omega_r = \omega_\theta(V_{cr}) = 0$. This is an instability limit that uses a vibrational mode predominantly in torsion. What happens is that the structure loses its torsional stiffness due to interaction with the wind. From the expression for the circular frequency, $\omega_r^2 = K_{tot}/M$, the circular frequency is zero with no stiffness K_{tot}. K_{tot} includes both structural and aerodynamic stiffness. This reduces the impedance matrix (2.6) to equation (2.15).

$$\hat{\mathbf{E}}_\eta(\omega_r = 0, V_{cr}) = \mathbf{I} - \boldsymbol{\kappa}_{ae} \qquad \textbf{(2.15)}$$

The critical velocity is found when equation (2.15) goes to zero. $\boldsymbol{\kappa}_{ae}$ is $\mathbf{K}_{ae}$ given in equation (2.8) divided by the structural stiffness matrix. The value for A_3^* has to be positive for static divergence to occur. The aerodynamic derivatives from quasi-static theory are applicable since it is a purely static instability problem (Strømmen, 2010), that means that the aerodynamic stiffness matrix from equation (2.5) applies.

Galloping

In galloping the mode shape of interest is predominantly in the vertical direction. Galloping can be described as a type of single-vertical-mode flutter.

The critical frequency is the same as the eigenfrequency for the lowest vibrational mode shape in vertical direction. It is important to remember that this eigenfrequency is not constant any more, it is a function of the velocity. $\omega_r = \omega_z(V_{cr})$, where ω_r is the critical frequency. When only considering a vertical vibration mode, the impedance matrix is reduced to equation (2.16).

$$\hat{\mathrm{E}}_{\eta}(\omega_r, V_{cr}) = 1 - \kappa_{aezz} - \left(\frac{\omega}{\omega_z}\right)^2 + 2 \cdot i(\zeta_z - \zeta_{aezz}) \cdot \frac{\omega}{\omega_z} \qquad \textbf{(2.16)}$$

Setting the real and imaginary parts of the impedance matrix equal to zero and making the wind exposed part the same as the entire span gives the resonance frequency in equation (2.17).

$$\omega_r = \omega_z \left(1 + \frac{\rho B^2}{2\tilde{m}_z} H_4^*\right)^{-1/2} \qquad \textbf{(2.17)}$$

The critical frequency is reached when the damping properties are as shown in equation (2.18), giving zero total damping.

$$\zeta_z = \zeta_{aezz} = \frac{\rho B^2}{4\tilde{m}_z} \cdot \frac{\omega_r}{\omega_z} H_1^* \qquad \textbf{(2.18)}$$

The total damping must be zero for galloping to occur, this means that galloping can only happen for H_1^* grater that zero. For streamlined cross sections, H_1^* is negative and galloping will not occur (Strømmen, 2010).

Dynamic stability limit in torsion

The dynamic stability limit in torsion is similar to galloping; the only difference is that the mode shape is in torsion. This can be considered as a type of single-torsional-mode flutter. The impedance matrix is then reduced to equation (2.19).

$$\hat{\mathrm{E}}_{\eta}(\omega_r, V_{cr}) = 1 - \kappa_{ae\phi\phi} - \left(\frac{\omega}{\omega_\phi}\right)^2 + 2 \cdot i(\zeta_z - \zeta_{ae\phi\phi}) \cdot \frac{\omega}{\omega_\phi} \qquad \textbf{(2.19)}$$

As with galloping, the critical velocity is found when the total damping is zero. The critical frequency is given in equation (2.20) and the damping at the stability limit is given in equation (2.21).

$$\omega_r = \omega_\theta \left(1 + \frac{\rho B^4}{2\tilde{m}_\theta} A_3^*\right)^{-1/2} \qquad \textbf{(2.20)}$$

$$\zeta_\theta = \zeta_{ae\theta\theta} = \frac{\rho B^4}{4\tilde{m}_\theta} \cdot \frac{\omega_r}{\omega_\theta} A_2^* \qquad \textbf{(2.21)}$$

This means that A_2^* has to be positive to give motion induced instability in torsion. With the quasi static theory A_2^* is zero and it is not possible to obtain a stability limit for torsional flutter. For streamlined cross sections A_2^* is negative (Strømmen, 2010).

2.2 Response

Response calculations play an important role in the design of long span bridges. Both ultimate limit state and serviceability limit state uses results from response calculations. The response calculation derived in this chapter uses buffeting theory with aerodynamic derivatives and still-air natural frequencies. Vortex shedding is not included. Since vortex shedding normally dominates the response at low velocities, the response for low wind loads is not accurate.

The aerodynamic derivatives are functions of the reduced velocity, $V_{red}=V/(\omega B)$. V is the mean wind velocity, B the width of the girder and ω is the eigenfrequency of the modes. The aerodynamic derivatives are dependent on ω and change the ω at the same time, implying that iterations are needed. By assuming that the changes in the aerodynamic derivatives for small changes in ω are negligible, no iterations are necessary. This assumption holds for wind velocities up to about half the critical wind velocity.

The fact that the structures experience a small rotation when subjected to the mean wind force is neglected when calculating the response. This gives the assumption that the attack angle of the mean wind is zero degrees.

Max deflections are a tool for designing in ultimate limit state, but will not be considered any further. Deflections and accelerations are important parameters for the serviceability limit state. High accelerations and deflections make the bridge feel unsafe and may make it unusable.

The modal frequency domain approach is used to calculate the deflections. In time domain the response plot looks random, and it is difficult to obtain any information about the structure, like which frequencies dominate the response. When calculating the response in frequency domain the result is more structured and easy to understand. The time domain response can be obtained as a Fourier array of harmonic functions with different frequencies, these functions are added together with a random phase angle which gives the randomness of the time domain plot. The amplitudes of the harmonic functions say how much each piece contributes to the response. It is these pieces that are identified in the frequency domain; the pieces are connected to the different egen-modes and eigenfrequencies of the structure.

The solution in frequency domain is separated in three different calculation procedures, depending on the complexity of the problem (Strømmen, 2010):

1. Single mode single component response. This uses vibrational modes that have one component only, and eigenfrequencies well separated from each other.
2. Single mode three component response. This uses general vibrational modes, but still well separated eigenfrequencies.
3. General multi-mode response. This uses general vibrational modes and coupling effects between the different modes.

The response theory in this chapter is derived using the second solution procedure. Because of the uncoupling of the system the superposition principle applies and the variances from each mode can be summed together:

$$\sigma_n^2 = \sum_{in}^{N} \sigma_{in}^2 \text{ , where n=y,z,θ and i=mode nr.} \quad \textbf{(2.22)}$$

For a given mode shape i, the contribution in time and space is split into 2 parts.

$$\mathbf{r}_i(x,t) = \boldsymbol{\varphi}_i(x) \cdot \eta_i(t) \quad \textbf{(2.23)}$$

Where

$$\boldsymbol{\varphi}_i = \begin{bmatrix} \phi_y(x) \\ \phi_z(x) \\ \phi_\theta(x) \end{bmatrix}_i \quad \textbf{(2.24)}$$

ϕ_{ni} is the shape function in n-direction for mode i and $\eta_i(t)$ is the modal time dependent variable.

The derivation continues with the Fourier transform of the equation of motion. The modal frequency-response-function connects the Fourier amplitude of the time variant part and the Fourier amplitude of the load.

$$a_{\eta_i}(\omega) = \frac{\hat{H}_i(\omega)}{\tilde{K}_i} \cdot a_{\tilde{Q}_i}(\omega) . \quad \textbf{(2.25)}$$

It is further assumed that the motion induced loads are proportional and in phase with the displacement, velocity and acceleration. The loads are named aerodynamic damping, stiffness and mass. Neglecting the aerodynamic mass term and sorting the equations gives the non-dimensional modal frequency-response-function:

$$\hat{H}_i(\omega) = \left[1 - \kappa_{aei} - \left(\frac{\omega}{\omega_i} \right)^2 + 2 \cdot i(\zeta_i - \zeta_{aei}) \cdot \frac{\omega}{\omega_i} \right]^{-1} \quad \textbf{(2.26)}$$

Where

$$\tilde{\mathbf{M}}_i = \int_L (\boldsymbol{\varphi}_i^T \cdot \mathbf{M_0} \cdot \boldsymbol{\varphi}_i) dx \quad \textbf{(2.27)}$$

$$\mathbf{M_0} = diag[m_y(x), m_z(x), m_\theta(x)] \quad \textbf{(2.28)}$$

$$\tilde{\mathbf{C}}_i = 2\tilde{\mathbf{M}}_i \omega_i \zeta_i \quad \textbf{(2.29)}$$

$$\tilde{\mathbf{K}}_i = \omega_i^2 \tilde{\mathbf{M}}_i \tag{2.30}$$

$$\tilde{m}_i = \frac{\tilde{M}_i}{\int_L (\boldsymbol{\varphi}_\mathbf{i}^\mathbf{T} \boldsymbol{\varphi}_\mathbf{i}) dx} \tag{2.31}$$

$$\kappa_{aei} = \frac{1}{\tilde{m}_i} \frac{\int_{L_{\exp}} (\boldsymbol{\varphi}_\mathbf{i}^\mathbf{T} \mathbf{K}_{\mathbf{ae}} \boldsymbol{\varphi}_\mathbf{i}) dx}{\int_L (\boldsymbol{\varphi}_\mathbf{i}^\mathbf{T} \boldsymbol{\varphi}_\mathbf{i}) dx} \tag{2.32}$$

$$\zeta_{aei} = \frac{1}{2\tilde{m}_i} \frac{\int_{L_{\exp}} (\boldsymbol{\varphi}_\mathbf{i}^\mathbf{T} \mathbf{C}_{\mathbf{ae}} \boldsymbol{\varphi}_\mathbf{i}) dx}{\int_L (\boldsymbol{\varphi}_\mathbf{i}^\mathbf{T} \boldsymbol{\varphi}_\mathbf{i}) dx} \tag{2.33}$$

C_{aei} and K_{aei} can be found in section 2.1.2. $\omega_i, \tilde{M}_i$ and $\tilde{K}_i$ are the eigenfrequency, modal mass and modal stiffness of mode i. ζ_i is the modal damping. $m_y(x), m_z(x)$ and $m_\theta(x)$ are the distributed masses in y-, z-, and θ-direction.

The spectral density of the response from mode i at x=x_r is given by,

$$\mathbf{S}_{ri}(x_r, \omega) = \begin{bmatrix} \phi_y^2(x) \\ \phi_z^2(x) \\ \phi_\theta^2(x) \end{bmatrix}_i \cdot \frac{\left|\hat{H}_i(\omega)\right|^2}{\tilde{K}_i^2} \cdot S_{\tilde{Q}_i}(\omega), \tag{2.34}$$

where $S_{\tilde{Q}_i}(\omega)$ is the spectral density of the load and $\phi_i(x_r)$ is the mode shape in horizontal, torsional or vertical direction for mode i at point x=x_r.

The Fourier transform of the fluctuating wind loads in the equation of motion is carried out to find the spectral density of the load. Multiplying the Fourier amplitudes and making the time period, T, go to infinity, using buffeting theory for the wind load and neglecting all cross spectral terms gives:

$$a_{\tilde{Q}_i}(\omega) = \frac{\rho V B}{2} \int_{L\exp} \boldsymbol{\varphi}_i^T (\hat{\mathbf{B}}_q \cdot \mathbf{a}_v) dx \tag{2.35}$$

$$\mathbf{a}_v(x, \omega) = [a_u, a_w]^T \tag{2.36}$$

$$S_{\tilde{Q}_i}(\omega) = \lim_{T \to \infty} \frac{1}{\pi T} (a_{\tilde{Q}_i}^* \cdot a_{\tilde{Q}_i}) \tag{2.37}$$

Here a_u and a_w are the amplitudes of the fluctuating parts and $a_{\tilde{Q}_i}^*$ is the complex conjugated Fourier amplitude of the modal load.

$$S_{\tilde{Q}_i}(\omega) = \left[\frac{\rho V^2 B}{2} \cdot J_i(\omega) \right]^2 \tag{2.38}$$

Where,

$$J_i^2(\omega) = \iint_{L_{\exp}} \boldsymbol{\varphi}_i^T(x_1) \cdot \hat{\mathbf{B}}_q(x_1) \cdot \mathbf{I}_v^2 \cdot \hat{\mathbf{S}}_v(\Delta x, \omega) \cdot \hat{\mathbf{B}}_q^T(x_2) \cdot \boldsymbol{\varphi}_i(x_2) \cdot dx_1 dx_2 \quad \textbf{(2.39)}$$

$$\mathbf{I}_v = diag[I_u, I_w] \quad \textbf{(2.40)}$$

$\hat{\mathbf{B}}_q(x_1) = \mathbf{B_q} \cdot \frac{2}{\rho V B}$, $\mathbf{B_q}$ can be found in equation (2.5). J_i is the joint acceptance function for mode i.

$$\hat{\mathbf{S}}_v(\Delta x, \omega) = diag[S_{uu} / \sigma_u^2, S_{ww} / \sigma_w^2] \quad \textbf{(2.41)}$$

Where,

$$S_{nn}(\Delta x, \omega) \approx S_n(\omega) \cdot \hat{Co}_{uu}(\Delta x, \omega), \text{ n=u or w.} \quad \textbf{(2.42)}$$

$\hat{Co}_{uu}(\Delta x, \omega)$ is the normalized co-spectrum and $S_n(\omega)$ is the spectral density in n direction. To get the variance from the spectral density function, integration over the frequencies is carried out. This gives the final equation for the variance (2.43).

$$\sigma_i^2 = \int_0^\infty S_{ri}(x_r, \omega) d\omega \quad \textbf{(2.43)}$$

The development of these equations and assignment of different coefficients can be found in (Strømmen, 2010). Components of the response calculation is discussed below.

2.2.1 Modal frequency-response-function

To simplify the explanation of the frequency-response-function, aerodynamic stiffness and damping are assumed to be zero.

From equation (2.25), (2.26) and (2.34), it is seen that the modal frequency-response-function says something about how much each mode contributes to the final response. If a harmonic load with only one frequency excites a one degree of freedom system, the frequency-response-function as a function of the load's frequency gives a multiplication factor for the value of the response. If a single harmonic load has a frequency of 2 rad/s and is applied to a structure that has the frequency-response-function shown in figure 2.4, the response will be a harmonic wave with 10 times the amplitude of the load amplitude.

Abs ($\hat{H}_i(\omega)$) is plotted in figure 2.4 for a mode shape with eigenfrequency of 2 rad/s and damping of 0.05. From the figure, the phenomenon of resonance can be seen. At loads with

frequencies close to the eigenfrequency the function becomes large, only limited by the damping. It can be seen from equation (2.26) that if the system is un-damped, the resonant response would go to infinity and the structure collapse. For figure 2.4 it is also seen that loads with higher frequencies than the eigenfrequency of the mode will give small contributions to the modal response, the higher the frequency the smaller the contribution. If the frequency of the load is smaller than the eigenfrequency the function goes to 1. This is called a quasi-static load.

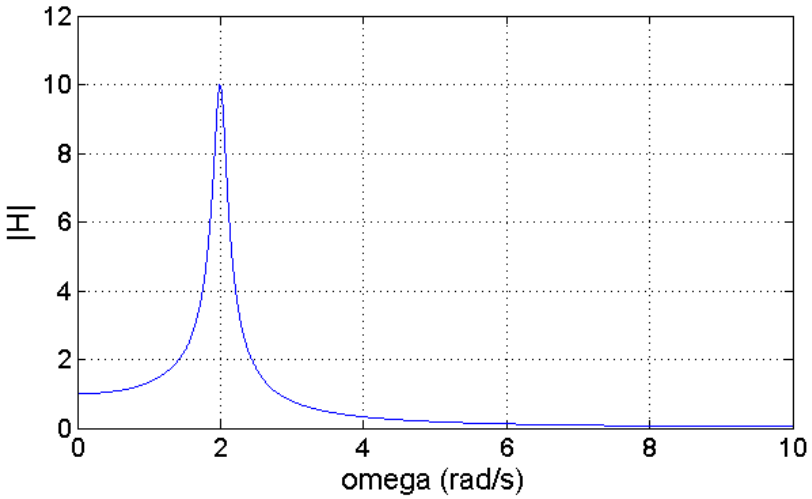

Figure 2.4 Normalized modal frequency-response-function for ω=2 and damping = 0.05

In figure 2.5, the $\sum_i \left|\hat{H}_i(\omega)\right|^2$ is plotted for a three-modal system with eigenfrequencies 1, 3 and 6, with damping 0.05, 0.1, and 0.15. The peaks correspond to the eigenfrequencies, and the height of the peaks clearly depends on the amount of damping.

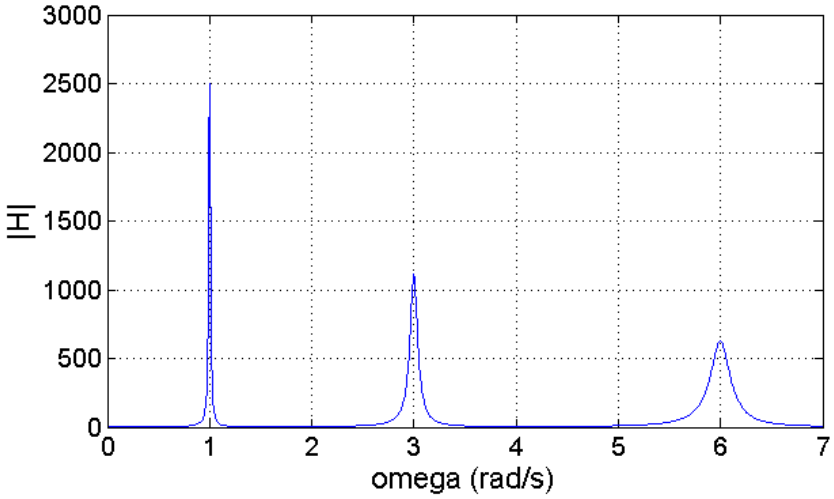

Figure 2.5 Normalized modal frequency-response-function

2.2.2 Spectral density function

The auto spectral density function, $S_x(\omega)$, of a process describes the distribution of the variance contribution at different frequencies (Strømmen, 2010).

$$\sigma_x^2 = \int_0^\infty S_x(\omega) d\omega \,. \tag{2.44}$$

$$S_x(\omega) = \lim_{T\to\infty} \frac{1}{\pi T} \cdot a_x^*(\omega) \cdot a_x(\omega) \,. \tag{2.45}$$

$a_x(\omega)$ is the Fourier amplitude of x.

The time domain transformation is shown under:

$$S_x(\omega_k) = \frac{c_k^2}{2\Delta\omega} \,. \tag{2.46}$$

$$x(t) \approx \sum_{k=1}^{N} x_k \text{ and } x_k = c_k \cos(\omega_k t + \theta_k) \tag{2.47}$$

Equation (2.46) shows that spectral density intervals with high values give a high c_k. The spectral density can be split into different sections with width $\Delta\omega$ and mean value $S(\omega_k)$. The smaller the frequency interval, $\Delta\omega$, the more accurate the response. In equation (2.47) it is shown that the response in time domain is the sum of harmonic functions with amplitudes c_k. From this it is possible to see the connection between the spectral densities of the response in frequency domain with the response in time domain. To find the maximum variance of a process, equations (2.48) and (2.49) applies.

$$\sigma_{xk}^2 = c_k^2 / 2 \tag{2.48}$$

$$\sigma_x^2 = \sum_k \sigma_{xk}^2 \tag{2.49}$$

Equation (2.48) applies for a narrow banded process (Strømmen, 2010). It gives that the total variance of the response is the sum of the amplitudes for the harmonic contributions divided by the square root of two. The total variance is found by an integral over the spectral density function with respect to the frequency.

It is seen from equation (2.34) that the spectral density of the load is proportional to the spectral density of the response, which gives that also the variance of the response is proportional to the spectral densities of the load.

Figure 2.6 shows the spectral density for a mean wind velocity of 30 m/s on the Hardanger Bridge. The directions of the fluctuating wind components, u and w, are shown in figure 2.1.

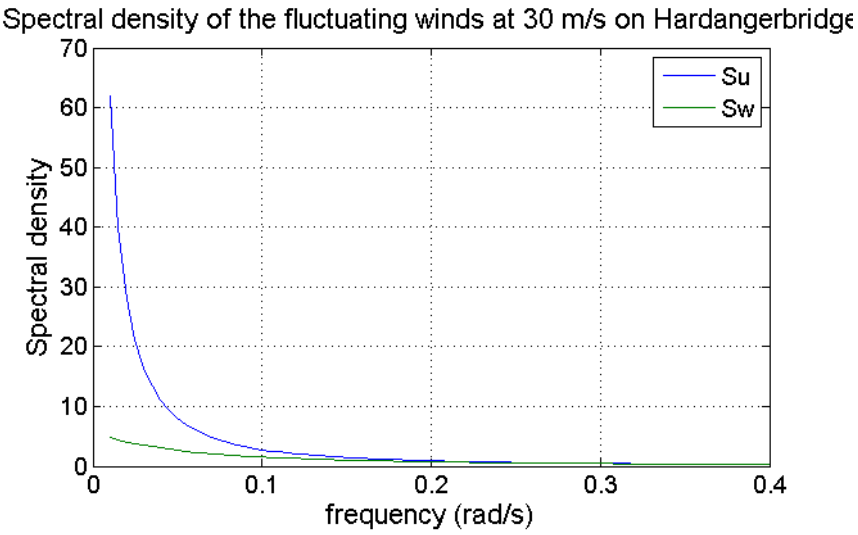

Figure 2.6 Spectral densities for the wind loads on Hardanger Bridge

2.2.3 Aerodynamic stiffness and damping in response calculation

How the aerodynamic stiffness and damping affect the system can be seen from the modal frequency-response-function (2.26). Positive aerodynamic stiffness gives higher response at lower frequencies. Positive aerodynamic stiffness moves the peak of the modal-frequency-response function towards lower frequencies. Positive aerodynamic damping makes the total damping of the system go down. The consequence of lower damping of the system is higher response because of less energy dissipated.

Since the response procedure used is supposed to be uncoupled, the aerodynamic damping matrix $\tilde{C}_{aei}$ and stiffness matrix $\tilde{K}_{aei}$ have to be diagonal. This is a simplification compared to the full multimodal approach.

2.2.4 Joint acceptance function and normalized co-spectrum

Under developing of the spectral density of the load, the Fourier amplitudes of the load are multiplied together in equation (2.44). This gives a double integral over the span called the joint acceptance function (J). After assuming that the cross-spectra between the flow components are zero, the spectral density of the load is given by equations (2.38) - (2.42).

Physical explanations of the joint acceptance function are given under:

- $\hat{\mathbf{B}}_q(x)$ is a matrix with the static force coefficients that says something about how much the fluctuating wind affects the cross-section, or how much energy from the wind load is transferred to the cross-section.
- The normalized co-spectrum distributes the spectral densities of the fluctuating wind over the span. In other words, how much wind is felt a distant Δx from the point evaluated. The shape functions are weighting these distributions.

Figure 2.7 shows the normalized Co-spectrum and illustrates how this spectrum distributes the spectral densities over the span length.

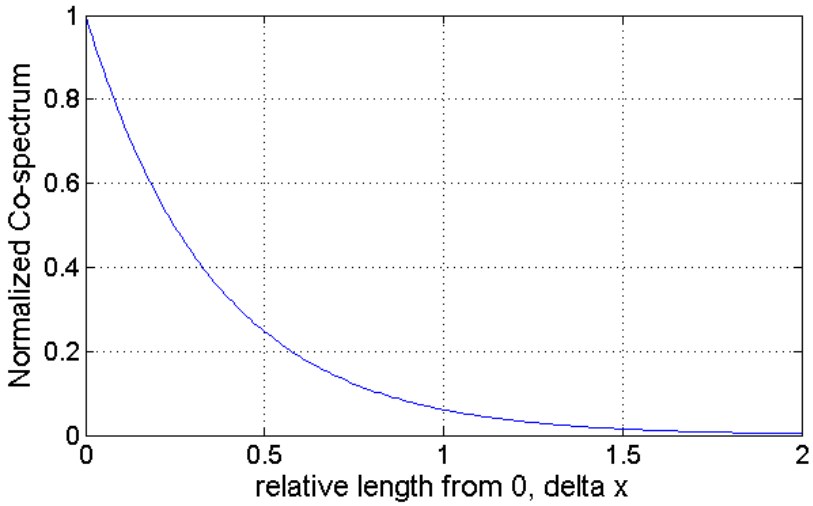

Figure 2.7 Normalized co-spectrum relative from zero

The normalized co-spectrum can have many forms. In this thesis the distribution shown in equation (2.50) is used.

$$\hat{Co}_{nn}(\omega, \Delta x) = \exp(-C_{nx} \cdot \omega \cdot \Delta x / V), \text{ where n=u,w} \qquad \textbf{(2.50)}$$

C_{nx} is a constant that normally has a value between 1.0 and 1.4.

2.2.5 Variance

Wind loads on structures cannot be exactly described by known mathematics. The wind varies randomly and is too complex. This is why statistics is useful for describing the wind field. The wind is assumed stationary over a period of 10 minutes, implying that the mean value of the wind is constant over 10 minutes. In these 10 minutes, the fluctuating part is assumed normally distributed. The way to describe the "wideness" of the normal distribution is by variance. Figure 2.8 shows three normal distributed probability density functions with different variances and mean values.

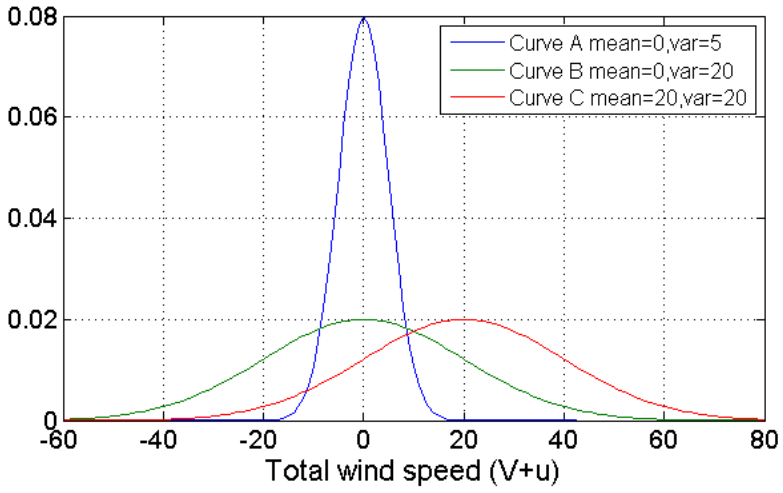

Figure 2.8 Normally distributed probability functions with different variances and mean values.

Note that the areas under the three curves are the same (areas =1). Curve A has relatively small variance which gives a high probability for occurrences of wind velocities near the mean wind velocity. This would imply smaller wind oscillations because the probability of occurrences of high absolute values for the fluctuating wind component (u) is low.

Curve B shows that there is a larger probability for higher values for the fluctuating wind component (u). Curve C has the same variance but a higher mean, this shows that the oscillations are expected to be the same for both curve B and C, the only different is the mean wind, V.

The curve with the biggest variance has more values longer from the mean value. This means that fluctuating wind (with higher variance) will have bigger oscillations.

The load is describes statistically which leads to that the structural displacement also is described statistically. The response of a structure that is loaded with a mean and a fluctuating part will have a mean displacement and a fluctuating displacement. The mean part of the response is the static part and the fluctuating part is the dynamic part.

2.2.6 How many modes to include

In solution procedure 2, the modal response is summed up over all modes, but in practical calculations it is not necessary to include all the modes. This comes from two contributions:

1. The fluctuating wind load has mainly contributions at lower frequencies; this can be seen from figure 2.6 where the spectral densities from the wind have its main contribution up to 0.15 rad/s.

2. For loads (spectral densities) with overweight in relative low frequency range:

   From the expression, $\frac{\phi_i^2(x_r)}{\tilde{K}_i^2} \cdot \left|\hat{H}_i(\omega)\right|^2$ in equation (2.34), it is shown that these factors influence the relationship between the load specter and response specter. Maximum value of the mode shapes are 1 for all modes independent of mode number. The normalized modal frequency-response-function will be 1 for modes with much higher eigenfrequencies than the load (high modes has high eigenfrequencies and the function goes to quasi-static load). The modal stiffness will in general increase for higher modes and reduce the response.

   For loads (spectral densities) with overweight in relative high frequency range:
   The normalized modal frequency-response-function will go towards zero for a load that has a frequency larger than the eigenfrequency of the system.

If contribution 1 and 2 are put together, it is seen that a load specter with low frequencies put together with the high modal stiffness of the higher modes will give low response contributions compared to the lower modes. This is why higher modes can be neglected.

It is important to note that a load with high frequency can give an error in the response calculation when neglecting the modes. This is because a high frequency load can be multiplied by a high normalized modal frequency-response-function making a large contribution to the response. If the high mode shape is poorly damped, the response can become very large.

Example of increasing modal stiffness

To illustrate the increased modal stiffness for higher eigenfrequencies a uniform simply supported beam is evaluated with a modal approach (evenly distributed mass and stiffness). If the boundary condition is put into the equation of motion for the system and taking advantage of the modal orthogonallity; the eigenfrequencies, mode-shapes, modal stiffness and modal masses becomes:

$$\begin{aligned} \omega_n &= \frac{n^2\pi^2}{L^2}\sqrt{\frac{EI}{m}} \\ \phi_n(x) &= \sin\frac{n\pi x}{L} \\ M_n &= \frac{mL}{2} \\ M_n &= \int_0^L m(x)\cdot[\phi(x)]^2 dx \\ K_n &= \omega_n^2 M_n^2 \\ K_n &= \frac{n^2\pi^4 EI}{2L^3} \end{aligned} \qquad \textbf{(2.51)}$$

Here n is the mode nr, I is the second moment of area, E is the modulus of elasticity, m(x) is the distributed mass, M_n is the modal mass, K_n is the modal stiffness, ω_n is the modal eigenfrequency and $\phi_n(x)$ is the mode shape (Chopra, 2007).

The equations in (2.51) show that the modal stiffness increases for higher modes. This effect should in general be expected for line-like structures. This can be explained by the amount of energy needed to deflect a system in different modes. There is less energy needed to deflect a beam like half a sinus-wave than four whole sinus-waves. This is because the curvature needed is grater for the four sinus wave example.

Modal stiffness can be substituted with modal mass and eigenfrequencies ($k=\omega^2 M$). For a rigid body movement, the eigenfrequency is zero, giving zero modal stiffness for this mode. A rigid body movement demands zero energy to be displaced, that fact supports the argument above.

2.2.7 Parameters that influence the dynamic response

Mean wind velocity

Equations (2.38) and (2.43) express that the variance is proportional to the mean wind velocity squared. This should give a perfect quadratic mean wind vs. variance plot, but there are some components that disturb this relation.

Normalized co-spectrum grows for increasing wind velocities. The relative distribution length goes up; this means that it is more likely that two points with distance Δx are experiencing the same wind load when the mean wind velocity is higher.

The aerodynamic derivatives vary with the mean wind velocities, making the response increase or decrease as explained in the aerodynamic derivatives chapter 2.2.3. This effect makes the structure experience motion induced instabilities.

Shape-wise similarity

Variances for the response will in general vary over the structure. This is obvious when the first mode shape is taken into consideration for a simply-supported beam, the variance will be distributed the same way as the mode-shape. This can be seen from equation (2.34). The variance of the displacement will be zero over the supports and maximum at mid-span (assumed a half sinus wave as the first mode shape).

The response calculations are the sum of variances from different modes. If all the mode-shapes for a type of structure have its maximum value at mid-span, the variance at mid-span would be the biggest. For line like structures, this is not the case. Mode-shape two in the horizontal direction is usually one whole sinus wave (anti symmetric mode shape), where the maximum is in the quarter-points, not the midpoint (Chopra, 2007). The variance contribution from this mode in the midpoint is zero.

Eigenfrequencies

The values of the eigenfrequencies influence the response of the structure. If the load applied to a structure contains frequencies close to the egenfrequencies of the structure, the response gets high. An example of this is resonance where a small harmonic load can excite a single mode shape giving the structure high response, even failure. This phenomenon is described in section 2.2.1.

Modal stiffness

As discussed in subsection 2.2.6, higher modal stiffness gives less dynamic response.

Static force coefficients and aerodynamic derivatives

The aerodynamic stiffness and mass alters the modal frequency-response-function as explained in subsection 2.2.3. The values of the static force coefficients influence the response as well. Higher values of the mean static coefficients make the displacements bigger. This can be explained by how much the different turbulence wind components can affect the cross- section. A higher drag coefficient means that the wind that hits the cross-

section will give the structure a higher drag force. With a more streamlined shape, the wind flow will pass more smoothly around the cross-section and the values for the static force coefficients will decrease. As a consequence the fluctuating forces on the cross-section will decrease. This effect is shown in the $\mathbf{B_q}$ matrix in equation (2.5).

2.2.8 Displacement and acceleration limits

Since this thesis focuses on the serviceability wind velocity, serviceability requirements is tested.

1. Max displacement: There are not found any specific standard value for max displacements on bridges, but for different construction materials (wood, steel and concrete) the value varies between L/100 – L/300. ((Standard1995-1-1, 2009) table 7.2)
2. In (Iso6897, 1984) two curves of maximum acceleration for a given frequency are considered the comfort-limit for humans. Curve one is for general purpose buildings, curve two is for fixed offshore structures. Bridges are considered type two structures.

Maximum accelerations are calculated by taking the response spectrum and multiplying it by the frequency to the power of four. This is derived under:

$$x(t) \approx \sum_{k=1}^{N} x_k(t), \quad x_k(t) = c_k \cdot \sin(\omega t + \theta)$$

$$S_x(\omega) = \frac{c_k^2}{2\Delta\omega}$$

$$\ddot{x}(t) = c_k \cdot \omega^2 \sin(\omega t + \theta) \qquad \textbf{(2.52)}$$

$$S_{\ddot{x}}(\omega) = \frac{(c_k \cdot \omega^2)^2}{2\Delta\omega} = \frac{c_k^2 \cdot \omega^4}{2\Delta\omega}$$

It is seen from the derivation in (2.52) that the spectral acceleration is found by dividing the spectral response by the frequency to the power of four. The maximum accelerations are found by finding the max values of the spectral density functions for the response.

2.2.9 Extreme values

Combining static and dynamic response when the dynamic response is represented by a variance is not straight forward. The theory is developed in (Strømmen, 2010). The result is equation (2.53).

$$X_{max} = x_{mean} + k_p * \sigma_x \qquad \textbf{(2.53)}$$

Here X_{max} is the extreme value, x_{mean} is the value from the static load, k_p is the peak factor and σ_x is the variance of the dynamic part. The peak factor varies from 2-5 in fairly broad banded processes, but goes to √2 for ultra-narrow banded processes.

2.2.10 Mono-cable and duo-cable consideration

The mode-shapes from a mono-cable model and a duo-cable model differ because of the different behavior of the systems when the girders are displaced. Figure 2.9 shows the modal coupling effect between horizontal and torsional mode-shapes because of the horizontal displacement of the girder. For a mono-cable model, horizontal displacement of the girder gives a rotation of the girder. It also shows that this is not the case for a bridge with two cables. This is why mono-cables have more coupling between horizontal and torsional mode shapes.

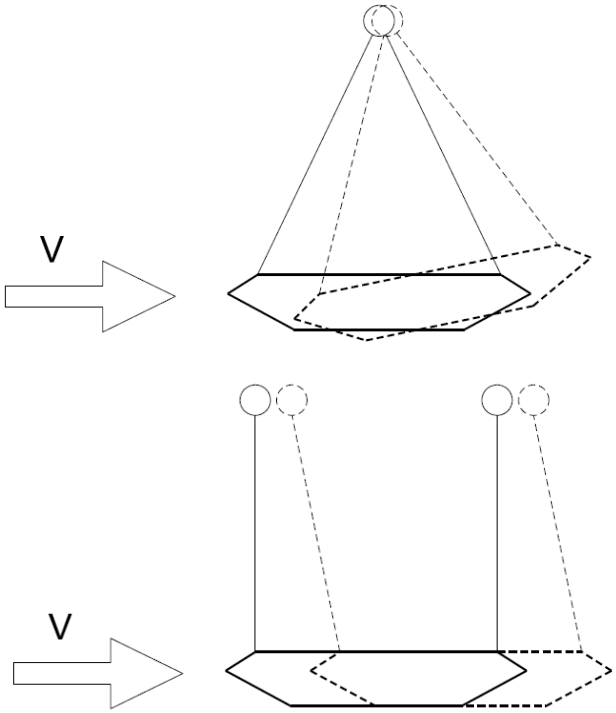

Figure 2.9. Static horizontal displacement of girder for a model with mono cable compared to a two cable model.

For the mono-cable bridge to have a pure torsional mode-shape, the cable has to twist. The duo-cable bridge handle a pure torsional mode-shape by lifting one of the cables and making the other one go down.

Hanger height

The force needed to displace the cables compared to the girder is higher for the cables because higher geometric stiffness. At mid-span the cable and girder are closer together, and with low hanger height the cable and girder will have approximately the same displacement. The stiffness of the cables will contribute to the girder stiffness. This increased stiffness would imply a smoothening of the mode-shapes towards mid-span.

The hanger height will also affect the modal coupling. If the mono-cable is fixed to the girder at mid-span there will be no relative displacement between cable and girder. As can be seen from figure 2.9, it is the relative displacement between cable and girder that gives the rotation of the girder for horizontal displacements.

2.2.11 Multimodal response

The multimodal response is physically more correct than the response calculations described earlier in this chapter. This is because the multimodal approach takes into account all cross-terms that are neglected. This makes the calculations more demanding, but is important if calculating response for higher wind velocities than used in this thesis. This thesis focuses on the serviceability limit state and the procedure used is justified by this:

"The buffeting response is assessed using a multimode and a mode-by-mode approach. The results indicate that the difference between a multimode and a mode-by-mode calculation is negligible when the mean wind velocity is lower than roughly half the stability limit, and that the difference increases with increasing mean wind velocity. The cross-spectral density of the horizontal and vertical component has negligible influence on the torsional response, while the response in the vertical direction is underestimated by 10% at the design mean wind velocity, if this cross-spectral density is not included." (Øiseth S. , 2011, 330)

2.2.12 Turbulence intensity

The turbulence intensity can be explained as the amount of turbulence for a mean wind. The equation for the turbulence intensity is given under:

$$I_i = \frac{\sigma_i}{V} \qquad \text{where i=u, v or w} \qquad \textbf{(2.54)}$$

2.2.13 Static loads

The static wind loads from the buffeting theory are given in equation (2.55).

$$\begin{bmatrix} \bar{q}_y \\ \bar{q}_z \\ \bar{q}_\theta \end{bmatrix} = \frac{\rho V^2}{2} \begin{bmatrix} D\bar{C}_D \\ B\bar{C}_L \\ B^2\bar{C}_M \end{bmatrix} \qquad \textbf{(2.55)}$$

These loads are given per meter, to get the total load the values are multiplied with the length of the bridge exposed to the wind. The static displacements for a structure with many degrees of freedom are normally calculated with an element method program like Abaqus.

3 Models of the Sogne Bridge

To be able to cross the fjord, the Sogne Bridge will have a 3700m main span, see figure 3.1.

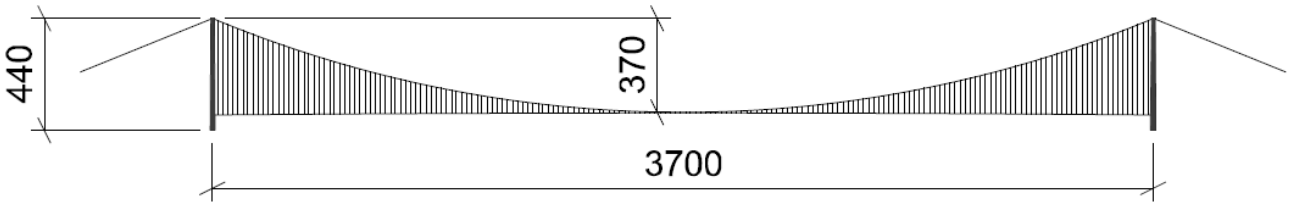

Figure 3.1 Sketch of the Sogne Bridge

Six different bridges are modeled to investigate different solutions and the aerodynamic stability and response of these. The aerodynamic derivatives of the cross-sections have to be known to be able to compute the critical velocity for the bridge models. These can only be obtained through wind tunnel tests, so the cross-sections used in this thesis are limited to those found in the literature with aerodynamic derivatives.

3.1 Choosing cross-sections

The amount of vehicles crossing the Sogne Fjord requires only one lane in each direction, so for practical purposes the girder of the Hardanger Bridge has the optimal size. It is therefore investigated what the stability limit is for that section (H), and if a mono cable can increase the stability limit, see figure 3.2 a).

From studies of aerodynamic stability of suspension bridges, it is found that the traditional suspension bridges with a single box girder seem to be limited to a span of 2000 m. To increase the span for the traditional two-cable suspension bridge, an alternative cross-section with better aerodynamic stability has to be found. With longer span, the torsional stiffness is reduced. A solution with a slotted box girder is proven to give better aerodynamic performance and higher torsional stiffness. These results are obtained through numerical simulations and wind-tunnel testing (Xiang Haifan, 2007). The TF (triangle faring) section has proven good aerodynamic behavior in previous studies (Matsumoto, 2007), and is here applied to the span of the Sogne bridge, see figure 3.2 b). The size of the girder gives three lanes in each direction. Also here the effect of having a mono cable instead of the traditional two cables is tested.

Statens Veivesen has conducted several wind tunnel tests of a slotted box section planned to use on the bridge called Brusymfonien. Two of the alternatives are applied to the Sogne Bridge, one with 20m between the centers of the girders (B20), and one with 30m (B30), see figure 3.2 c) and d).

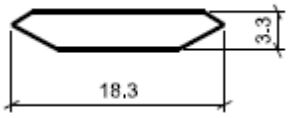

Figure 3.2 a) H and HM

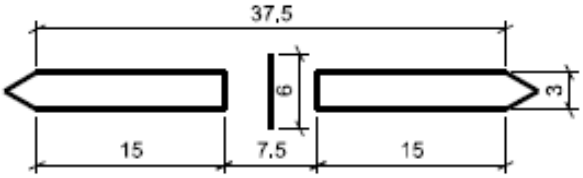

Figure 3.2 b) TF and TFM

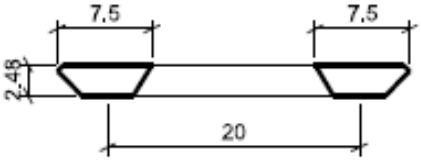

Figure 3.2 c) B20

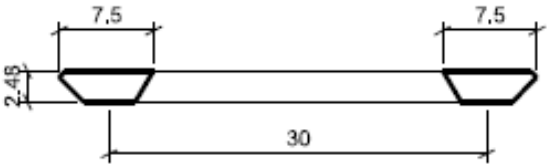

Figure 3.2 d) B30

Figure 3.2 The different cross sections of the chosen bridge girders.

3.2 Preliminary design

In the preliminary design the dimensions of the different bridge alternatives are calculated. The design is superficial. That is because the information and the authors time available is limited, and to dwell on details that may be incorrect serves no purpose in a preliminary phase like this. Only the static load is considered when finding the dimensions of the bridge. The next phase will be to investigate to best solutions from this thesis further, and then look more into the details.

The stiffness properties and yield strengths used for the different components are given in table 3.1, (Vegdirektoratet B. i., 2008):

Table 3.1 Material properties

	E [GPa]	fy [MPa]
Cable	200	1570
Hanger	160	1570
Girder	210	355
Connector beam	210	355
Pylons	40	45

3.2.1 Cross-section

For the models with the box section used on the Hardanger Bridge, all the properties concerning the girder are taken from the computational report of the Hardanger Bridge (Vegdirektoratet B. i., 2008).

For the models TF and TFM, the outline of the slotted box girder from the article, “On the flutter characteristics of separated two box girders” is chosen (Matsumoto, 2007). Then the program Cross X is used to calculate the cross-sectional properties of the slotted box girder, see figure 3.3 (CrossX Version 1.1, 2003). Inside stiffeners are included to prevent buckling of the steel plates. The spacing and shape of the stiffeners are chosen from the design of the Hardanger Bridge girder (Vegdirektoratet B. i., 2011). Values from Cross X give the dead weight of the cross-section that is used for calculation of the hangers and main cables. Additional masses from asphalt, railings and other masses are taken from the computational report of the Hanrdanger Bridge (Vegdirektoratet B. i., 2008). The girder size of the Hardanger Bridge approximately equals the girder size of half of the TF slotted box girder. The loads taken from the Hardanger Bridge is therefore doubled.

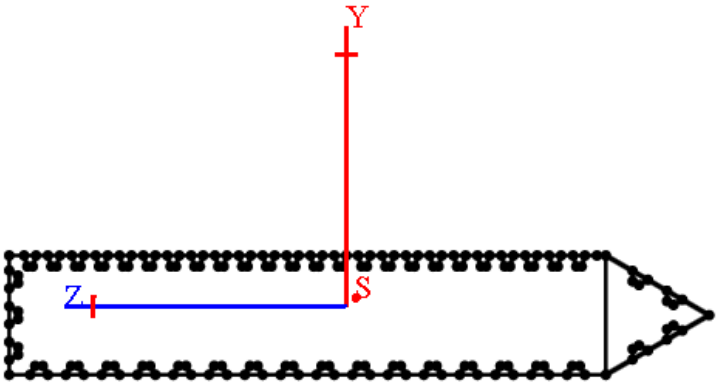

Figure 3.3 Right girder box for the TF section.

For the slotted box girder from Brusymfonien, the same approach as for the TF section is used. The outline of the girder is drawn in CrossX, and stiffeners are applied, see figure 3.4. From this, the sectional properties are calculated. The additional masses are determined from looking at the Hardanger report. The value of the deck mass is reduced due to half the girder with, while the same values are used for railings and similar properties.

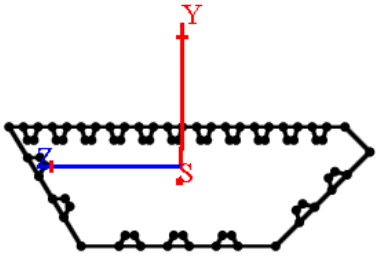

Figure 3.4. Right girder box for the B20 and B30 sections.

The dimensions of the cross beams for the slotted box girders are calculated by assuming that the girder sections connected by the cross-beams are simply supported beams with evenly distributed loads, see figure 3.5. This is conservative since the main parts of the loads are on the girders at the ends. The calculation is given in appendix A2. The cross-section of

the beam has a closed rectangular shape which gives both good resistance against bending and rotation.

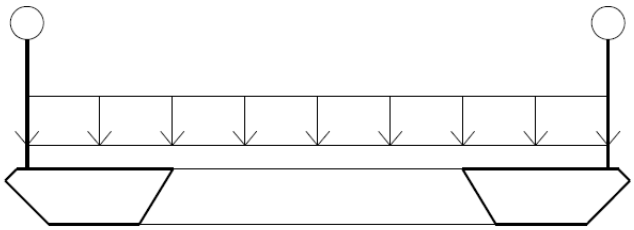

Figure 3.5 Assumed load-distribution on the cross beam.

3.2.2 Cables and hangers

The preliminary design calculations of hangers and cables are done with the equations found in the book, Cable Supported Bridges (Gimsing, 1998), chapter 3.1. The areas of cables and hangers are found from the Matlab script, predesignofcablesandhangers.m, given in the attachment. Since the calculated hanger area needed is much smaller than the area used in the Hardanger Bridge, the values from Hardanger Bridge are used for all the models. That is because the length interval between the hangers is the same in both cases; the only difference in load on the hangers comes from the girder size. The needed cable area is multiplied with a factor of 1.5 to give an extra safety margin. The cable area of the Hardanger Bridge has larger safety margin, but with the dimensions of the Sogne Bridge, this would give very big cable dimensions. Change in the cable area when coming up to a certain size will have small influence on the natural frequencies. That is because both the stiffness and the mass will increase, and the two will cancel each other out (Xiang Haifan, 2007). A table with the structural properties for the different models is given in the appendix A3.

The sag of the cables is chosen as L/10. This is an often used sag ratio (Gimsing, 1998). A higher sag ratio will give lower cable forces, but this requires higher pylons.

It is preferable to fix the cable to the girder at mid span for long suspension bridges. The fixed connection will reduce deflections in the case of unsymmetrical load on the bridge. It will also prevent longitudinal displacements between the cable and the girder, this will be an issue when one side of the girder is fixed at one anchor and the other side has a movable bearing (Gimsing, 1998). In this thesis the case with unsymmetrical load is not investigated and the fixed connection is not included in the models of the bridge. For a design with mono cable this fixed connection is not possible to build the traditional way, due to the hanger's interference with the roadway. An alternative way to fix the cable at mid span has to be figured out (Miguel, 1998 August). An alternative is to have vertical hangers at the middle of the bridge where the inclined hangers would have interfered with the roadway.

With a long span, the cable area grows quite large. Because the cable consists of many circular wires there will be open spaces in the cable cross-section. From this the actual cable area is larger than the effective area, and the drag forces on the cables may have a big

influence on the response of the bridge. When applying a mono-cable, the diameter of the mono-cable is smaller than the sum of the diameters of the traditional two cable solution, so to apply a mono-cable gives less drag forces on the cables. The drag effect on the critical velocity is not investigated in this thesis.

3.2.3 Pylons

Pylons are designed to make the dynamic system more accurate. It is stated in (Xiang Haifan, 2007) that pylons can be neglected for horizontal and torsional vibrational modes, but should be taken into account for vertical modes. Since all the vibrational modes are used to calculate the critical flutter velocity and the response of the models, the pylons are designed. In the design, the constructive period is not evaluated.

The pylons from the Hardangerbridge are used as a starting estimate, and then the dimensions are scaled up with a factor equal to the increase in span length. An additional multiplication factor is used to ensure that all the estimates are on the safe side.

The pylons are checked with Euler load, with critical length of L=2*H. This means that any possible horizontal stiffness contributions from the cables are neglected. This is a conservative estimation. Horizontal forces on the pylons are not considered at all, this is taken into account with the multiplication factor on top of all the other conservative estimations. General concrete properties are taken from the Hardangerbridge, see table 3.1. The cross section is considered un-cracked. This means that the pylons do not experience tension. This assumption is not conservative and will therefore contribute to the added multiplication factor.

The multiplication factor is chosen as 1.5 for the pylons. All the Abaqus models have the same pylons, except for the mono cable models where the angle of the legs are adjusted so the legs meet at the top, see figure 3.6. The design is conducted with the loads from the TF cross section. This means that the dimensions are larger than necessary for the other models since they have smaller girders. This gives a higher stiffness to the system than required and may increase the natural frequencies of the bridge. The calculation of the pylons can be found in the attached files (filename:columnsdesign.xlsx).

Figure 3.6 Pylon for a mono-cable suspension bridge.

3.3 Guide vanes and vertical plate at center air-gap

The cross sections chosen from Brusymfonien and the Hardanger Bridge have guide vanes. The application of guide vanes has proven to increase the flutter stability with approximately 30 percent (Xiang, 2007). This is also shown in the Brusymfonien report (Statens Veivesen, 2005). For the TF section, there are no guide vanes, but a vertical plate at the center air-gap. From the article “On flutter characteristics of separated two box girders” (Matsumoto, 2007) it is shown that the plate improves the flutter stability.

3.4 Aerodynamic derivatives for the chosen models

For cross-section TF, a slotted girder with vertical plate in the middle, the values for the aerodynamic derivatives are taken from the article, “On flutter characteristics of separated two box girders” (Matsumoto, 2004). There are plots in the article of the values for Ai and Hi (i=1,2,3,4). From these plots the curves for the aerodynamic derivatives as a function of reduced critical velocity are approximated by linear and quadratic equations.

For the models with a single bridge girder, H, the aerodynamic derivatives are obtained from wind tunnel tests of the cross-section for the Hardanger Bridge (Ole Øyseth, 2012).

For the slotted box section, Brusymfonien, the values for the aerodynamic derivatives obtained through wind tunnel tests are scattered and few, see figure 3.7. This means that it is not given what kind of curve is best to fit to the data, and the results are uncertain. The reason for these less reliable wind tunnel results may be because the theory around aerodynamic derivatives are developed for an airfoil and not optimized to slotted girders, as mentioned in section 2.1.2.

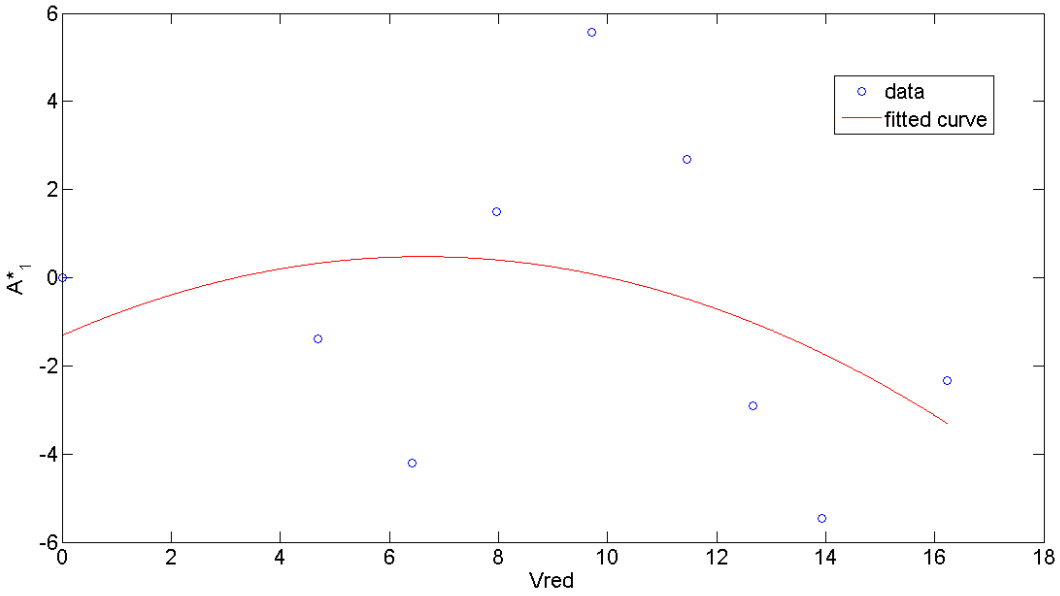

Figure 3.7 Curve fitting for the aerodynamic derivative, A^*_1, for the model B20.

The aerodynamic derivatives are obtained with an attack angle of zero degrees. This is acceptable for a streamlined girder, where the attack angle does not influence the critical velocity significantly (Hansen, 1999). The aerodynamic derivatives of the different cross sections are plotted in figure 3.8, the functions can be found in appendix A4.

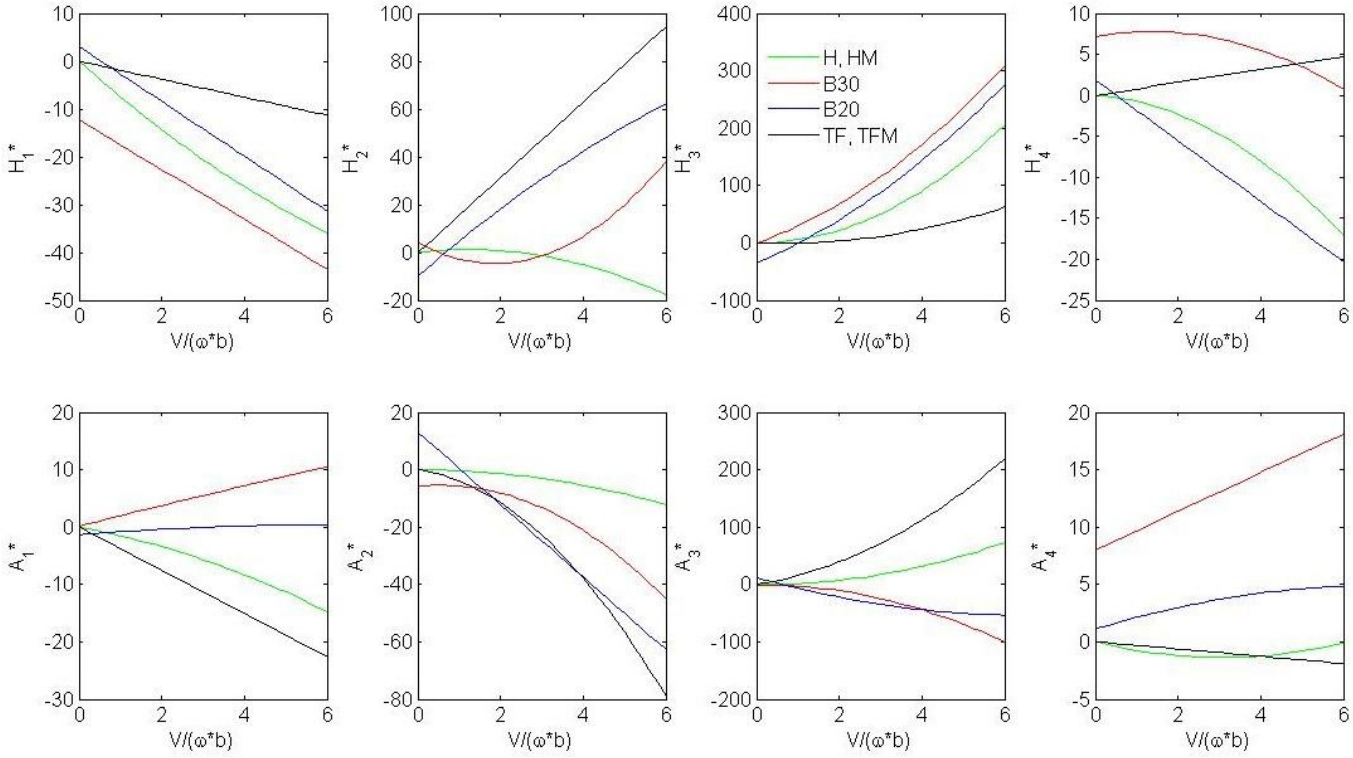

Figure 3.8. Plot of the Aerodynamic derivatives as a function of the reduced velocity for the chosen cross sections.

3.5 Static force coefficients for the models

The static force coefficients of the different models are presented in table 3.2. The values are given at an attack angle of 0 degrees. C_D', C_L' and C_M' are derivatives of the attack angle at 0 degrees.

Table 3.2 Static force coefficients for an attack angle of 0 degrees.

Cross section	$\bar{C}_D$	C_D'	$\bar{C}_L$	C_L'	$\bar{C}_M$	C_M'
H	0.794	0	-0.254	2.502	0.004	0.859
TF	1.20	0	-0.02	0.05	-0.01	0.006
B20	1.754	0	0.118	6.37	0.185	-0.8
B30	1.819	0	-0.2	6.96	0.194	-3.24

The values for the H model are obtained from the computational report of Hardangerbrua. For the B30 and B20 sections the values are gotten from the Brusymfoni report (Vegvesen, 2005). There is an uncertainty about the sign for the $\bar{C}_L$ value for the B20 section. Of 12 different variations of the section, it was only this alternative that had a positive $\bar{C}_L$. It is possible that it is a writing error in the report and the value should have been negative. The article with the TF section did not include the static force coefficients. To get an

approximation for these values an article with a similar cross section is used (Sato, 2002). This slotted box section has a vertical plate in the middle as the TF section, but it has also guide vanes which the TF section does not have.

4 Abaqus

Abaqus is a finite element program that, among other things, can calculate the natural frequencies and mode shapes of a structure (SIMULA, 2010). To calculate natural frequencies and modes, Abaqus can use Lanczos eigensolver. This is a method that by the eigenvalue problem iterates until the solution is obtained, see equation (4.1).

$$(\boldsymbol{K} - \omega_j^2 \boldsymbol{M})\varphi_j = 0 \qquad \textbf{(4.1)}$$

Here **K** is the stiffness matrix, **M** is the mass matrix, ω_j is the j-th natural frequency and φ_j the associated eigenvector. Abaqus can calculate as many natural frequencies as there are degrees of freedom in the model. It is possible to specify the number of desired natural frequencies to calculate. The mode shapes at high frequencies are not interesting (see section 2.2.6) so it is normal to only look at the 30-50 first frequencies. Equation (4.1) shows that it is the stiffness matrix and mass matrix that determine the natural frequencies and modes. The important thing when modeling a bridge in Abaqus is therefore to represent the mass and stiffness properties correct.

4.1 Making models of the Sogne Bridge in Abaqus

The models of the Sogne Bridge are modeled with two parts, one for the towers and another for the cable system and girders. Figure 4.1 shows an Abaqus model of the bridge.

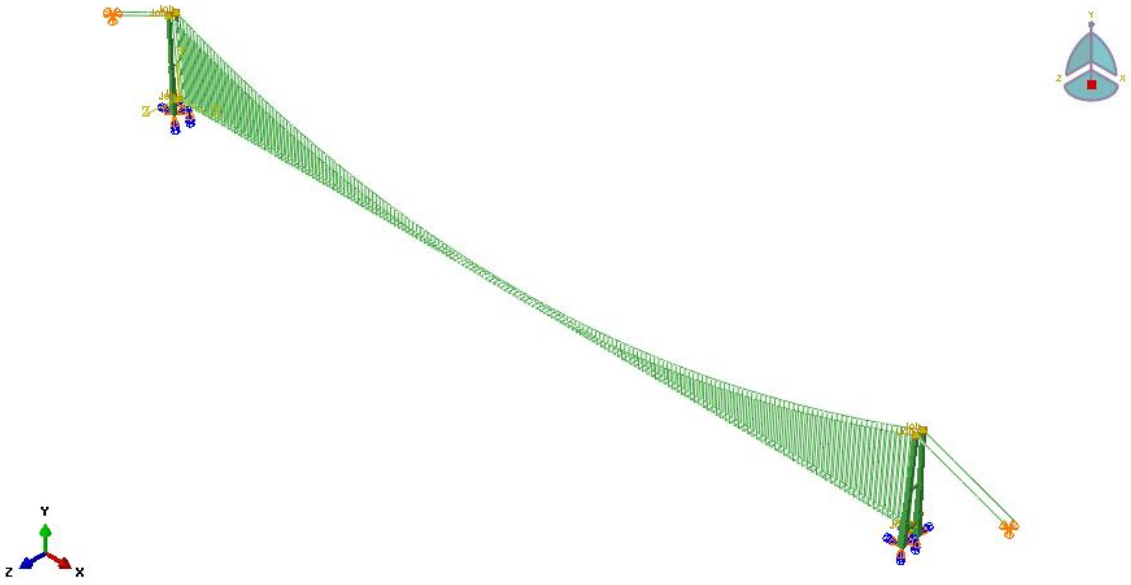

Figure 4.1. Abaqus model of the Sogne Bridge.

All the connections in the same part are fixed against rotation. This is not the case with a real suspension bridge, where the connections are somewhere between fixed and free to rotate for the cable system. This error is disregarded since it has a negligible influence on the

results. The increased stiffness given by the fixed connection can be neglected due to the slenderness of the parts, if subjected to compression the hangers will buckle.

4.1.1 Elements

The bridges are modeled with B33 elements. These are beam elements that represent bending. In the cables and hangers there are only axial forces, but the bending forces included by the beam elements are very small compared to the axial forces and will have an insignificant influence on the result.

4.1.2 Girder, hangers and cables

The bridge girders are modeled as generalized sections in Abaqus. That means that only the structural parameters are specified, not the geometry. To get the correct eccentricities, massless bars with high stiffness are modeled between hangers and girders, and between girders and cross-beams, see figure 4.2. The stiffness of the massless bars is thousand times as high as for the girder. To represent the mass and mass moment of inertia for the bridge girder, point masses every 20m are applied. Here all the mass from girder and additional masses from deck, railings and similar are located. The value per meter is multiplied by 20m. The mass moment of inertia around the longitudinal direction of the bridge is also specified in the same point as the masses. For the hangers and the cables the density is specified higher than the steel density. This is to include all the extra masses in connection with the hangers and cables. The values of the extra masses are taken from the computational report of the Hardanger Bridge (Vegdirektoratet B. i., 2008).

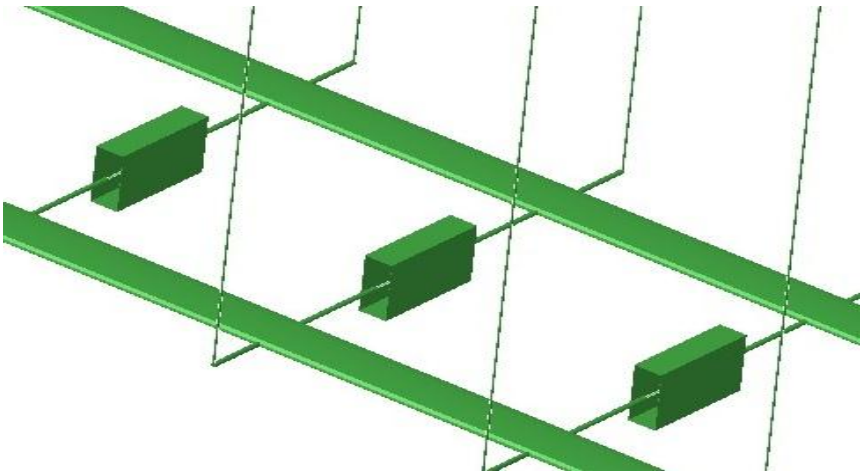

Figure 4.2. Massless bars to give the correct eccentricities for the slotted TF girder.

The hangers are modeled with one element per hanger. This will prevent vibration modes represented by the hangers, which is uninteresting since resonance in the hangers is not a problem.

The curving upwards of the bridge girder has a much smaller curve/span rate than there is in the Hardanger Bridge. For the Hardanger Bridge the ratio is 10m/1310m=0.0076, for the Sogne Bridge the ratio is 9m/3700m=0.0024. The reason the bridges is not modeled with the

same ratio is because this means that the towers would have to be about 20m higher than they are modeled now. The reason for curving the girder is to have enough space for big ships to sail under the bridge.

4.1.3 Pylons

The pylons have a height of 440m, see figure 4.3. This means that even though they are made of concrete and are massive, they will have displacements at the top. The pylon legs are fixed at the bottom and connected to the cables at the top. To model the bridge with pylons gives a case where the cables are more fixed than when having slide bearings instead of pylons. This gives higher stiffness to the structure, which in turn gives higher natural frequencies. There is no movement between the pylon top and cables, but the connection is free to rotate. For the real bridge, the cable will probably be allowed to slide at the pylon top. How much they will slide is questionable since the axial forces from the cables down in the pylon legs are enormous. The girders are connected to the pylons at a height of 60m above water level. The connection is free to rotate for the slotted box girder models, for the single box girder models the connection is fixed against torsional rotation.

Figure 4.3. Pylon of the Sogne Bridge modeled in Abaqus.

4.1.4 Steps

To include the geometric stiffness when calculating the natural frequencies of the bridge, the first step accounts for the self-weight of the structure. Ngeom, non-linear geometry is switched on in this step. This gives a deflection of 30-60m depending on which of the models are submitted. To reverse this deflection the cables are specified with a temperature expansion coefficient, and tightened with a decrease in temperature in the next step. See figure 4.4. In the last step the fifty first natural frequencies and corresponding vibration modes are calculated.

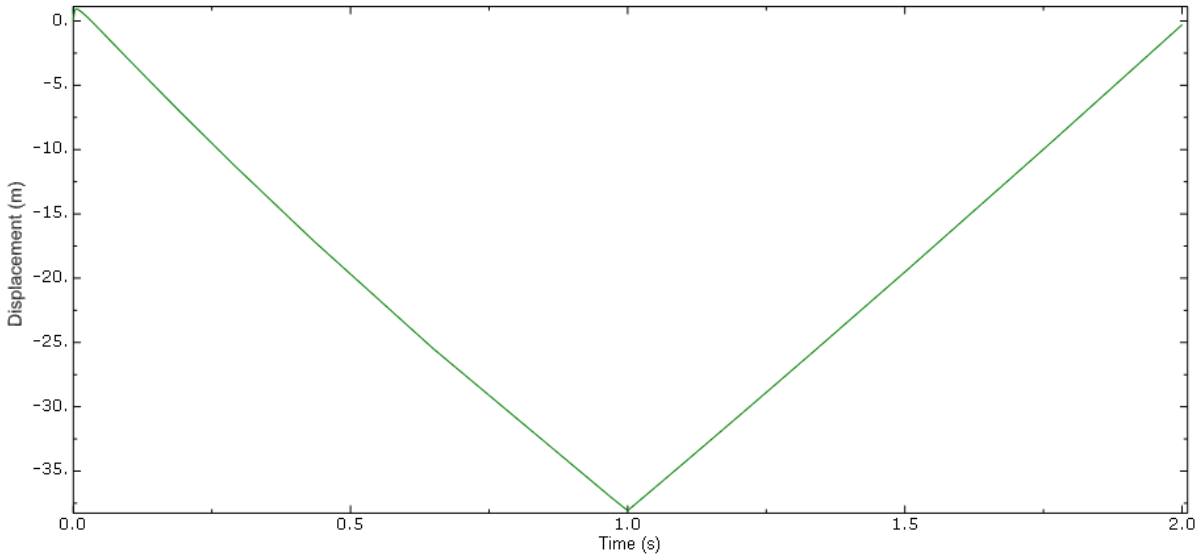

Figure 4.4. Vertical displacement of the center of the bridge for the first and second step.

4.2 Matlab program to generate the geometry

It is possible to create an Abaqus model from a written input file. It is the same that happens when the model is drawn in Abaqus; the information is converted to a written file. It is possible to make this input file with a Matlab program. For the models of the Sogne Bridge the geometry is generated with a self-made Matlab program. This program specifies node numbers with coordinates and then elements are specified between the nodes and assigned a number. These numbers are generated with loops that write out the information to a file. Element sets are created by taking the numbers of the wanted elements and write them to the file. It is not possible to mesh the Matlab generated models inside Abaqus, the mesh has one element between each node. The only input parameters for the Matlab program are the basic geometry and how many elements wanted for every 20 m. The sections, material properties and boundary conditions are made manually in Abaqus. There are three different Matlab programs. The setup is a bit different when making a mono cable model and when applying a slotted box girder instead of a single box girder. One of the programs is found in the attachment with computer programs (filename: BridgegeometryAbaqusinput.m).

4.3 Static wind load in Abaqus

To calculate the static response of the bridge models due to the mean wind velocity, the wind forces are applied to the models in Abaqus, se figure 4.5. It is assumed that the entire span of the bridge is subjected to the wind load. The drag and lift loads on the girder are applied as concentrated forces to a node at the center of the girder for every 20 m. For the models with two box girders the loads are applied on the cross-beams in order to have symmetry. The moment load is applied as a concentrated moment in the middle of the girder every 20 m. The drag load on the cables is applied as concentrated forces where the hangers are fixed to the cables.

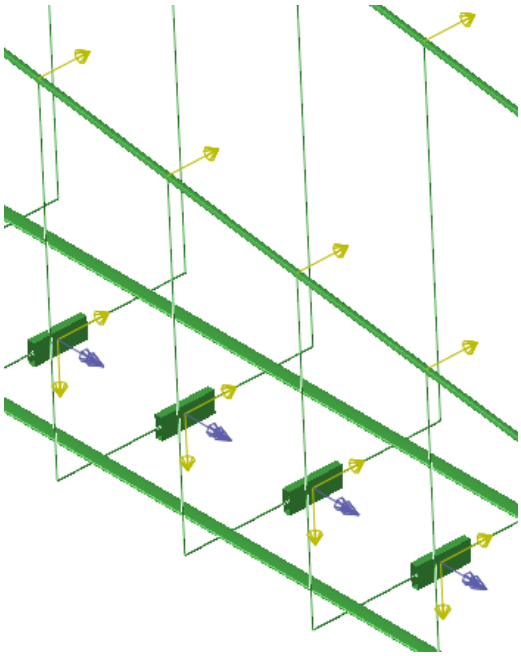

Figure 4.5. Static wind forces applied as concentrated forces in Abaqus.

4.4 Getting data from the Abaqus model

To extract information from Abaqus a set with nodes is created. The node set consists of nodes every 20 m along the center of the bridge girder. For the slotted box sections the node is the middle point of the cross beam. When carrying out the calculations of the frequencies and mode shapes of the model, the program writes the results out as a data file. To get the mode-shapes of the girder it is possible to specify in the keywords that the coordinates and the displacements of the node set shall be written out to the data file. To get the relevant information out from the data file, a Matlab script provided by Ole Øiseth is used. This Matlab program searches through the data file until it finds the name of the table it is looking for, and then starts to gather the wanted information from the tables and arranges the values into Matlab matrixes.

5 Matlab programs

The calculations done in this thesis are carried out in Matlab. The authors have made a simple two mode flutter program, a static divergence program and a response calculation program. The multimode flutter calculations are done with a Matlab program provided by Ole Øiseth.

The structural damping is impossible to determine mathematically. This is because the damping comes from friction in all the thousand connections in the structure, opening and closing of microcracks in the concrete pylons and repeated elastic straining of the steel among other things (Chopra, 2007). For all the Matlab calculations the structural damping ratio of the modes is assumed to be ζ=0.005. This damping ratio corresponds satisfactory with the damping ratios given for the modes from the Hardanger Bridge (Ole Øiseth, 2011).

5.1 Multimode flutter calculation

This program uses modes, eigenfrequencies and mass properties from the Abaqus models and functions for the aerodynamic derivatives for the different cross sections given in appendix A4. The mass, modes and natural frequencies are obtained from Abaqus as described in section 4.4. There is no limit for how many modes possible to include in the flutter calculations.

The critical flutter velocity is calculated by the eigenvalue problem described in section 2.1.3. The routine considers the fact that each mode can have displacements in three directions; horizontal, vertical and rotation. The contribution from the horizontal displacement is included with the aerodynamic derivatives P*, $A^*_{5,6}$ and $H^*_{5,6}$. For the two mode flutter program those aerodynamic derivatives are zero.

5.2 Bi-modal flutter program

The bi-modal flutter program uses the assumption of pure one-directional mode shapes. The mode shapes are still taken from the Abaqus models, but the unused directions are simply neglected.

The solution procedure is partly described in section 2.1.3. The algorithm for writing the program is taken from the book, Wind Loads on Structures (Hansen, 1999).

Since the final eigenfrequency of the flutter mode is unknown, this frequency was made symbolic by a “syms” command in Matlab. The roots are then solved by a “solve” command that solves the roots with respect to the symbolic variable ω_r. The “solve” command is a symbolic solver in Matlab that gives an exact solution for a given symbol. If the solver cannot find the solution, it uses a numerical toolbox to estimate the solution (Mathworks, 2012). Note that the parts of the roots that have imaginary values are not plotted; it is only the real part of the roots that can give the actual flutter velocity. Note that the critical frequency has to have a positive value. Intersection of the roots at a negative frequency is neglected. The bi-modal flutter script can be found in the attached files (filename: Bimodalflutter.m).

5.3 Static divergence program

The program used to calculate the critical velocity due to static divergence is given in the attached files (filename: Staticdivergens.m). The program is based on the theory given in section 2.1.4. The quasi static coefficients used are given in table 3.2.

5.4 Response calculations

The mean wind velocity used for the response calculations is chosen as 30 m/s. This is because the value is around the serviceability limit and low enough that the assumption given in section 2.2.11 holds.

The response calculations are done in Matlab using vibrational modes and eigenfrequencies from Abaqus. Aerodynamic derivatives for the different bridges are given in appendix A4. The wind parameters used are the same as for the Hardanger Bridge report (Vegdirektoratet B. i., 2008). The Matlab script for response calculation can be found in the attached files (filename: Response.m).

The Matlab script should be fairly easy to understand. It contains only algebraic operations, and no special functions are used.

5.4.1 Static load

The static load applied in Abaqus is calculated according to equation (2.55) given in section 2.2.13. The static load coefficients are given in table 3.2. The drag coefficients for the cables are taken from the computational report of the Hardanger Bridge (Vegdirektoratet B. i., 2008). The drag forces on the hangers are included by multiplying the drag coefficients with a factor of 1.6, for both girder and cables.

6 Results

6.1 Vibration modes and natural frequencies

The mode shapes are a combination of horizontal displacement, vertical displacement and rotation. The vertical mode shapes are approximately pure vertical movement, while the mode shapes dominated by torsion and horizontal movement usually are a combination of both types. For the mono cable models this tendency is more evident, even the first horizontal mode shape has a significant torsional rotation. With a long span like 3700m, the mode shapes are behaving differently than for a suspension bridge with one third of the span. The mode shapes in torsion tend to twists a different way at the ends compared to the middle, see figure 6.1.

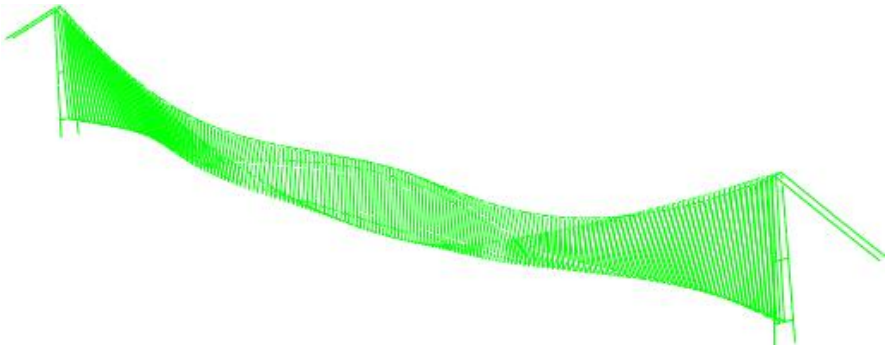

Figure 6.1 First torsional mode for the B20 model.

The first symmetrical natural frequency for the vertically dominated mode shape has a circular frequency of about 0.45-0.47 rad/s. The first one in torsion has a frequency of 0.64-0.82 rad/s, see table 6.1. This seems correct when compared with other models tested. For the 5000m bridge in the article "Aerodynamic challenges in span length of suspension bridges" the first symmetrical vertical mode shape has a frequency of 0.39 rad/s and the torsional a frequency of 0.54 rad/s (Xiang, 2007). For the Hardanger Bridge with a main span of 1310m the vertical frequency is 0.675 rad/s and the torsional frequency is 2.225 rad/s. It is therefore reasonable that the results from the Sogne Bridge models with a main span of 3700m lie between the other two, and closer to the 5000m bridge's frequencies.

Table 6.1. Natural frequencies for the first symmetrical mode shape in horizontal, vertical and torsional direction.

Model	1. horizontal ω [rad/s]	Sym 1. vertical ω [rad/s]	1. torsional ω [rad/s]
H	0.17059	0.46251	0.82035
HM	0.16938	0.46137	0.80155
TF	0.19518	0.45789	0.73435
TFM	0.19289	0.45636	0.74381
B20	0.18436	0.46844	0.74544
B30	0.18567	0.46503	0.64072

The B30 section has a significantly lower torsional frequency than the other slotted sections. This may be explained by the length of the cross beam, it is 10 m longer than for the B20 section. This beam might not have been designed stiff enough; the dynamic forces are not considered when designing the beam. As a result the torsional stiffness is lower than for the B20 section.

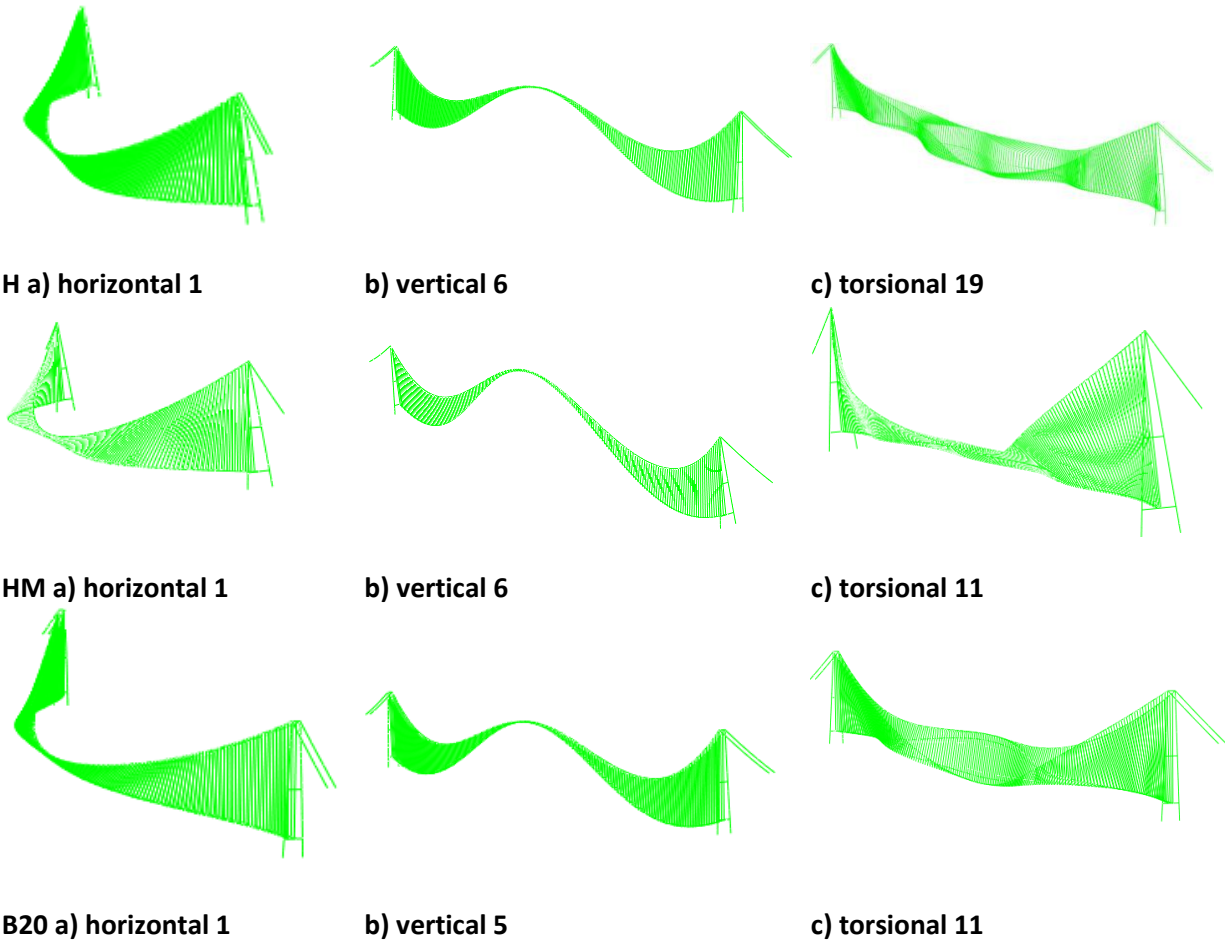

H a) horizontal 1 **b) vertical 6** **c) torsional 19**

HM a) horizontal 1 **b) vertical 6** **c) torsional 11**

B20 a) horizontal 1 **b) vertical 5** **c) torsional 11**

Figure 6.2 Vibration modes in horizontal, vertical and torsional direction for models H, HM and B20

Figure 6.2 shows that the first horizontal mode-shape looks the same for all the models, except for the HM model where there is a rotation of the girder, see figure 2.9. The first symmetrical vertical mode-shape is the same shape for all the models. The torsional mode-shape varies between the models. For rotation to occur, the mono-cable must be rotated as a contrast to the two cable system where one cable is raised and the other lowered.

6.2 Critical wind velocity

The design velocity for the Sogne Bridge is 64.2 m/s, the calculation can be found in appendix A1.

6.2.1 Flutter

The values for the critical velocity in table 6.2 are obtained from Matlab, where multimode flutter analysis is carried out with the fifty first vibration modes. There is no difference in critical velocity between calculations with the thirty first modes and the fifty first modes.

Table 6.2. Critical flutter velocity and critical circular frequency.

Model	Vcr [m/s]	ω_{cr} [rad/s]
H	50	0.76
HM	72	0.75
TF	>110	-
TFM	>110	-
B20	108	0.63
B30	>110	-

The range for Vred=V/(ω*b) which the aerodynamic derivatives are found for, are limited. This means that for models TF, TFM and B30 the information output from the flutter routine when the velocity gets high and the frequencies goes to zero are no longer reliable, see figure 6.3. As a result the assumption is that the models will not start to flutter for a wind velocity under 110 m/s, but to say anything about what happens for higher velocities is not possible with the available information in this thesis.

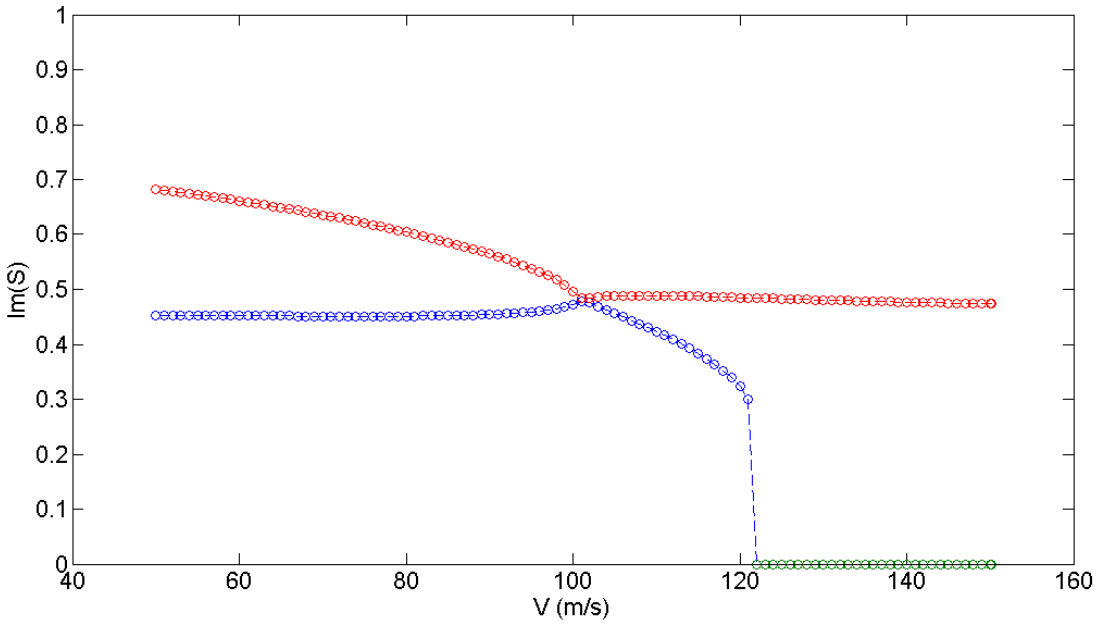

Figure 6.3 The imaginary part of the eigenvalues (frequencies) for the TF model.

It is usually the first symmetrical vertical mode and the first torsional mode that control the bridge flutter with only minor contributions from other modes (Trein, 2011). Figure 6.4 shows that two-mode flutter with mode 6 and 11 for the HM model gives a critical velocity of 82 m/s, and by adding mode nr 13, 18, 19 and 26 the critical velocity is reduced with about 8 m/s.

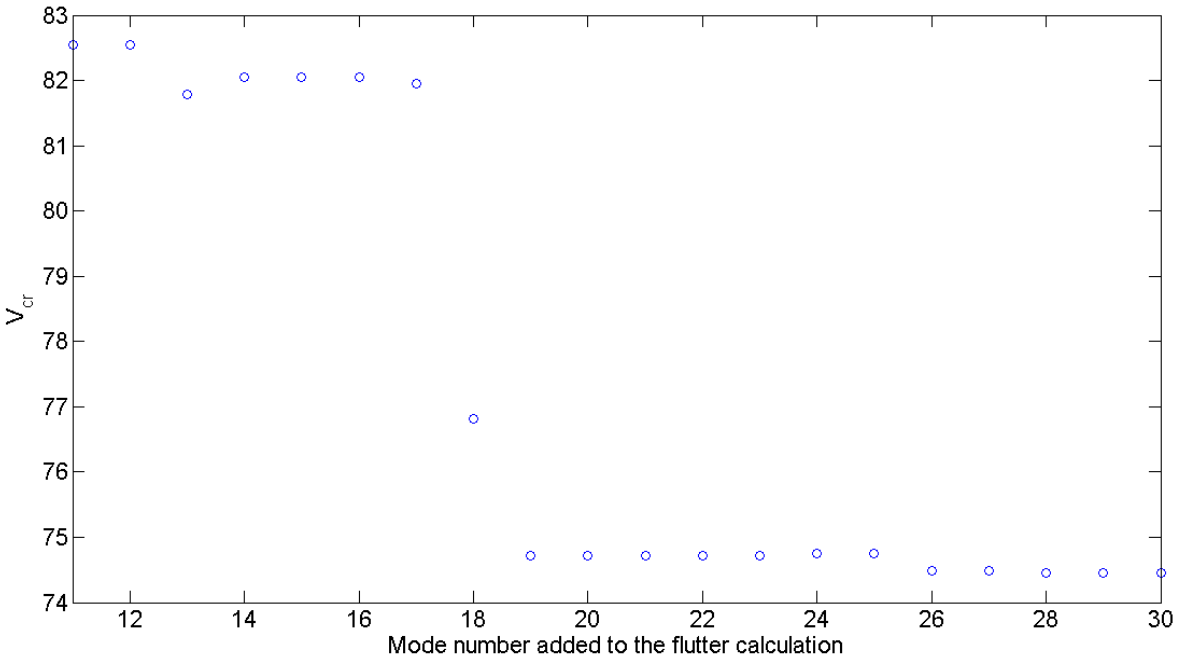

Figure 6.4. Plot that shows which modes contribute to reduce the critical velocity for multimode flutter, model HM.

The shape wise similarity between the vertical and torsional vibration modes has proven to be important for the initiation of flutter and the value for the critical velocity, see section 2.1.3. For two mode flutter of the H model, the shape-wise similarity between mode 6 and 19 is 0.93, see equation (6.1), and gives a critical velocity of 76 m/s. The first torsional mode shape for the H model is number 11, but because of a higher shape wise similarity, it is the next torsional mode that causes the lowest two-mode flutter velocity for the H model. For the HM model the shape-wise similarity between mode 6 and 11 is 0.86, see equation (6.2), and gives a critical velocity of 82 m/s. Only the torsional part of the mode shape is considered for mode 19 (H) and 11 (HM).

$$\frac{\int_L \phi_6 \phi_{19} dx}{\int_L \phi_6{}^2 dx} \frac{\int_L \phi_6 \phi_{19} dx}{\int_L \phi_{19}{}^2 dx} = 0.93 \qquad \textbf{(6.1)}$$

$$\frac{\int_L \phi_6 \phi_{11} dx}{\int_L \phi_6{}^2 dx} \frac{\int_L \phi_6 \phi_{11} dx}{\int_L \phi_{11}{}^2 dx} = 0.86 \qquad \textbf{(6.2)}$$

Perfect shape wise similarity would give the answer 1 to equations (6.1) and (6.2). The difference in shape-wise similarity contributes to the difference in critical flutter velocity between the H model and the HM model. Figure 6.5 shows that to add mode number 19 to the multimode flutter calculation for the H model reduces the critical velocity with 20 m/s, which is a significant contribution.

For the Hardanger Bridge it was not the first symmetrical vertical mode that gave the lowest flutter velocity, it was the second symmetrical vertical mode together with the first torsional mode (Ole Øiseth, 2011). This was also explained with higher shape-wise similarity for the two modes that gave the lowest flutter velocity.

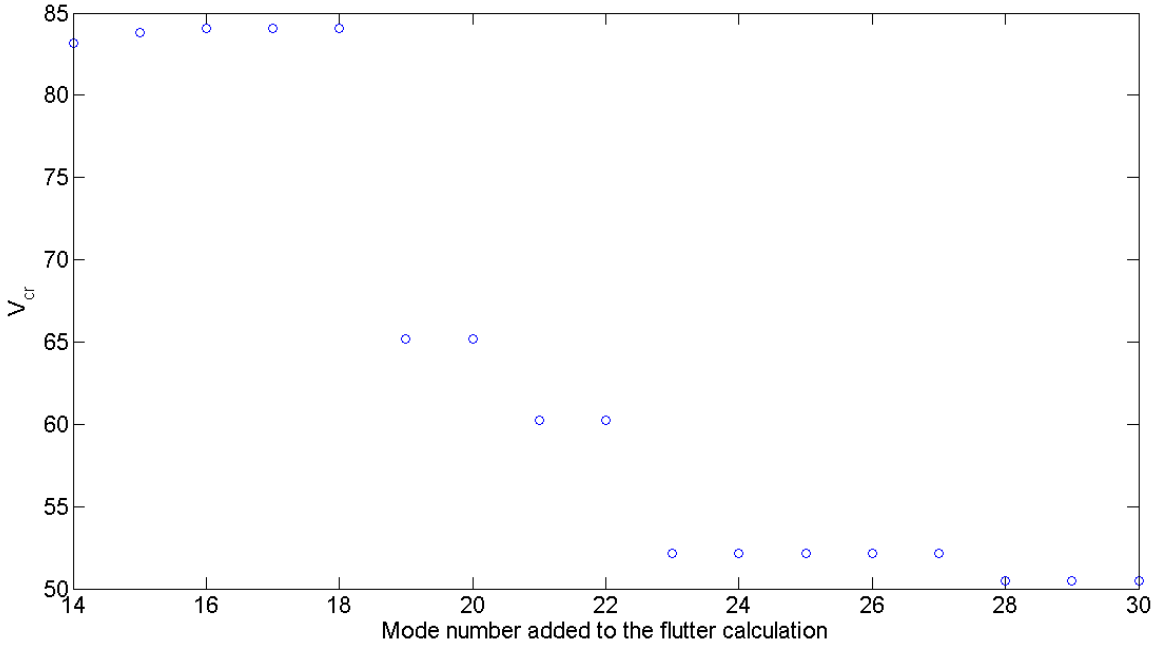

Figure 6.5 Plot that shows which modes contribute to reduce the critical velocity for multimode flutter, model H.

For the H and HM models the contribution from horizontal movement is included with aerodynamic derivatives, P*s, $H_{5,\ 6}$* and $A_{5,\ 6}$*, calculated with quasi static theory. The critical velocity for HM is higher than the design velocity, 72 m/s > 64 m/s, in contrast to the H model that has a critical velocity of 50 m/s. The critical velocity for the HM model without horizontal contribution is 62 m/s and for the H model 49 m/s. This indicates that for a mono cable model the horizontal contribution is considerable, but for the traditional two cable system the horizontal contribution is negligible.

The critical velocity for B20 is 1m/s higher with the P*s. For the TF sections the P*s are not included. The article with the aerodynamic derivatives for the TF section does not include the static load coefficients for the cross section that are used to calculate the aerodynamic derivatives with quasi static theory. To include the P*s, the static force coefficients from a similar cross-sections has to be used. This will be inaccurate. To neglect the P*s for the TF section is justified by the fact that the difference in critical velocity is small, and to neglect

them is on the conservative side. For TFM, to neglect the contribution form the horizontal movement is very conservative and gives a lower critical velocity.

With the aerodynamic derivatives obtained for the H section applied to the B20 model, the critical velocity for B20 is reduced to 64 m/s. This shows that it is mainly the aerodynamic characteristics with a slotted section that improves the aerodynamic stability limit, not the increase in stiffness. The same is the case for the TF model, the critical velocity with the H aerodynamic derivatives is reduced to 62 m/s. For the TFM model with H aerodynamic derivatives, the critical velocity is 95 m/s. This shows again that the structural measure of applying a mono-cable increases the critical flutter velocity.

With the aerodynamic derivatives of B20, the stability limit is lower for B30 than for B20. The frequency separation between the lowest torsional mode and vertical mode for B30 is lower than for B20. This indicates that there is no structural advantage to increase the width of the sloth; it only improves the aerodynamic ability.

The damping ratio is plotted to see if any of the modes have low damping for velocities before the flutter velocity is reached. In figure 6.6 the damping ratio for model H is shown. The damping of the vertical mode increases with increasing wind velocity and has values outside the shown axis-range. Only the modes that contributed to the reduction of the critical velocity according to figure 6.5 are included. The plotting of the damping is done for all the models. None showed modes with damping close to zero prior to the flutter velocity. Low damping of modes would have resulted in high response-contribution from those modes, and may have made the model unusable for a lower velocity than the critical.

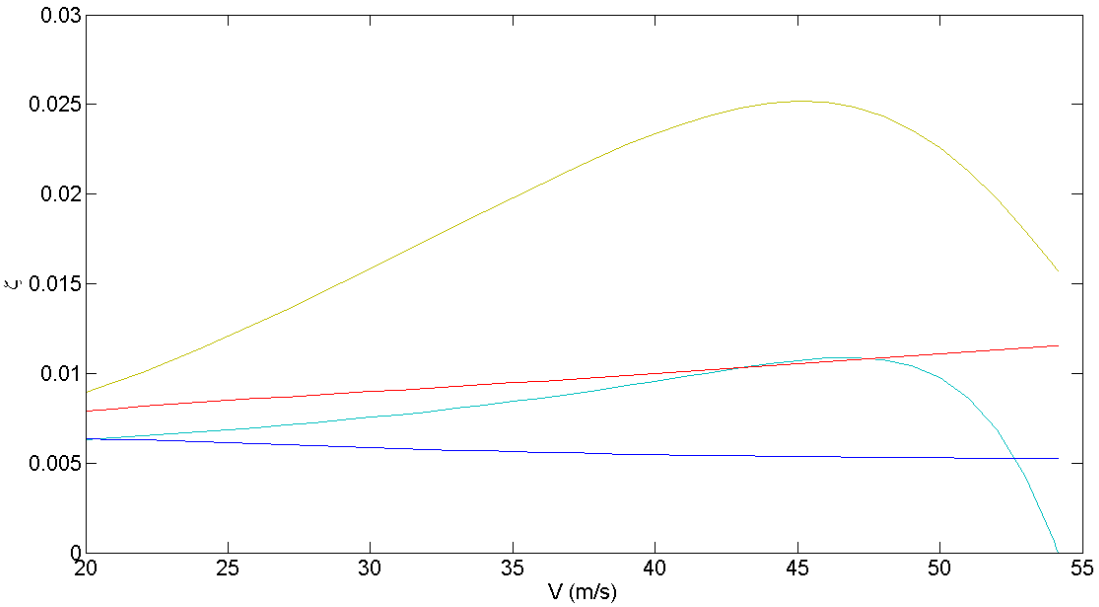

Figure 6.6. Plot of the damping ratio as a function of the wind velocity for the H model.

There was no difference in critical velocity between the boundary conditions with the girder connected to the pylon fixed against torsional rotation and the girder connected free to

rotate for the H and HM models. With a 3700 m span the effect of the boundary condition for the girder ends will have minor influence on the mode-shape properties along the bridge. It is the cable system and girder stiffness that are important.

6.2.2 Result from the two-mode flutter program

The multimode flutter program gives a critical velocity of 76 m/s for two mode flutter with mode 6 and 19 for the H-model. The self-made two-mode flutter program gives a critical velocity of 75 m/s for the same two modes. The small difference of 1m/s comes probably from neglecting the P*s for the two-mode flutter program. For the HM model the two mode flutter program gives a critical velocity of 70 m/s for mode 6 and 11. With the multimode flutter program the critical velocity is calculated to be 82 m/s. This is a significant difference, but as mentioned earlier in this chapter the contribution from the horizontal movement is considerable for the mono-cable model, and it is assumed that it gives the difference in the results from the two programs. When calculating the critical two-mode flutter velocity without the horizontal contribution the velocity is 70 m/s. These results verify the multimode flutter program.

6.2.3 Static divergence

A Matlab program, see section 5.3, uses a dominant torsional mode to calculate the critical velocity for the occurrence of static divergence.

Table 6.3. Critical velocity by static divergence of a torsional mode.

Model	Torsional mode	Vcr [m/s]	ω_{cr} [rad/s]
H	19	120	1.21
HM	11	230	0.80
TF	8	-	-
TFM	8	-	-
B20	11	-	-
B30	8	-	-

It appears that the slotted girder sections do not converge to a critical velocity for static divergence, see table 6.3. This has to do with the value of the static force coefficients, C_M' and C_L'. For the B sections, C_M' is negative, this gives no solution for Vcr. The values for C_M' and C_L' for the TF sections are very small, this gives a very high critical velocity (>500m/s). The slotted girders have higher torsional stiffness than a single girder; higher stiffness increases the critical velocity.

The static force coefficients obtained for the TF section are taken from another article with a different section, this gives very uncertain results. For better test results, static force coefficients should be obtained through tests of the TF section.

These results show that static divergence does not give the stability limit for the bridge models. The values for the TF section is obtained from a cross section with guide vanes, see section 3.5. The H and B sections do also have guide vanes. These results may imply that guide vanes reduce the chance of static divergence. However, there is no calculation for static divergence without guide vanes, so this hypothesis is not confirmed.

6.3 Response results

6.3.1 Accuracy of the solutions

To make the script as accurate as possible, small increments in the frequency vector and length vector is needed. The length vector is governed by the nodes in Abaqus, and cannot be changed in the Matlab program. Appendix B6 shows four plots of abs(H) for the first mode in horizontal direction for bridge H with frequency steps 0.001, 0.005, 0.05 and 0.5. These plots show the influence the size of the frequency steps have on the functions. In table 6.4 the variance in horizontal direction is compared with the different types of steps and the calculation time of the scripts (Bridge H, V=30m/s at mid-point). From these results, a step of 0.005 rad/s is used and considered accurate enough. The scripts where the mean wind velocity is varied from 5-30 m/s will take about 6 days to complete if the 0.001 frequency step is used. Note that the 0.001 frequency step is set to be the basis for the error estimation.

Table 6.4 Frequency step table

Frequency step (rad/s)	Calculation time (t)	Horizontal variance(m)	Error (%)
0.5	114 (2 min)	3,2192	590 %
0.05	1003 (16 min)	1,0488	125 %
0.005	9995 (2,7 t)	0,5048	8 %
0.001	86121 (24 t)	0,4668	0 %

6.3.2 Number of modes

The number of modes to include is important for the accuracy of the solution. The downside of including too many modes is increased calculation time. Note that these results are calculated at mid-span, the modal contribution will be different on other points along the span as explain in section 2.2.7. In figure 6.7, figure 6.8 and figure 6.9, plots of how much each mode contributes to the total variance is shown (mid-span, H bridge, V=30m/s).

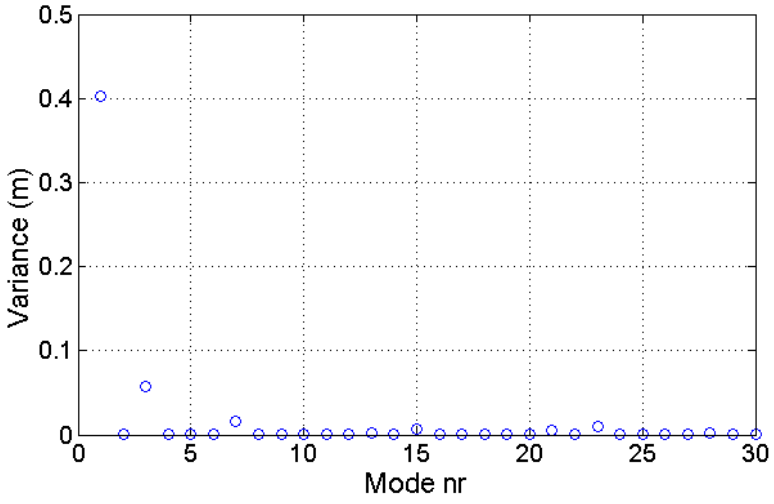

Figure 6.7 Horizontal variance contribution from each mode, mid-span and V=30 m/s, H

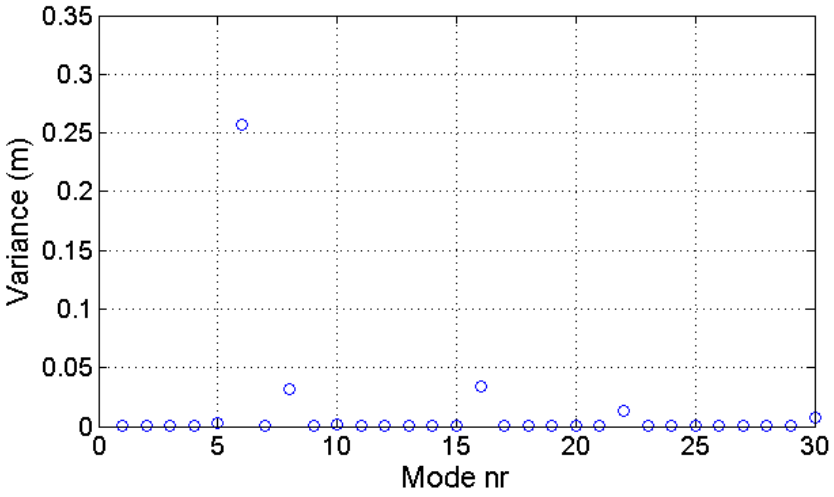

Figure 6.8. Vertical variance contribution from each mode, mid-span and V=30 m/s, H

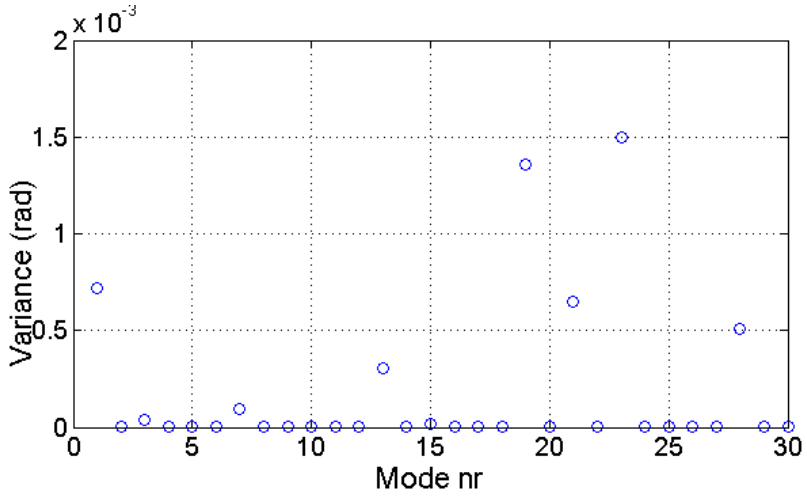

Figure 6.9. Torsional variance contribution from each mode, mid-span and V=30 m/s, H

Figure 6.7 shows the modal contribution to horizontal variance. All of the cross-sections share similar distributions, making individual comparisons unnecessary. There is no need for more than the first 10 mode-shapes for a complete horizontal representation. Mode-shape 1, 3 and 7 has a dominating horizontal component and has high values at midpoint. Since the spectral density of the load has an extreme overweight in the smallest frequency range and the modal stiffness generally increases for higher modes it is no surprise that these modes dominate the response.

The results given in figure 6.8 show vertical variance contribution that is typical for all the bridge models. By the same argument as in the section over, the first 22 modes are considered enough for the vertical variance. There is need for more modes in vertical direction than horizontal direction because the mode-shapes with predominantly vertical deflection have higher eigenfrequencies.

From figure 6.9 a big spread in torsional modal variance distribution is shown. This is typical for all the duo-cable models evaluated. The mode-shapes with predominantly torsional components have higher eigenfrequencies compared to the other directions, but there are small torsional components in some of the “horizontal” mode shapes. An example of this is mode shape 1.

One other consideration regarding mode-shapes in torsional direction is that mode-shape number 30 has an eigenfrequency of only 1.62 rad/s. This is low compared to the Hardangerbridge (Øiseth S. , 2011, 330). Why this is important is explained thoroughly in chapter 2.2.

The modal variance distribution for the mono-cable models is different from the duo-cable models. Figure 6.10 shows the variance contribution in torsional direction for the HM model. The difference for the mono-cable is explained by the horizontal and torsional coupling of mode shapes and the increased stiffness from having to twist the cable to get pure torsional mode-shapes. Both effects are described in subsection 2.2.10. The increased stiffness makes pure torsional mode-shapes absent.

In appendix B2 the rest of the plots are shown.

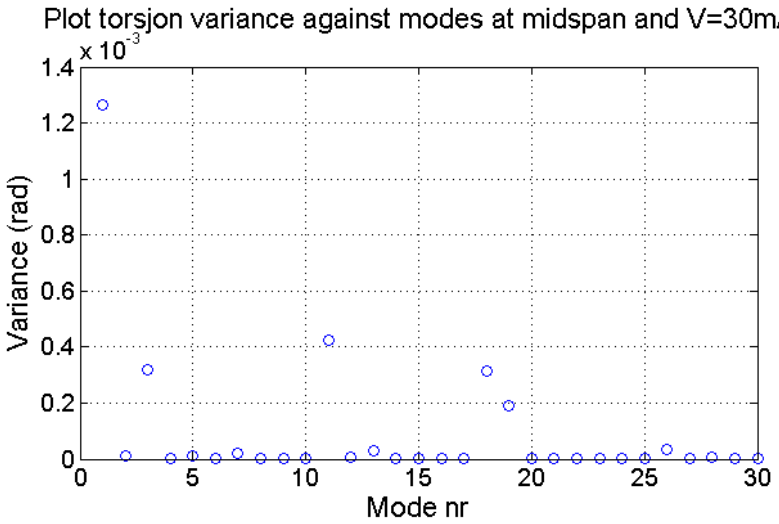

Figure 6.10 Torsional modal distribution at mid-span for V=30m/s, HM bridge

The first thirty modes of a mono-cable bridge are enough to obtain good results in torsion. For the duo-cable models more mode-shapes are probably needed. In figure 6.11, the distribution in torsion from the first 50 modes is shown for the TF model. The total mid-span torsional variance ended up being the same for 30 modes and 50 modes. It is recommended to include the 40 first mode-shapes when calculating the torsional response for long-spanned duo-cable bridges.

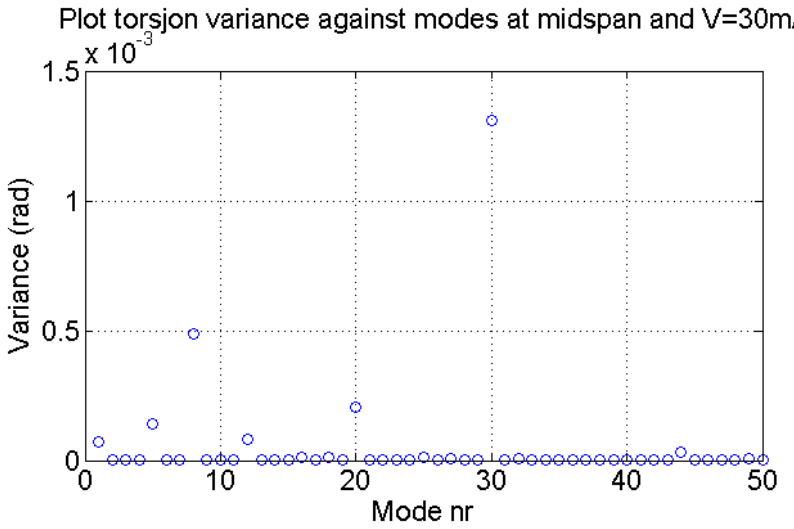

Figure 6.11 Torsional modal distribution at mid-span for V=30m/s, TF first 50 modes

A trend that more mode-shapes are needed to calculate accurate response for long-spanned bridges is evident and can be explained by the low eigenfrequencies.

6.3.3 Variance vs. mean wind velocity

The variances vary with mean wind velocity. Figure 6.12 shows horizontal variance at mid-span with mean wind velocities between 5 and 30 m/s (bridge H). As expected, the variance increases with increasing mean wind. The variation between the bridges is expected to be small, therefore no comparison is made. The rest of the thesis focuses on a mean wind velocity of 30 m/s. Note that this is buffeting theory variances, vortex shedding is not included. Vortex shedding usually makes the variances at low mean wind velocities bigger.

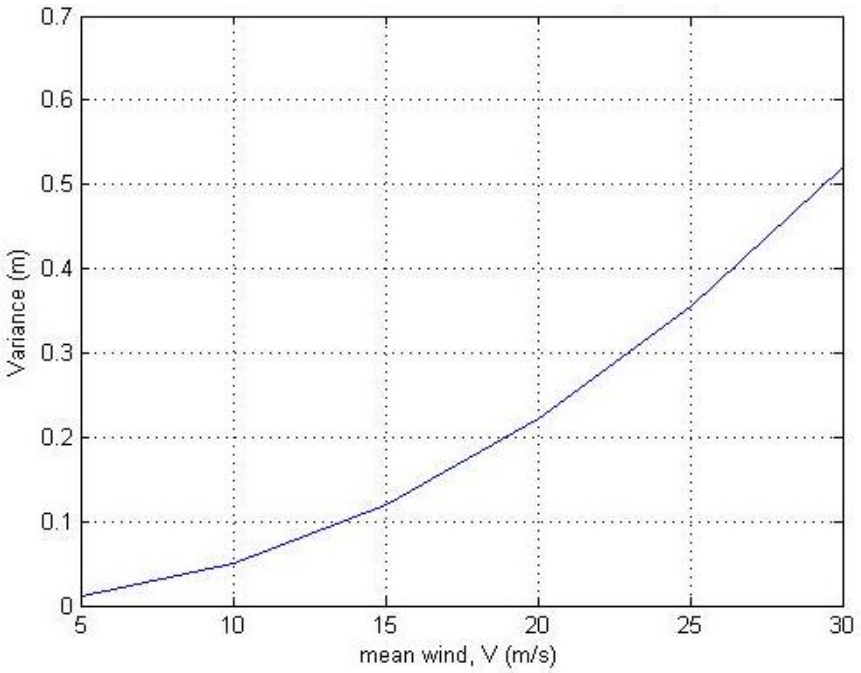

Figure 6.12 Plot of horizontal variance vs. mean wind velocity at mid-span, H

6.3.4 Variances over the span length

The variances are function of the longitudinal coordinate along the girder, x_r, because the mode-shapes are functions of x_r as explained in section 2.2. This gives the possibility of showing the variance over the span length. Figure 6.13 show horizontal variance at different locations on the bridge for a mean wind velocity of 30 m/s (bridge H). Figure 6.14 shows torsional and figure 6.15 shows vertical variance distribution. Note that the bridge is 3700m long.

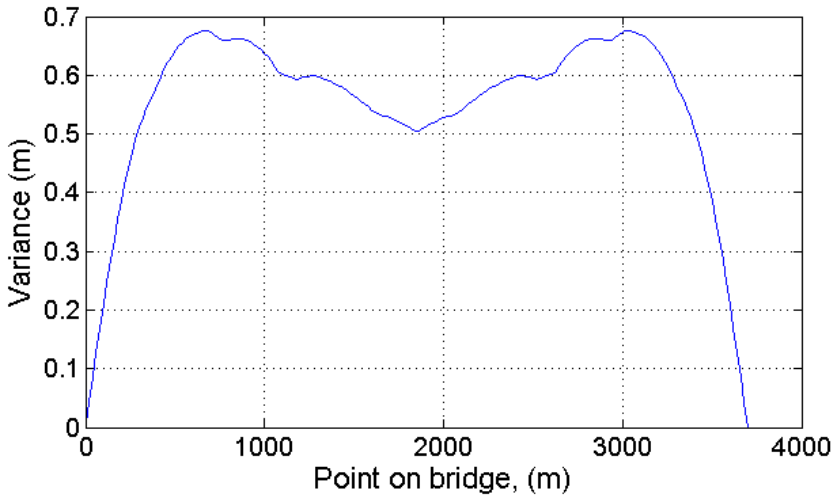

Figure 6.13 Plot of horizontal variance over the span of the bridge a V=30 m/s for bridge H.

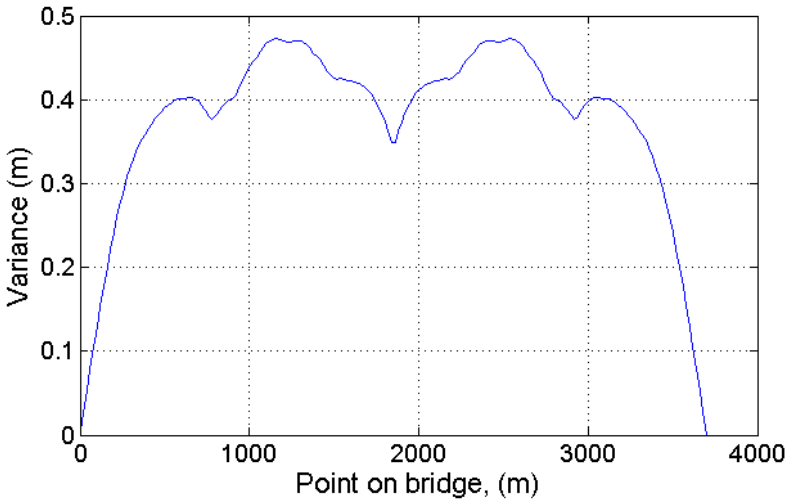

Figure 6.14 Plot of vertical variance over the span of the bridge a V=30 m/s for bridge H.

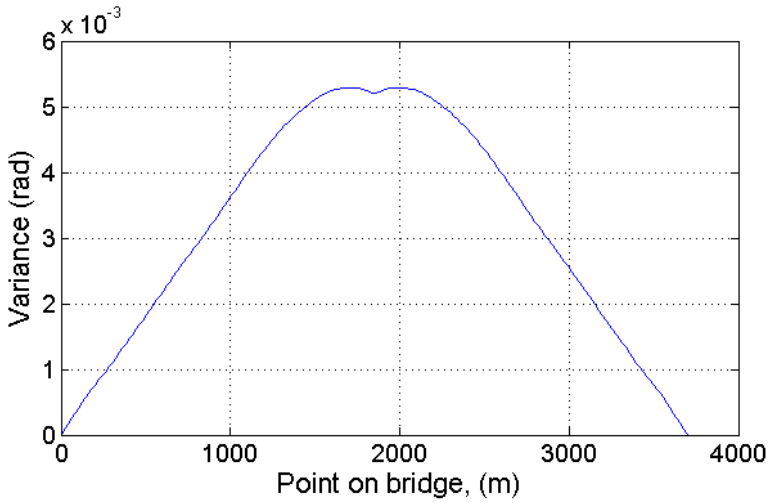

Figure 6.15 Plot of rotational variance over the span of the bridge V=30 m/s for bridge H.

The variances have one or more drops over the span length. This has to do with how the modes are shaped. An unsymmetrical mode-shape has zero displacement at mid-span, making the variance at mid-span zero for this mode.

The choice of using midpoint as a measure for the variance, with the intent to find the largest variance, is not always good. The biggest difference is for the vertical direction with a 35% difference in max variance vs. midpoint variance.

In figure 6.16 the torsional variance for TF is shown, it is seen that a mode-shape with high eigenfrequency is influential because of the many peaks. It is mode-shape 30 that stands out in the modal variance distribution. This can be seen from the total value of the variances.

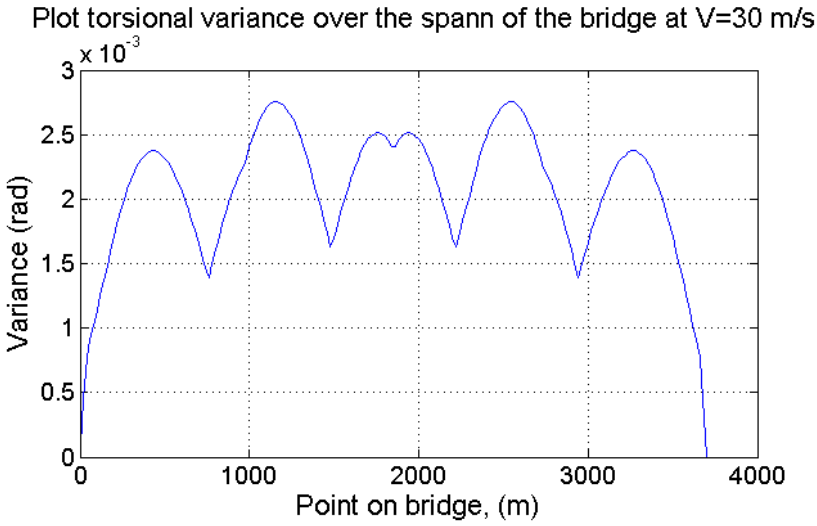

Figure 6.16 Plot of rotational variance over span of the bridge at V=30m/s, for bridge TF

HM has a bigger drop in torsional variance at mid-point than H. The modal coupling between horizontal and torsional direction is one of the factors contributing here. The increased torsional stiffness of the mono-cables at mid-span because the cable has to twist contributes

as well. The increased torsional stiffness favors the unsymmetrical modes, which have zero value at mid-span, making the drop bigger.

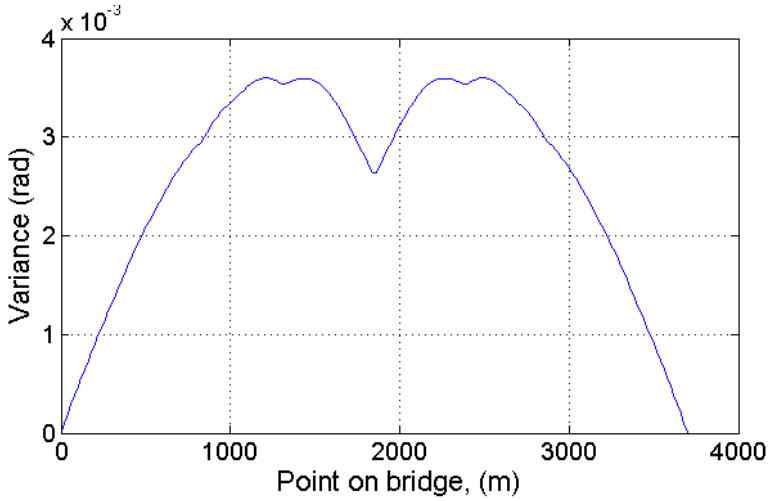

Figure 6.17 Torsional variance over the span for bridge HM at V=30 m/s

The effect described in the section above would probably be expected in TFM also, but the distance between the girder and the cable in the TFM model is 12 m higher than for the HM model. This is because the girder is 37m wide for the TFM model and need a larger distance between the girder and the cable to avoid interference of the inclined hangers with the roadway.

For bridges with mono-cable it is recommended that the cable-girder distance at mid-span is made as small as possible. How this is done practically is not looked into, but this will decrease the torsional rotation at mid-span.

All the plots of span-vise variance can be found in appendix B3.

6.3.5 Spectral density of the response

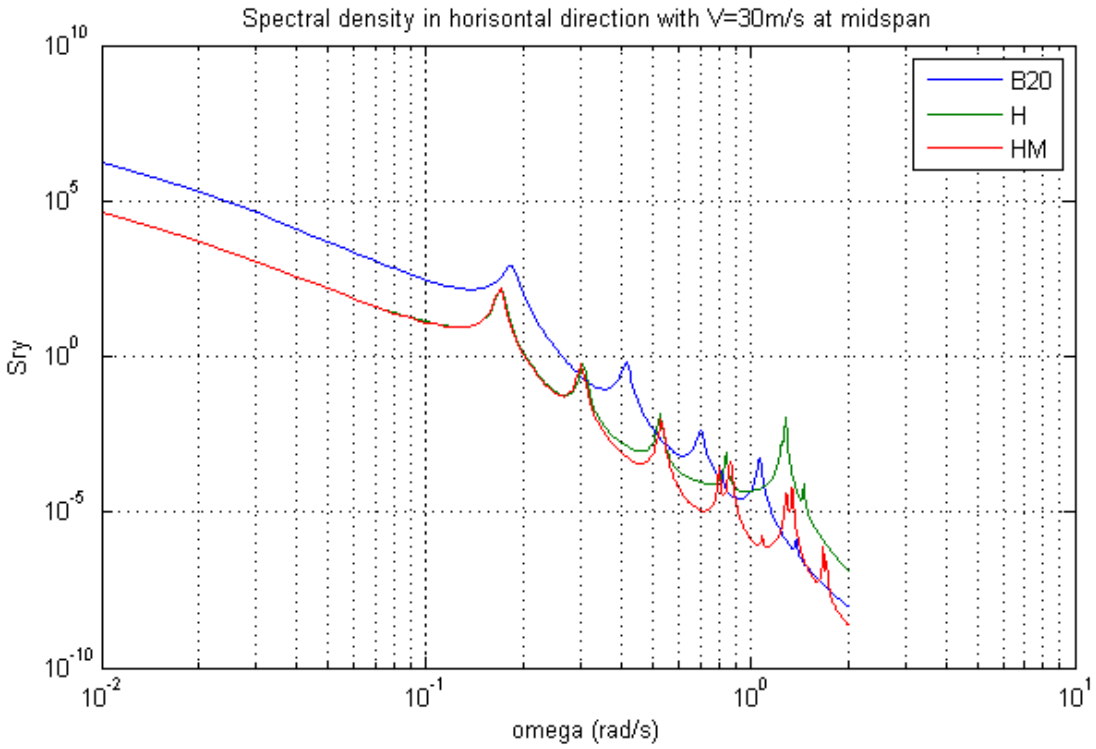

Figure 6.18 Spectral density for the response in horizontal direction, at mid-span for mean wind velocity at 30 m/s, for bridge H HM and B20

Figure 6.18 shows the spectral density for the response in horizontal direction at mid-span for models H, HM and B20. The spectral density of the load in figure 2.6 is recognized by the increased values at low frequencies. A combination of modal variance contribution and the modal frequency-response-function is also recognized by the peaks at the eigenfrequencies that contribute to the variance. From figure 6.18, it is seen that the B20 model has a higher overall spectral density; this will contribute to a larger variance in the horizontal direction for B20 compared to H and HM.

The spectral density function shows the variance contribution as a function of the frequencies. The frequency range with big contributions to the variance varies little between the different models. The total amount of variance for the different models is discussed in section 6.3.7. All the spectral densities can be found in appendix B1.

6.3.6 Static response from the mean wind velocity

Table 6.5 Static displacement at midpoint for mean wind velocity, V = 30 m/s

Model	H	HM	TF	TFM	B20	B30
Uz [m]	-0.8	-0.8	-0.07	-0.07	0.2	-0.2
Uy [m]	6.1	5.5	3.8	3.6	9.2	8.9
θ [rad]	0.009	0.018	0.004	0.014	0.005	0.0012

Table 6.6. Static displacements in horizontal direction without drag force on the cables.

Model	H	HM	TF	TFM	B20	B30
Uy [m]	3.9	4.1	2.5	2.7	7.0	6.9

Table 6.5 shows the static displacement at midpoint for mean wind velocity, V=30 m/s.

When comparing the results from table 6.6 with the horizontal displacement in table 6.5 it is seen that the drag-force on the cables contributes more to the response for the models with two cables than for the mono-cable models.

The static forces depend on the static force coefficients found in table 3.2. Note that the bridges use different widths and depths (B and D), making a direct comparison of the coefficients wrong.

For H vs. HM:
The rotation is much bigger for HM than H, this can be explained by the coupling effect between horizontal displacement and rotation for the mono-cable model, see section 2.2.10.

For TF and TFM:
The rotational effect seen in HM vs. H model is also seen here.

B20 and B30:
The increased distance between the girders gives an increased horizontal stiffness of the girder for B30. The increased stiffness gives little effect on the static displacement implying that the horizontal stiffness of the bridge comes mainly from the cable. As mentioned in section 3.5, a writing error in the lift coefficients for the B20 model is suspected, this would explain the difference in vertical displacement.

6.3.7 Variances at mid-span

Table 6.7 shows the different variances for the different models at mid-span for a mean wind velocity at 30 m/s.

Table 6.7 Variances of the different models at mid-span for V=30 m/s

Model	Variance-y	Variance-z	Variance-θ
H	0,51	0,35	0,0052
HM	0,50	0,36	0,0026
TF	0,28	0,02	0,0024
TFM	0,37	0,02	0,0049
B20	0,73	0,22	0,0027
B30	1,04	0,24	0,0033

The variances from the models H, HM and B20 are compared in detail. Bridge H is included to get a comparison between the mono-cable and the two-cable system. The vertical variance is not evaluated.

Table 6.8 Comparison table of 3 bridges, in horizontal direction, 2 most important modes, V=30m/s at mid-span

B20

Mode	omega	K	omegaae	Kae	Cae	PhiH(max)	Int of H and JJ	Int H	Int JJ	Phih(midpoint)	Var contrib.	% of total
1	0.1851	882400	0.1844	0.0000	-0.0374	1.0000	0.0638	0.8241	0.0168	99 %	0,6361	87 %
3	0.4151	2102500	0.4148	-0.0001	-0.0232	0.9999	0.0426	1.9706	0.0146	54 %	0,0632	9 %

HM

Mode	omega	K	omegaae	Kae	Cae	PhiH(max)	Int of H and JJ	Int H	Int JJ	Phih(midpoint)	Var contrib.	% of total
1	0.1701	952200	0.1694	0	-0.0209	1.0000	0.0143	0.8419	0.0037	98 %	0,4093	82 %
3	0.3001	1189000	0.3007	0	-0.0144	0.9998	0.0102	1.5594	0.0034	52 %	0,0601	12 %

H

Mode	omega	K	omegaae	Kae	Cae	PhiH(max)	Int of H and JJ	Int H	Int JJ	Phih(midpoint)	Var contrib.	% of total
1	0.1701	982100	0.1706	0	-0.0203	1.0000	0.0145	0.8520	0.0038	100 %	0,4027	80 %
3	0.3051	1210700	0.3051	0	-0.0143	0.9996	0.0106	1.5835	0.0036	53 %	0,0581	12 %

In figure 6.8, the two most important mode-shapes in horizontal direction are compared. Omegaae is defined as the frequency where the modal frequency-response-function has its maximum (with aerodynamic damping and stiffness). The int JJ is the joint acceptance function integrated over the frequency, and Int H is the modal frequency-response-function integrated over the frequency. Int of H and JJ are the integral that appears in the equation of variance, see equation (2.34). Phih is the value of the mode-shape at midpoint compared with the max value, PhiH(max).

Bridge H and HM has similar numbers and will not be compared further. It is noted that Kae for the bridges is not zero, but the values are so small that the round of makes them zero.

When comparing the H and B20 one thing that stands out is the Int JJ. It is much higher for B20, making the response higher for B20 than for H. If equation (2.39) is analyzed further, it is seen that $\mathbf{I}_v^2, \hat{\mathbf{S}}_v$ is the same for both cross sections. The $\hat{\mathbf{B}}_q$ matrix has to be one of the

deciding factors. If $\hat{\mathbf{B}}_q$ is studied, it is seen that it is the static force coefficients that determine the matrix. Mode-shapes, φ, also affect the joint acceptance function.

Figure 6.19 shows a plot of the joint acceptance function for mode shape number 1 for both B20 and H. It is clear that the B20 bridge has overall higher values of the joint acceptance function.

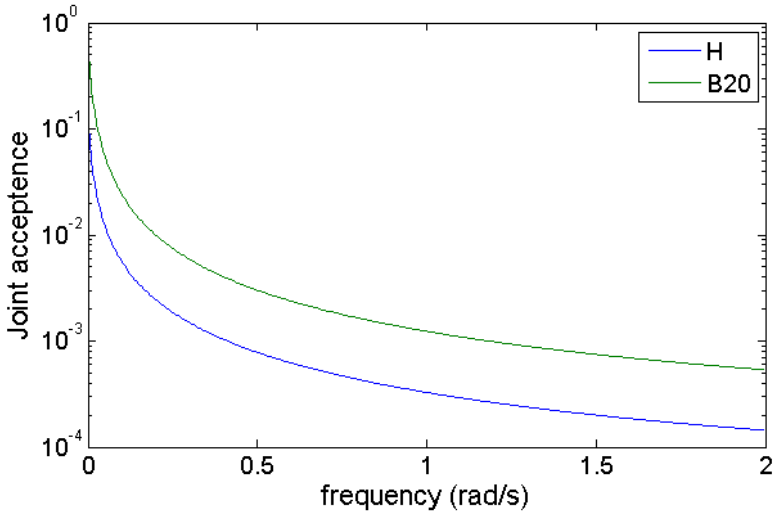

Figure 6.19 Joint acceptance function of B20 and H bridges, mode 1, V=30m/s

Table 6.9 Torsional comparison, V=30m/s, mid-point, H and HM bridge

HM

Mode	omega	K	omegaae	Kae	Cae	PhiT(max)	Int of H and JJ	Int H	Int JJ	Phit(midpoint)	% of max	Var contrib.	% of total
1	0.1694	9500000	0.1701	0	-0.0209	0,0031	0.0143	0.8419	0.0037	0,0030	97 %	0,0013	50 %
3	0.3007	1,2E+08	0.3001	0	-0.0144	0,0050	0.0102	1.5594	0.0034	0,0028	56 %	0,0003	12 %
11	0.8015	6,7E+08	0.8001	0	-0.0013	0,0227	0.0505	4.8403	0.0173	0,0227	100 %	0,0004	15 %

H

Mode	omega	K	omegaae	Kae	Cae	PhiT(max)	Int of H and JJ	Int H	Int JJ	Phit(midpoint)	%of max	Var contrib.	% of total
1	0.1706	9820000	0.1701	0	-0.0203	0,0018	0.0145	0.8520	0.0038	0,0018	100 %	0,0007	13 %
19	1.2138	5,4E+07	1.2151	0	-0.0004	0,136	0.1376	7.1774	0.0579	0,136	100 %	0,0014	27 %
23	1.2848	4,2E+08	1.2851	0	-0.0016	0,1286	0.0383	7.2454	0.0173	0,1286	100 %	0,0015	29 %

In table 6.9, the three most important torsional mode shapes for HM and H is evaluated. If mode 1 for both models is compared, the separating factor for the difference in variance contribution is definitely the size of the mode-shape at midpoint. The reason for the mode shape difference is explained by the modal coupling described in section 2.2.10.

The increased eigenfrequencies for mode-shape 19 and 23 of model H is compensated with purer torsional mode-shapes giving fairly low stiffness and a high PhiT. This contributes to higher variance.

The HM model lacks the pure torsional mode-shapes the H model has. This means that to rotate the cable as mentioned in section 2.2.10 demands high energy, indicating increased stiffness.

6.3.8 Combined response

Table 6.10 gives the total displacement in the different directions. The peak factor combining the dynamic and static response is set to be 3.5.

Table 6.10 Combined static and dynamic displacement at mid-span for V=30 m/s

Model	Total displ y	Total displ z	Total rotation
H	7,9	-2,0	0,027
HM	7,3	-2,0	0,027
TF	4,8	-0,1	0,012
TFM	4,9	-0,1	0,031
B20	11,7	1,0	0,014
B30	12,5	-1,0	0,013

6.3.9 Serviceability

Max displacement: Since the span length is 3700m, maximum allowed displacement with L/200 is 18.5 m. In table 6.11, the static and dynamic response contributions are combined again, but now with a 30 % increase in the dynamic parts. This increase takes into account the span-vise maximum, together with a decrease in maximum static displacement.

Table 6.11 Static displacement with 30 % increase in the dynamic parts

Model	Total displ y (m)	Total displ z (m)
H	8,4	-2,4
HM	7,8	-2,4
TF	5,1	-0,2
TFM	5,3	-0,2
B20	12,5	1,2
B30	13,6	-1,3

To find the total displacement the values in table 6.11 are added together with pythagoras. This gives 13.7 m as total displacement for the B30 model. From this it is shown that the max displacement is lower than the requirement for all the bridge models.

Acceleration comfort: Table 6.12**Feil! Ugyldig selvreferanse for bokmerke.** shows the maximum acceleration in vertical and horizontal direction after a RMS sum. This is checked against the requirements of (Iso6897, 1984).

Table 6.12 Acceleration table for check against comfort limit

Cross-section	Acceleration $(m/s^2)^2/s$	Frequency (Hz)	Requirements met?
H	0,0466	0,0748	Ok
HM	0,0614	0,07323	Ok
TF	0,0000597	0,03	Ok
TFM	0,0000445	0,03	Ok
B20	0,0175	0,077	Ok
B30	0,0322	0,068	Ok

The requirement for the acceleration is dependent on the frequency. The acceleration specters usually have more than one peak, so this causes a problem when comparing the results to the requirement. The peaks in vertical and horizontal directions are not at the same frequency, so the RMS sum is taken at least twice for each bridge. Figure 6.20 shows an example of an acceleration specter for H.

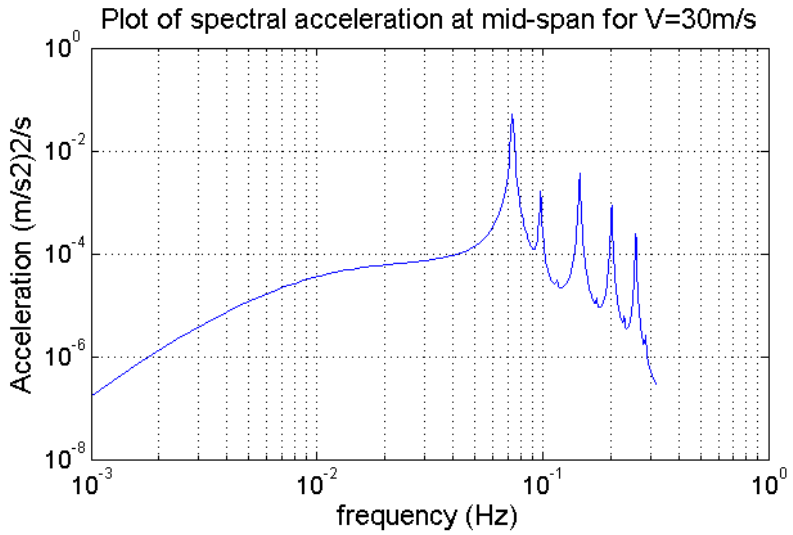

Figure 6.20 Spectral acceleration density for vertical direction, at mid-span for V=30 m/s, HM

6.3.10 Verification of the model

The script made in Matlab is tested on different examples in the book, Theory of Bridge Aerodynamics (Strømmen, 2010), with good results. The script is built up from simple one mode one component response, to what it is now. By this way of writing the script, the authors have better control over the final results.

7 Conclusion

The traditional streamlined box section, H, does not have sufficient aerodynamic stability to be used in a 3700m long suspension bridge with the usual design. With use of a mono-cable instead of the traditional geometry with two cables, the critical velocity increases to above the stability limit for the single girder. All the slotted box section models have stability limits above the design velocity. The slotted models have been tested with the aerodynamic derivatives from the Hardanger Bridge and from these results it can be concluded that the increase in critical velocity for the slotted models manly comes from aerodynamic improvements. The increase in structural stiffness has minor influence on the flutter velocity.

The contribution from the horizontal movement is considerable for the HM model due to coupling effects between horizontal movement and torsional rotation; it increases this model's critical velocity by 10 m/s. This means using quasi static values for the aerodynamic derivatives related to the horizontal movement is not accurate enough. Therefore conducting new wind tunnel tests to obtain these values is recommended.

The results from tests on the TF section proved its stability satisfactory, but there would not be enough traffic across the Sogne Fjord to necessitate the construction of three lanes in each direction. Designing the bridge to be this wide would produce a more expensive structure, requiring needless amounts of steel. Since more slender girders show adequate results, these girders should be implemented, despite the TF section having a higher Vcr.

All the models satisfy the serviceability requirements of max displacement and max acceleration. The B20 and B30 models generate the biggest horizontal displacement, while the H and HM models generate the biggest vertical displacement.

The number of modes necessary to include in response calculations are higher for long-spanned bridges compared to bridges with shorter spans. This is true on account of the fact that long-span bridges have lower eigenfrequencies.

To find maximum displacements along the bridge a span-vise variance calculation should be executed. The maximum displacements are not located at mid-span because of contributions from asymmetrical mode-shapes.

The joint acceptance function containing the static force coefficients has the biggest influence on variations in the response between the models in horizontal and vertical directions. The difference in mode-shapes contributes to the variation in torsional rotation for the mono-cable models and two-cable models.

If the mono-cable is not fixed to the girder at mid-span there will be a relative displacement in the horizontal direction which leads to a rotation of the girder. Thus, a fixed connection at mid-span is recommended: it gives increased torsional stiffness to the girder and decreased torsional response.

The results indicate that the models HM and B20 give the best overall solutions. They show satisfactory results for both critical velocity and response, and would be more economic and elegant alternatives to a wider, more costly bridge.

In conclusion, crossing the Sogne Fjord with a suspension bridge is a feasible option, and would make Norway the owner of the longest bridge-span in the world.

7.1 Further work

The HM and B20 models should be investigated further. In regards to the HM model, structural improvements like tuned mass dampers and how to fix the connection between cable and girder at mid-span should be looked into.

There is no walking/cycling path for B20. An alternative might be to expand the box sections with a few meters for a cycling path on one girder and a walking path on the other. If further aerodynamic measures like a vertical plate in the middle are applied to the B20 section, the critical velocity could be increased further. On the B20 model, the girder should be enlarged and new wind tunnel tests with both guide vanes and a vertical plate should be conducted.

For the design of the bridges based on ultimate limit state, a multimode response calculation should be used. Vortex shedding should be investigated to find the correct response at low mean wind velocities.

8 Bibliography

CrossX Version 1.1. (2003). Kolbein Bell.

Chopra, A. (2007). *Dynamics of Stuctures.* Pearson Prentice Hall.

Gimsing, N. J. (1998). *Cable Supported Bridges.* John Wiley & Sons.

Hansen, D. a. (1999). *Wind loads on structures.* Chichester: John Wiley & Sons.

Iso6897. (1984). *"Guidelines for the evaluation of the response of occupants of fixed structures, especially buildings and off-shore structures, to low-frequency horizontal motion (0.063 to 1 Hz).".* Geneva: International Organization for Standardization,.

MathWorks. (2011). MATLAB R2011b. MathWorks, Simulink.

Mathworks. (2012). R2012a Matlab Documentation. Natick, Massachusetts, USA.

Matsumoto, S. E. (2007). On the flutter charachteristics of speoarated two box girders. *Wind and Stuctures Vol 7, no 4*, 281-291.

Miguel, A. (1998 August). Flutter stability of vero long suspension bridges. *Journal of brdge engineering*, 132-139.

Øiseth, O. A. (2012, March 20). Guidance appointment. NTNU.

Øiseth, R. S. (Volume 98, Issue 12, December 2010,). Simplified prediction of wind-induced response and stability limit of slender long-span suspension bridges, based on modified quasi-steady theory: A case study. *Journal of Wind Engineering and Industrial Aerodynamics*, Pages 730–741.

Øiseth, S. (2011, 330). An aletrnative analytical approach to prediction of flutter stability limits of cable suppoerted bridges. *Journal of Sound and Vibration* , 2784-2800.

Salvatoru, B. (2007). Frequency- and time-domain methods for numerical modeling of full-bridge aeroelasticity. *Computers and Structers 85*, 675-678.

Sato, H. (2002). Full aeroelastic model test of super long-span bridge with slotted box girder. *Journal of Wind Engineering and Idustrial Aerodynamics 90*, 2023-2032.

Scanland RH, T. J. (1971). Airfoil and bridge deck flutter derivatives. *Journal of the Engineering Meckanics Dicision*, ss. 97:1717-37.

SIMULA. (2010). Abaqus. USA: Dessault Systèmes.

Standard1995-1-1. (2009). *Eurokode 5, Prosjektering av trekonstruksjoner Del 1-1.* Standard Norge.

Strømmen. (2010). *Theory of Bridge Aerodynamics 2nd Edition.* Trondheim: Springer.

Trein, S. (2011). Coupled flutter stability from the unsteady pressure characheristics . *Journal of Wind Engineering an Industrial Aerodynamics 99*, 114-122.

Vegdirektoratet, B. i. (2008). *Hardangerbrua beregninger kap1: grunnlag.* Vegvesen Statens.

Vegdirektoratet, B. i. (2011). *Hardangerbrua, komplett tegningsliste.* Statens Vegvesen.

Vegvesen, S. (2005). *Brusymfonien:Static and dynamic wind tunnel tests with a section model.* Wind engineering fluid dynamics: Svend Ole Hansen.

Xiang Haifan, G. Y. (2007). *Aerodynamic challenge in span length of spuspension bridges.* Higher Education Press and Springer-Verlag.

9 Appendix

Appendix A

A1 The design velocity for the Sogne Bridge

A2 Design of crossbeam for slotted box girders

A3 Geometric data for the different models

A4 Aerodynamic derivatives

Appendix B

B1 Spectral densities

B2 Modal variance contribution

B3 Variance over span length

B4 Modal frequency-response-function

B5 Spectral density for the first 5 modes in horizontal direction

B6 comparison of frequency step

Appendix A

A1 The design velocity for the Sogne Bridge

The critical velocity of the area where the Sogne Bridge is being build is calculated according to Euro Code 1-2.

$Vcr > 1.5\ V_{10}$ EC 1-2, 6.4.3.2

$V_{10} = V_s(z) = C_r(z) * V_b$

$V_b = c_{ret} * c_{års} * c_{san} * V_{REF}$

$c_{ret} = c_{års} = c_{san} = 1$

The bridge is going to be built in Gulen kommune, here the reference velocity is V_{REF}=28m/s.

V_b=28m/s

$C_r(z) = k_T * \ln(z/z_0)$ z equals the height above ground.

For terrain category 1: k_T=0.17 and z_0=0.01

Assume that the bridge girder will be at a height around 80m above the water level of the fjord, z=80m.

$C_r(80m) = 0.17 * \ln(80/0.01) = 1.53$

$V_{10}(80m) = 28m/s * 1.53 = 43m/s$

<u>$Vcr > 1.5 * 43m/s = 64.2\ m/s$</u>

A2 Design of crossbeam for slotted box girders

Assume a simply supported beam between the hangers, contribution from 20 m of girder and two trucks on the girders.

Calculation for the TF section:

q_g= 5928 kg/m*9.81 m/s^2*2*1.2*20m/36.5m+0.112 m^2*7.5 m*7850 kg/m3*9.81m/s^2*1.2 /36.5 m =76 476 N/m +1 772 N/m = 78.3 kN/m

q_e= 2900kg/m*9.81 m/s^2*2*1.6*20m/36.5m= 50 kN/m

q_t=210 kN*3*2*1.3/36.5 m= 45 kN/m

q_{tot}= 78.3+50+45= 173.3 kN/m

M_{midt}= 173.3 kN/m*36.5^2m^2/8 = 28 860 kNm

I=1/6*[1m*0.02^3m^3+0.012*2.96^3m^3]+0.02m*1m*1.49^2m^2=0.14m^4

σ= 28 860 kNm*1.5m/0.14m^4= 309 MPa

σ_{fy}= 355>σ

Calculation for the B30 section:

q_g = 2000 kg/m*9.81 m/s^2*2*1.2*20m/36m+0.135 m^2*25m*7850 kg/m3*9.81m/s^2*1.2 /36 m =26 160 N/m +8 660 N/m = 34.8 kN/m

q_e = 1560kg/m*9.81 m/s^2*2*1.6*20m/36m= 27 kN/m

q_t =210 kN*3*2*1.3/36 m= 45 kN/m

q_{tot} = 34.8+27+45= 106.8 kN/m

M_{midt} = 106.8 kN/m*36^2m^2/8 = 17 300 kNm

I=1/6*[1m*0.03^3m^3+0.015*2.5^3m^3]+0.03m*1m*1.25^2m^2=0.133m^4

σ= 17 300 kNm*1.25m/0.133m^4= 163 MPa

σ_{fy} = 355>σ

The same cross beam is applied for the B20 model

A3 Geometric data for the different models

Model	H	HM	TF	TFM	B20	B30
Cable area [m^2]	2*0.3	0.6	2*0.56	1.12	2*0.3	2*0.3
Hanger area[m^2]	0.0032	0.0032	0.0032	0.0032	0.0032	0.0032
Girder area [m^2]	0.5813	0.5813	1.52	1.52	2*0.253	2*0.253
I_m girder[kgm^2/m]	222860	222860	2*222860	2*222860	2*21000	2*21000
Mass girder [kg/m]	8825	8825	2*8825	2*8825	2*3560	2*3560
Tower height [m]	440	460	440	460	440	460
Sag cable [m]	370	370	370	370	370	370
Girder height [1][m]	9	21	9	9	9	9

[1]The girder height at the middle relative to the girder height at the towers. The height for HM is higher than for TFM because the TFM slotted box girder is much wider than the HM girder and does not need that big distance between girder and cable due to hangers interfering with the roadway.

The margin for the cables is smaller than on the real Hardanger Bridge, here the factor is 1.5 multiplied with the calculated area.

A4 Aerodynamic derivatives

H section

```
P1*=-0.2548*vred;
P2*=0;
P3*=0;
P4*=0;
P5*=-0.25*vred;
P6*=0;
H1*=0.1184*vred.^2-3.1629*vred;
H2*=-0.3376*vred.^2+0.817*vred;
H3*=2.3738*vred.^2-0.1944*vred;
H4*=-0.1724*vred.^2-0.1315*vred;
H5*=0.5*vred;
H6*=0;
A1*=-0.0778*vred.^2-0.5406*vred;
A2*=-0.1375*vred.^2-0.0092*vred;
A3*=0.8789*vred.^2-0.2887*vred;
A4*=0.0595*vred.^2-0.3636*vred;
A5*=-0.0200*vred;
A6*=0;
```

TF section

```
P1*=0;
P2*=0;
P3*=0;
P4*=0;
P5*=0;
P6*=0;
H1*=-6/20*vred*pi*2;
H2*=40/16*vred*pi*2;
H3*=(0.11*vred^2*pi-0.42*vred)*pi*2;
H4*=2.5/20*vred*pi*2;
H5*=0;
H6*=0;
A1*=-9/30*vred*pi*4;
A2*=(-0.0467*vred^2*pi-0.167*vred)*pi*4;
A3*=(0.107*vred^2*pi+0.89*vred)*pi*4;
A4*=-0.5/20*vred*pi*4;
A5*=0;
A6*=0;
```

B20 Section

```
P1=0;
P2=0;
P3=0;
P4=0;
P5=0;
P6=0;
H1=-5.729*vred+ 3.038;
H2=-0.5045*vred^2+15.02*vred-9.846;
H3=3.537*vred^2+30.52*vred-35.02;
H4=(-3.702*vred + 1.872);
H5=0;
H6=0;
A1=-0.04092*vred^2+0.5411*vred-1.309;
A2=(-12.64*vred+ 13.12);
A3=(1.549*vred^2 -20.19*vred + 12.16);
A4=(-0.07704*vred^2+1.082*vred+1.14);
A5=0;
A6=0;
```

B30 Section

```
P1=0;
P2=0;
P3=0;
P4=0;
P5=0;
P6=0;
H1=(-5.202*vred+-12.25);
H2=(2.508*vred^2-9.335*vred +3.974);
H3=(4.326*vred^2+25.68*vred-0.6141);
H4=(-0.3208*vred^2+0.8535*vred+7.211);
H5=0;
H6=0;
A1=-0.02079*vred^2+1.846*vred+0.1454;
A2=(-1.353*vred^2+1.583*vred-5.848);
A3=(-2.956*vred^2+1.138*vred-1.383);
A4=(1.689*vred+7.981);
A5=0;
A6=0;
```

Appendix B

B1 Spectral densities

H

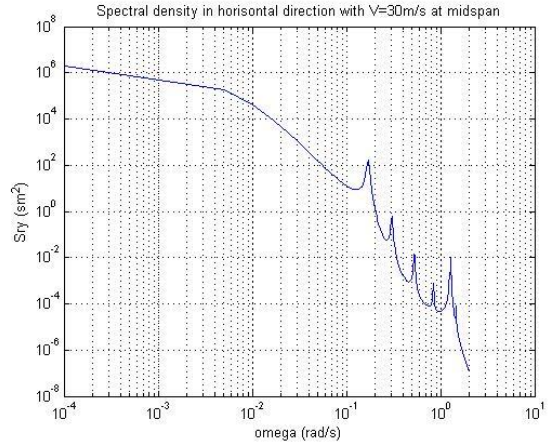

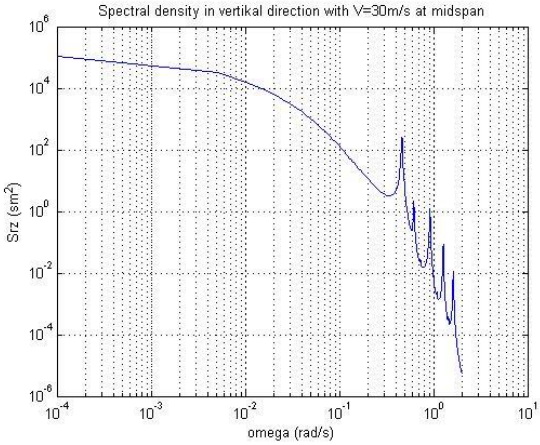

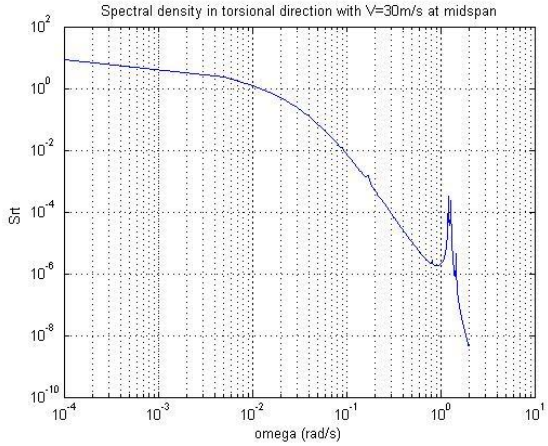

HM

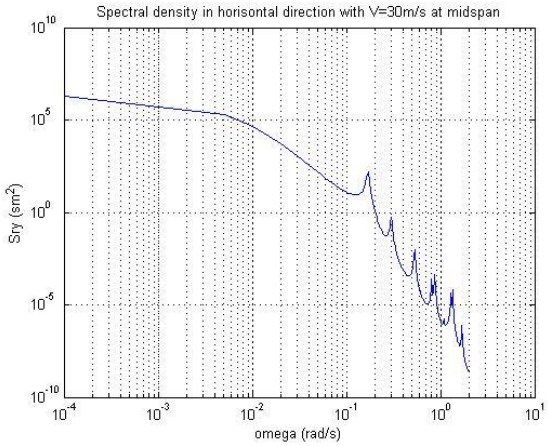

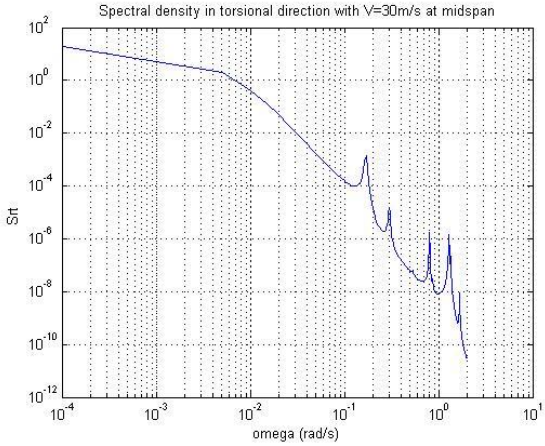

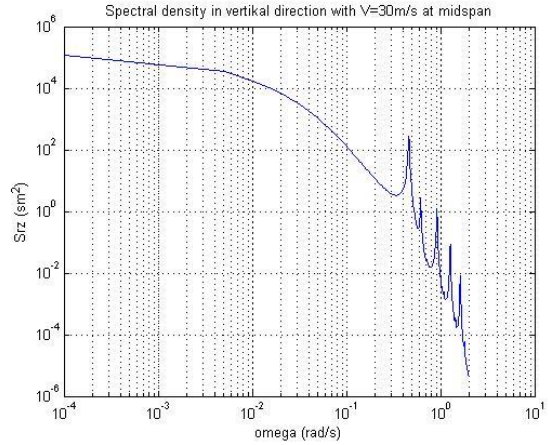
Spectral density in vertikal direction with V=30m/s at midspan
Srz (sm²)
omega (rad/s)

TF

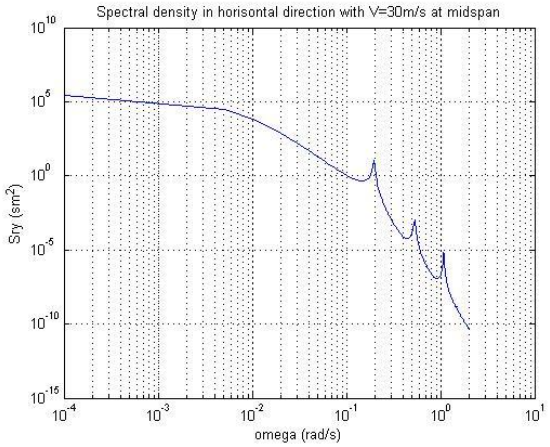
Spectral density in horisontal direction with V=30m/s at midspan
Sry (sm²)
omega (rad/s)

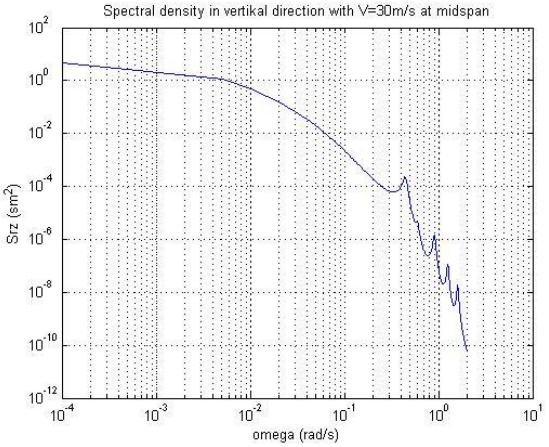
Spectral density in vertikal direction with V=30m/s at midspan
Srz (sm²)
omega (rad/s)

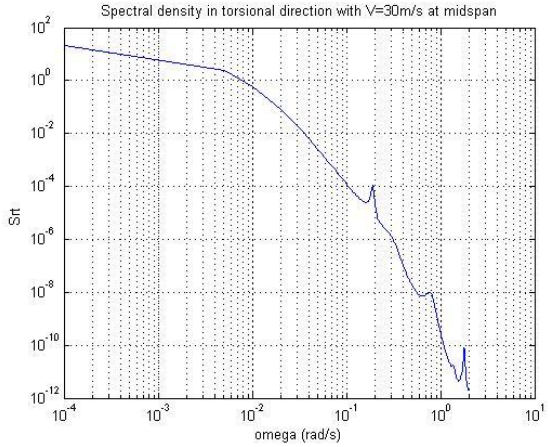
Spectral density in torsional direction with V=30m/s at midspan
Srt
omega (rad/s)

TFM

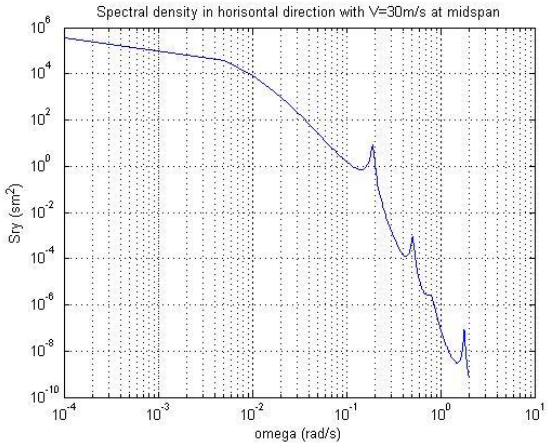
Spectral density in horisontal direction with V=30m/s at midspan
Sry (sm²)
omega (rad/s)

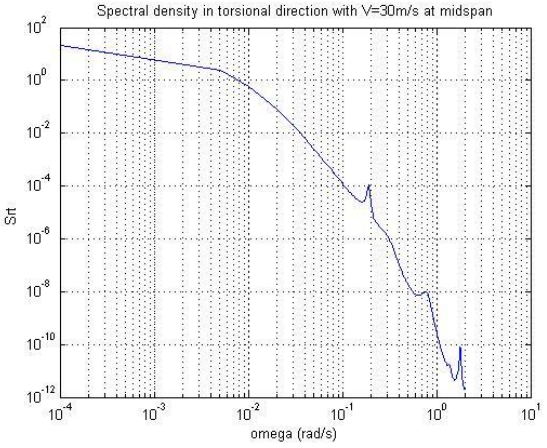
Spectral density in torsional direction with V=30m/s at midspan
Srt
omega (rad/s)

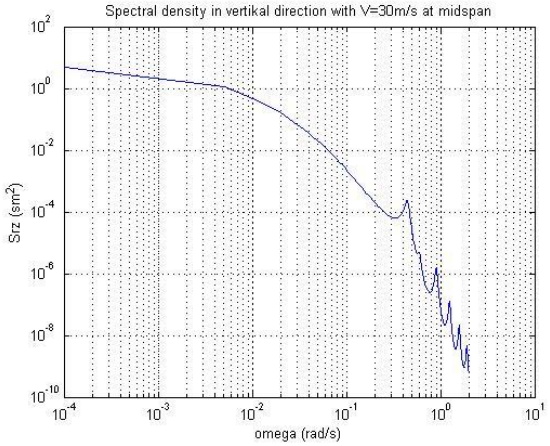
Spectral density in vertikal direction with V=30m/s at midspan
Srz (sm²)
omega (rad/s)

B20

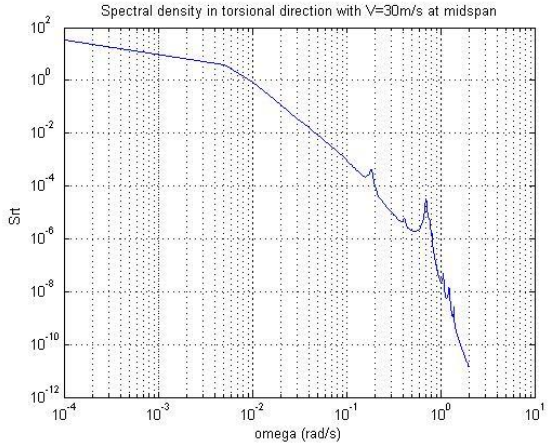
Spectral density in torsional direction with V=30m/s at midspan
Srt
omega (rad/s)

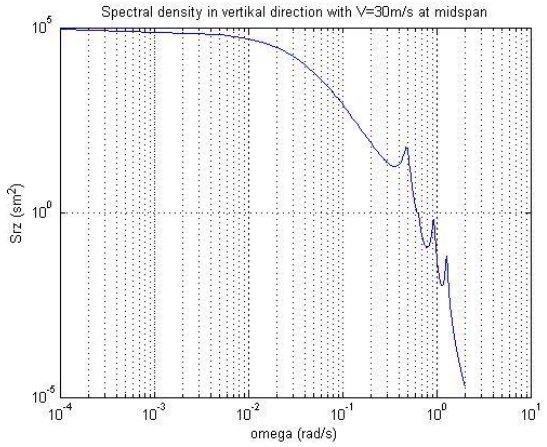
Spectral density in vertikal direction with V=30m/s at midspan
Srz (sm²)
omega (rad/s)

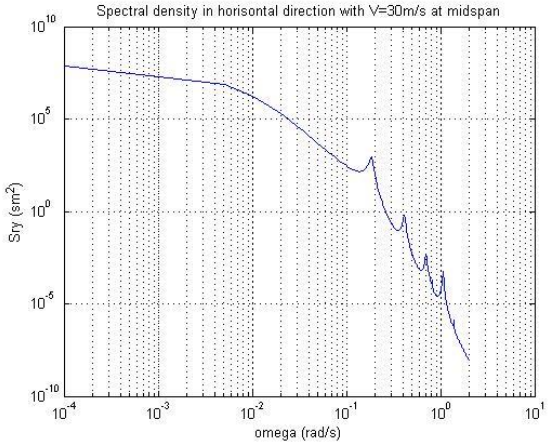
Spectral density in horisontal direction with V=30m/s at midspan
Sry (sm²)
omega (rad/s)

B30

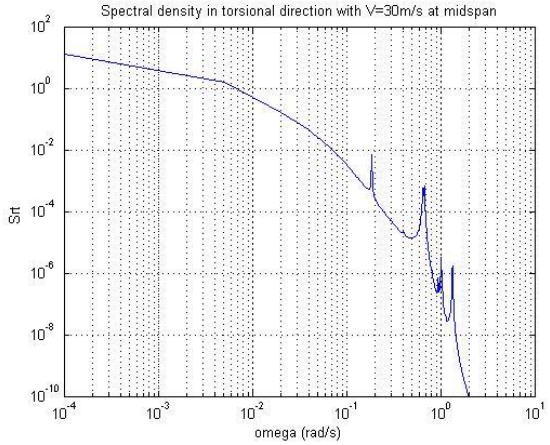
Spectral density in torsional direction with V=30m/s at midspan
Srt
omega (rad/s)

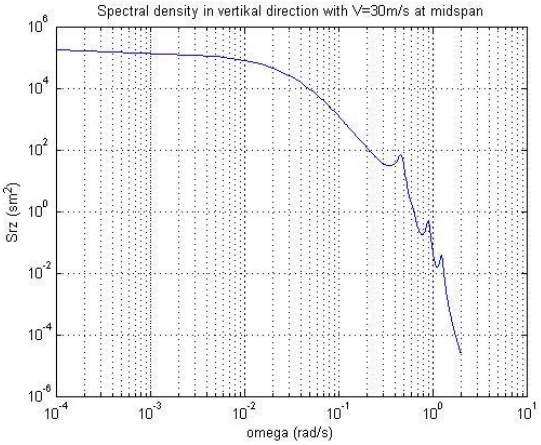
Spectral density in vertikal direction with V=30m/s at midspan
Srz (sm²)
omega (rad/s)

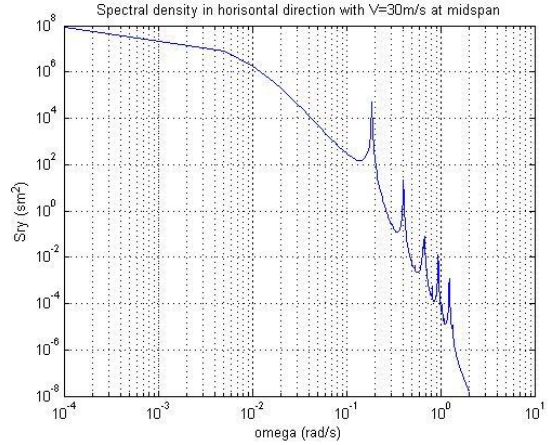
Spectral density in horisontal direction with V=30m/s at midspan
Sry (sm²)
omega (rad/s)

B2 Modal variance contribution

H

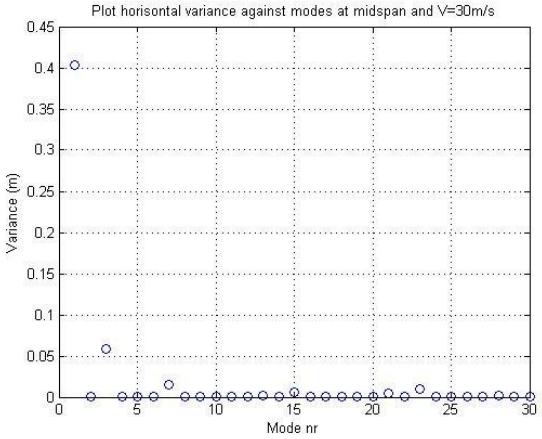

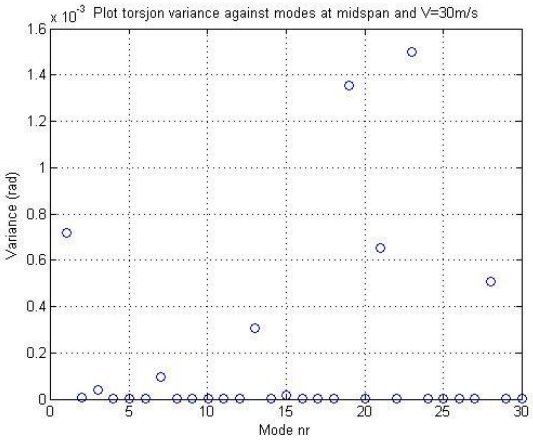

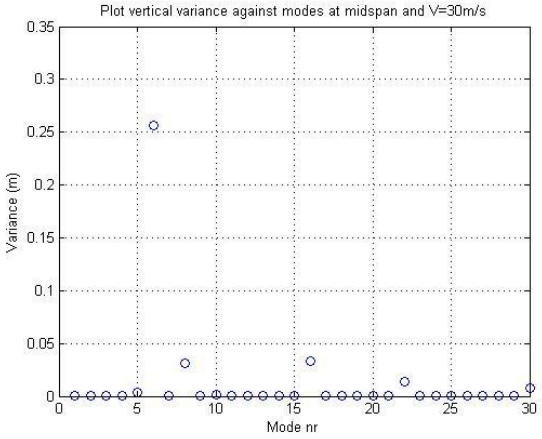

HM

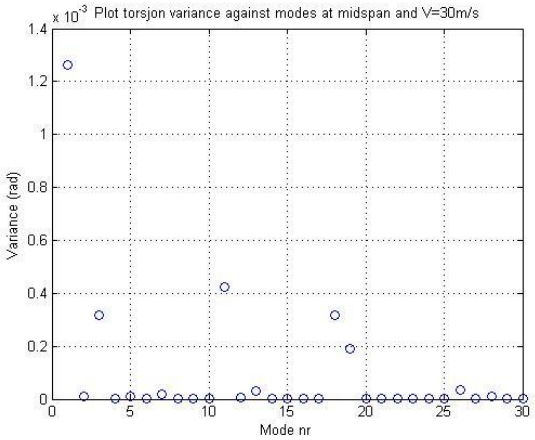

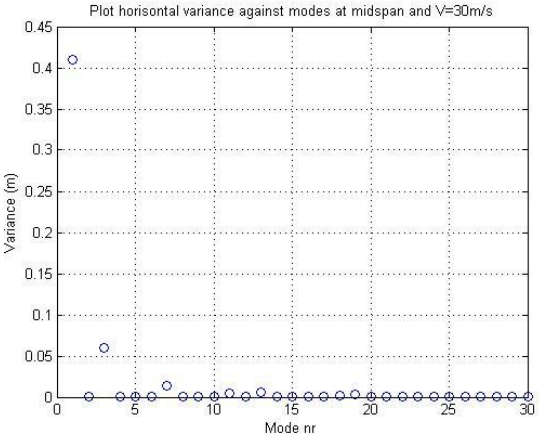

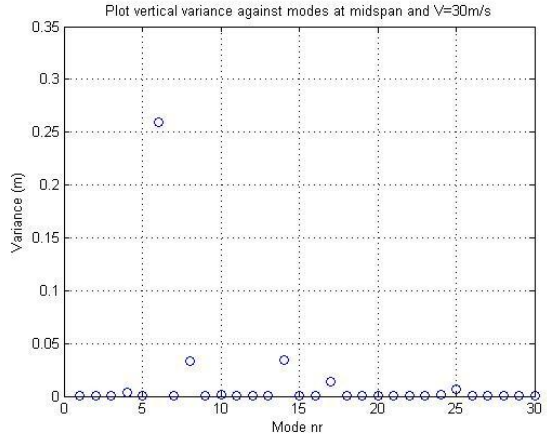
Plot vertical variance against modes at midspan and V=30m/s
Variance (m)
Mode nr

TF

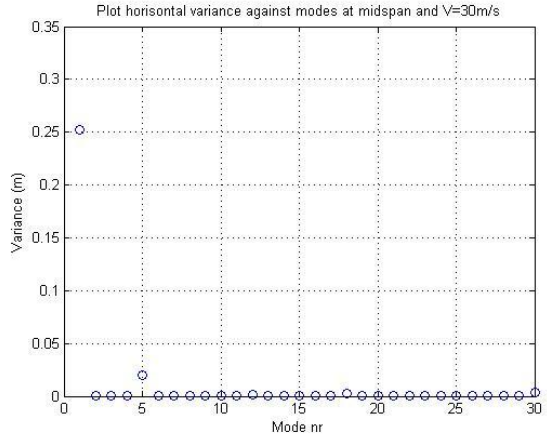
Plot horisontal variance against modes at midspan and V=30m/s
Variance (m)
Mode nr

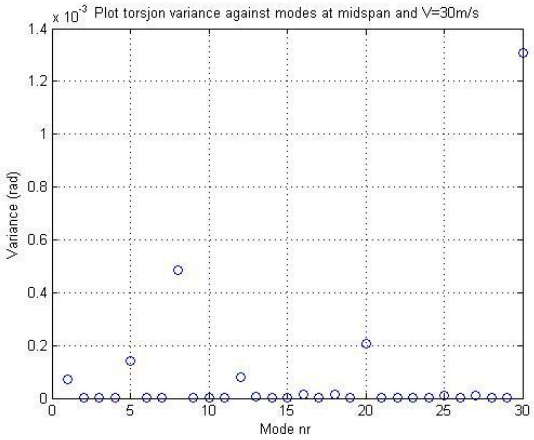
x 10^-3 Plot torsjon variance against modes at midspan and V=30m/s
Variance (rad)
Mode nr

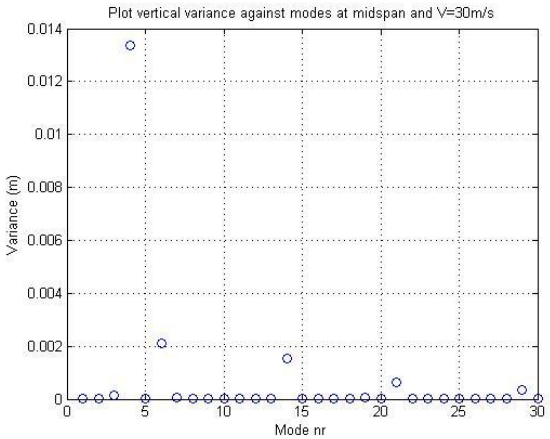
Plot vertical variance against modes at midspan and V=30m/s
Variance (m)
Mode nr

TFM

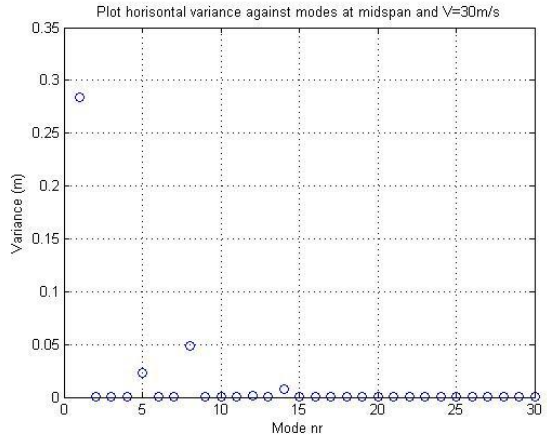
Plot horisontal variance against modes at midspan and V=30m/s
Variance (m)
Mode nr

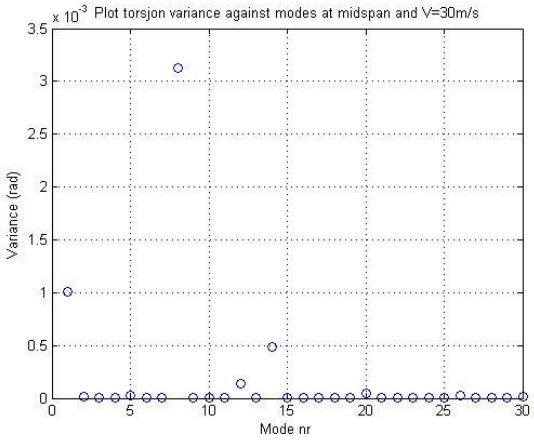
x 10^-3 Plot torsjon variance against modes at midspan and V=30m/s
Variance (rad)
Mode nr

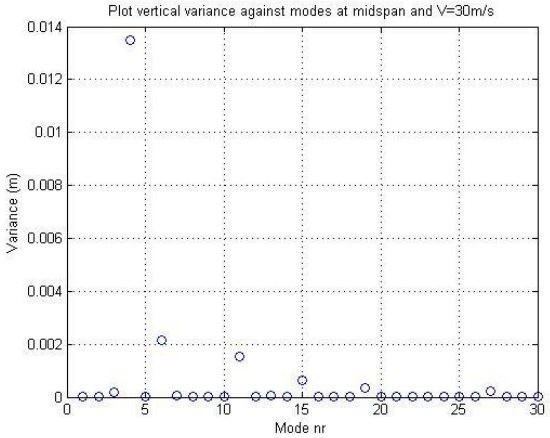
Plot vertical variance against modes at midspan and V=30m/s
Variance (m)
Mode nr

B20

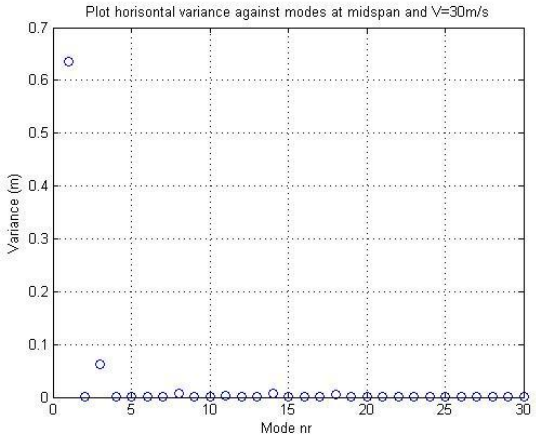
Plot horisontal variance against modes at midspan and V=30m/s
Variance (m)
Mode nr

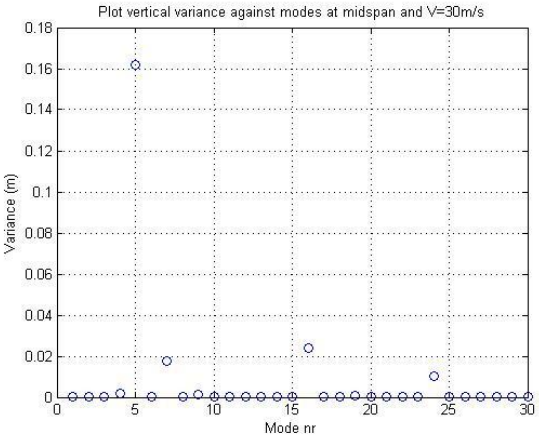
Plot vertical variance against modes at midspan and V=30m/s
Variance (m)
Mode nr

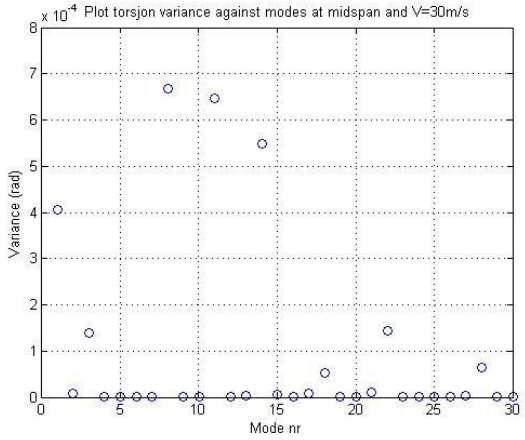
x 10^-4 Plot torsjon variance against modes at midspan and V=30m/s
Variance (rad)
Mode nr

B30

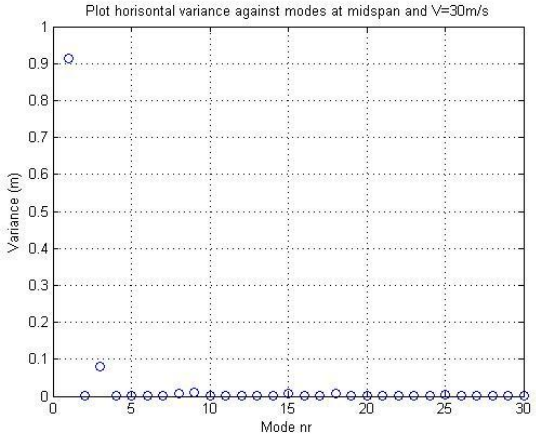
Plot horisontal variance against modes at midspan and V=30m/s
Variance (m)
Mode nr

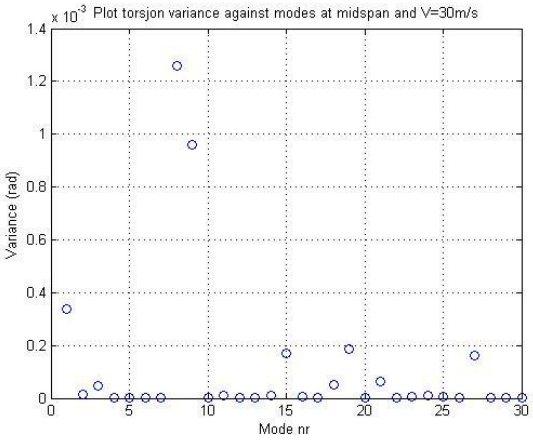
x 10^-3 Plot torsjon variance against modes at midspan and V=30m/s
Variance (rad)
Mode nr

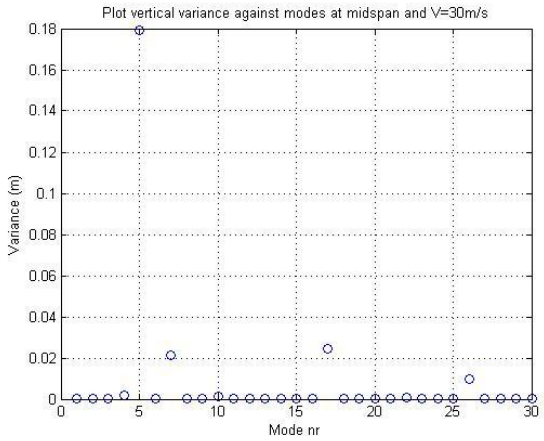
Plot vertical variance against modes at midspan and V=30m/s
Variance (m)
Mode nr

B3 Variance over span length

H

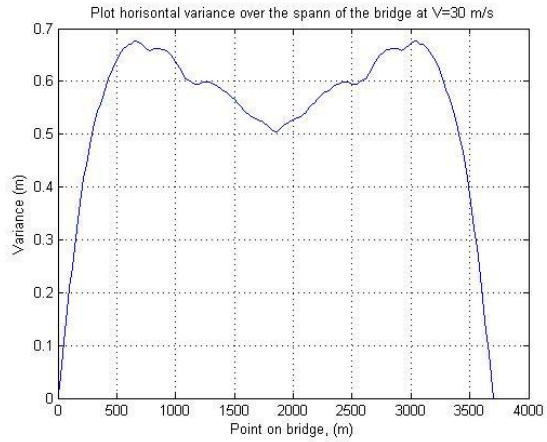

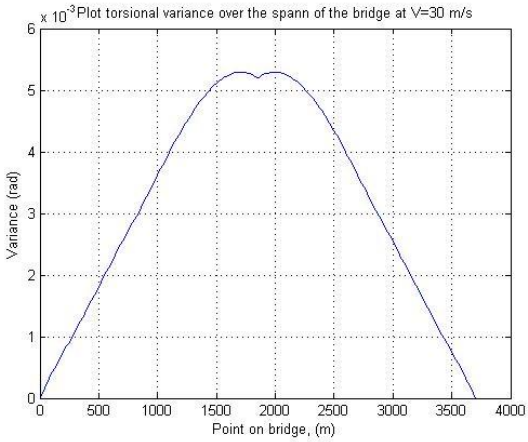

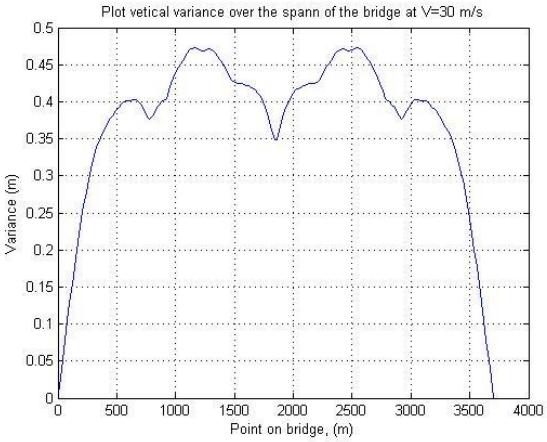

HM

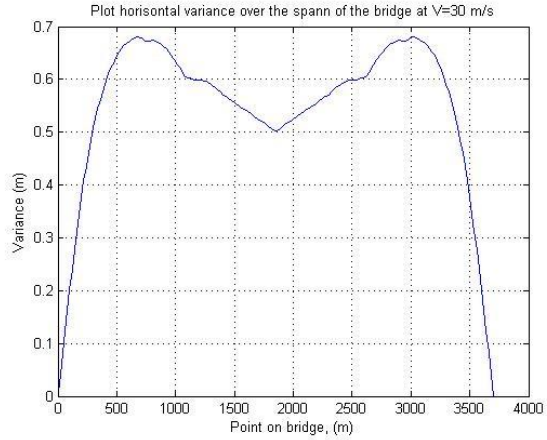

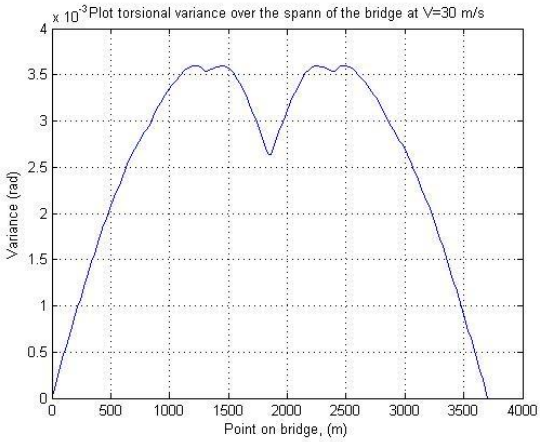

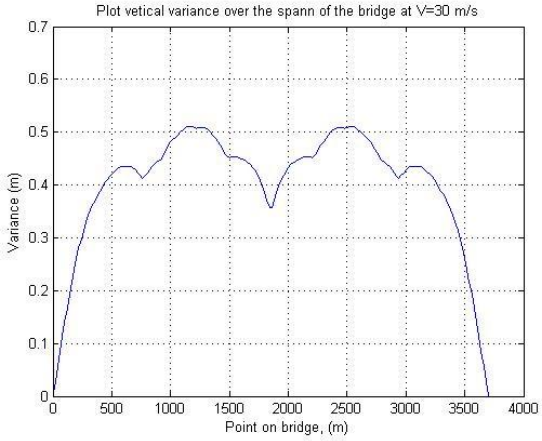
Plot vetical variance over the spann of the bridge at V=30 m/s
Variance (m)
Point on bridge, (m)

TF

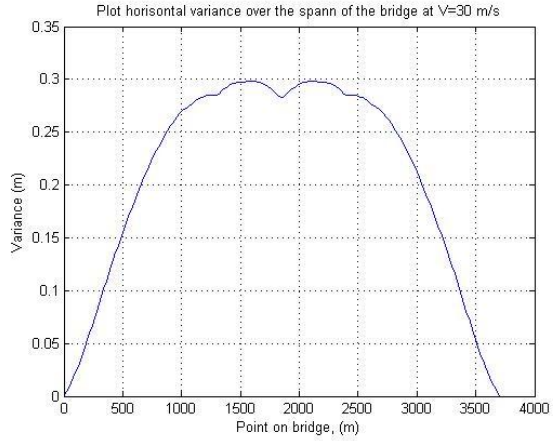
Plot horisontal variance over the spann of the bridge at V=30 m/s
Variance (m)
Point on bridge, (m)

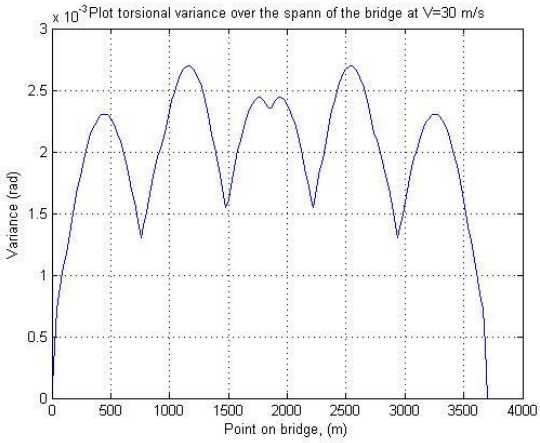
x 10^-3 Plot torsional variance over the spann of the bridge at V=30 m/s
Variance (rad)
Point on bridge, (m)

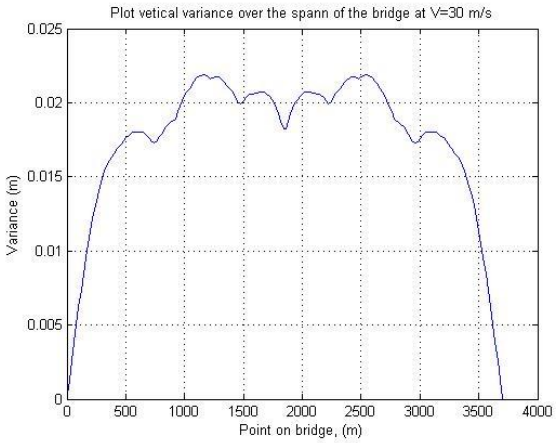
Plot vetical variance over the spann of the bridge at V=30 m/s
Variance (m)
Point on bridge, (m)

TFM

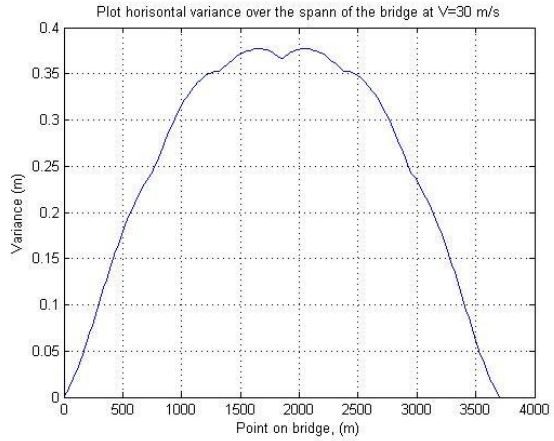
Plot horisontal variance over the spann of the bridge at V=30 m/s
Variance (m)
Point on bridge, (m)

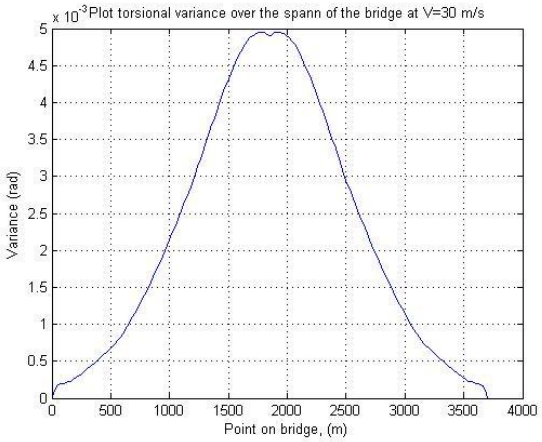
x 10^-3 Plot torsional variance over the spann of the bridge at V=30 m/s
Variance (rad)
Point on bridge, (m)

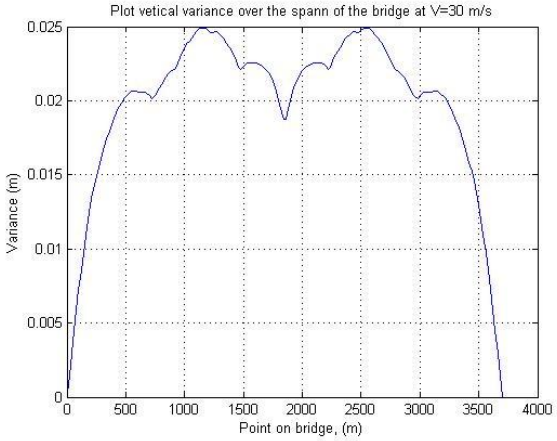
Plot vetical variance over the spann of the bridge at V=30 m/s
Variance (m)
Point on bridge, (m)

B20

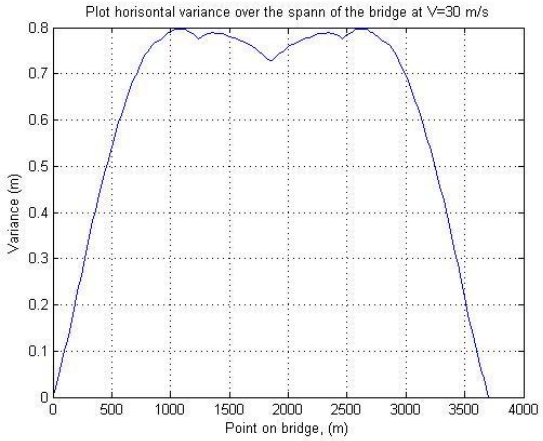
Plot horisontal variance over the spann of the bridge at V=30 m/s
Variance (m)
Point on bridge, (m)

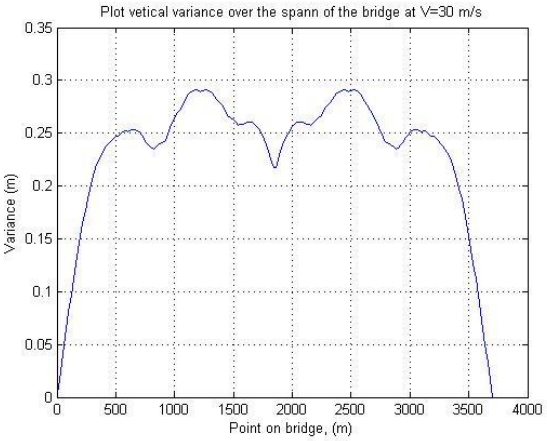
Plot vetical variance over the spann of the bridge at V=30 m/s
Variance (m)
Point on bridge, (m)

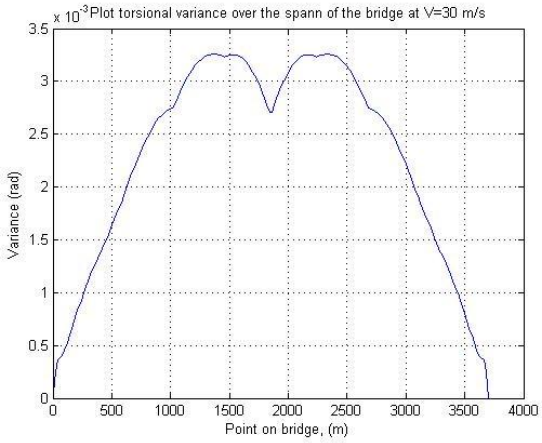
x 10^-3 Plot torsional variance over the spann of the bridge at V=30 m/s
Variance (rad)
Point on bridge, (m)

B30

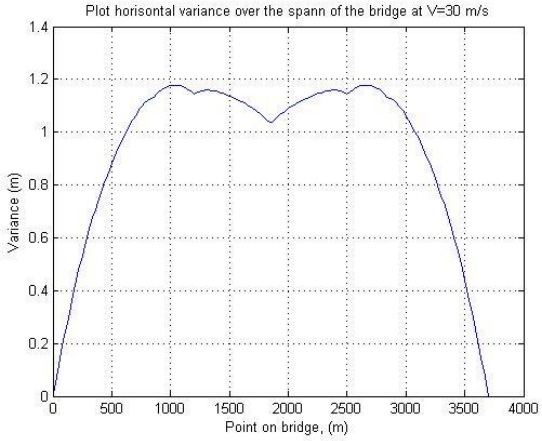
Plot horisontal variance over the spann of the bridge at V=30 m/s
Variance (m)
Point on bridge, (m)

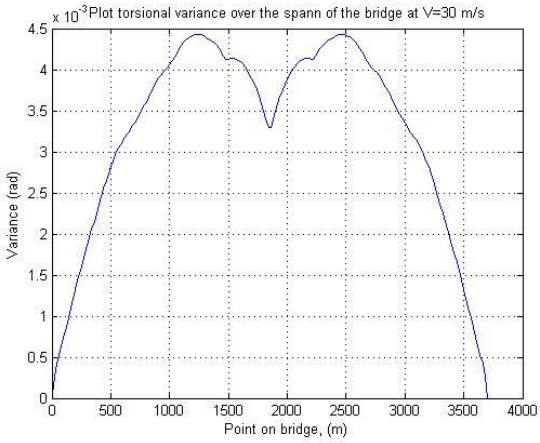
x 10^-3 Plot torsional variance over the spann of the bridge at V=30 m/s
Variance (rad)
Point on bridge, (m)

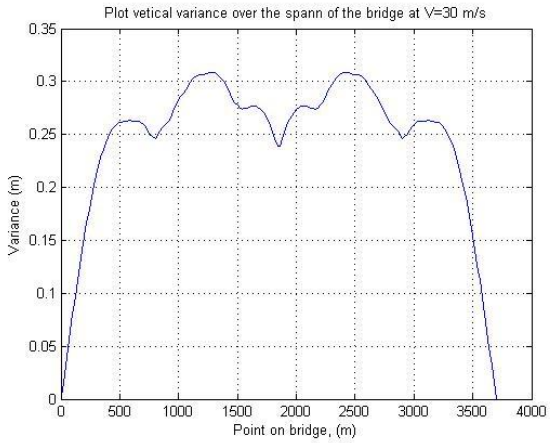
Plot vetical variance over the spann of the bridge at V=30 m/s
Variance (m)
Point on bridge, (m)

B4 Modal frequency-response-function

H

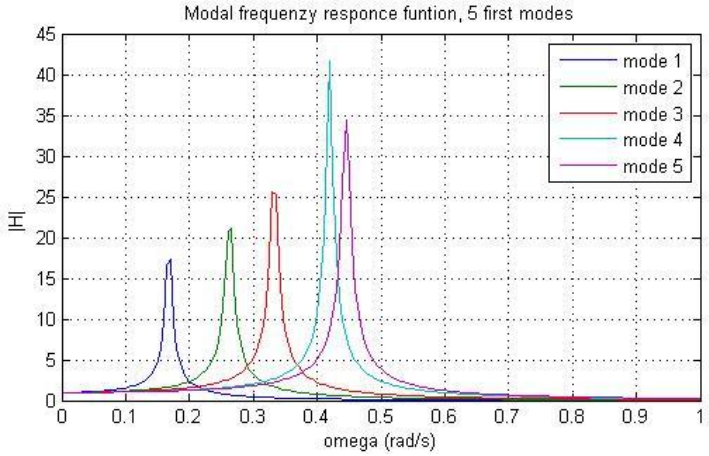

HM

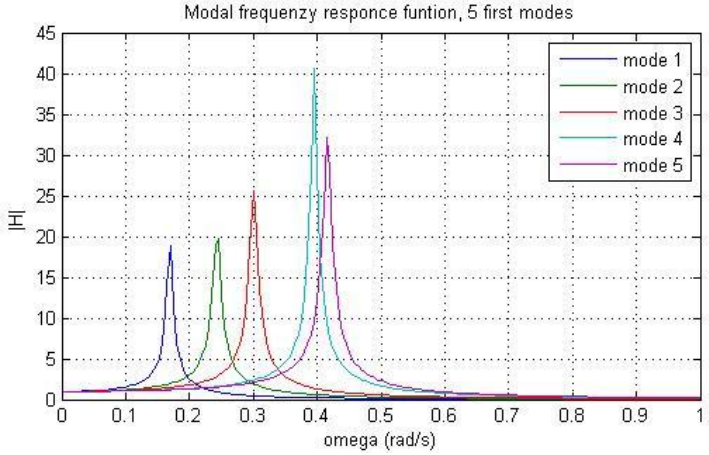

TF

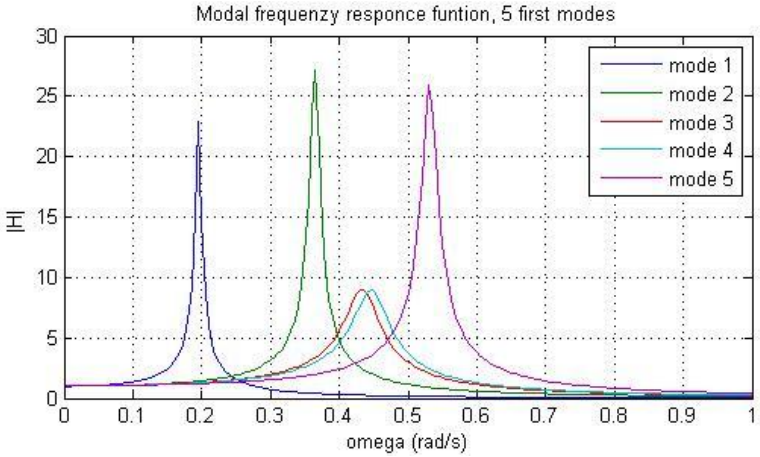

TFM

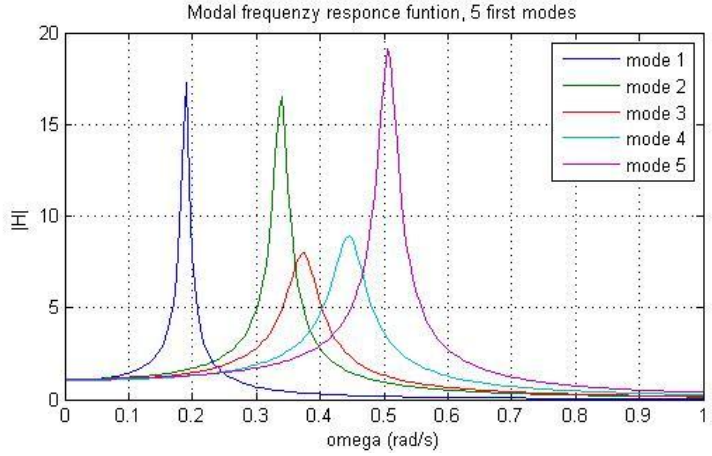
Modal frequenzy responce funtion, 5 first modes
mode 1
mode 2
mode 3
mode 4
mode 5
|H|
omega (rad/s)

B20

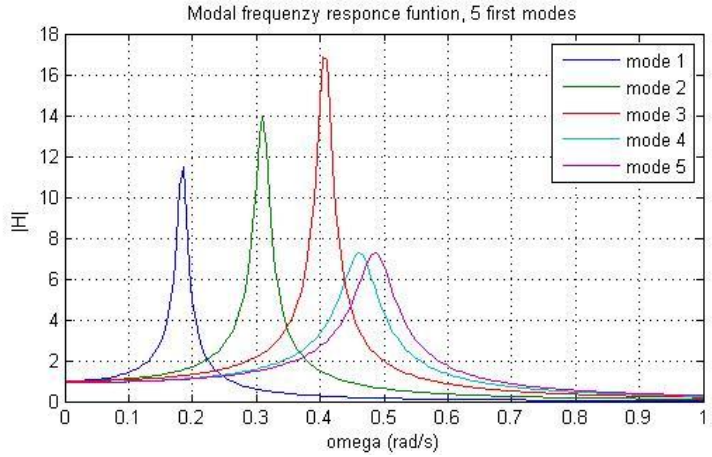
Modal frequenzy responce funtion, 5 first modes
mode 1
mode 2
mode 3
mode 4
mode 5
|H|
omega (rad/s)

B30

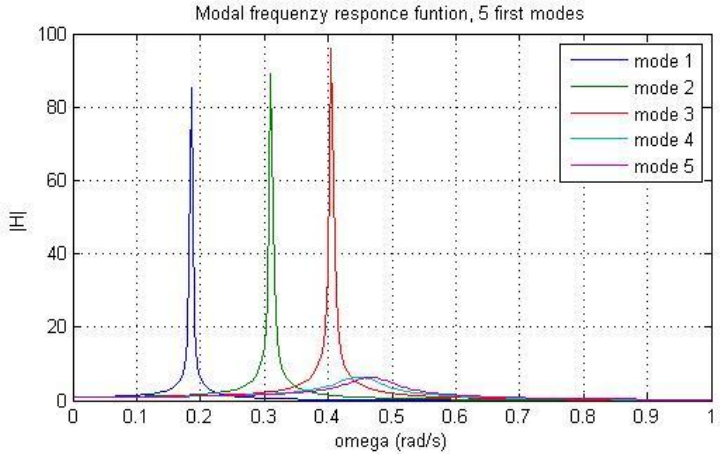
Modal frequenzy responce funtion, 5 first modes
mode 1
mode 2
mode 3
mode 4
mode 5
|H|
omega (rad/s)

B5 Spectral density for the first 5 modes in horizontal direction

H

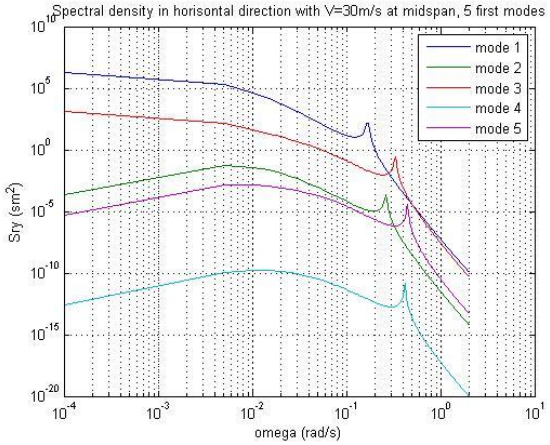

HM

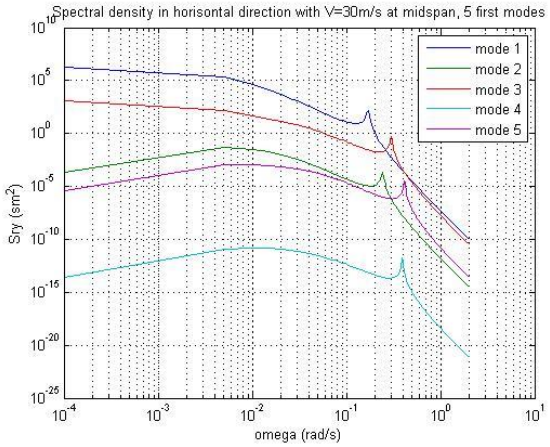

TF

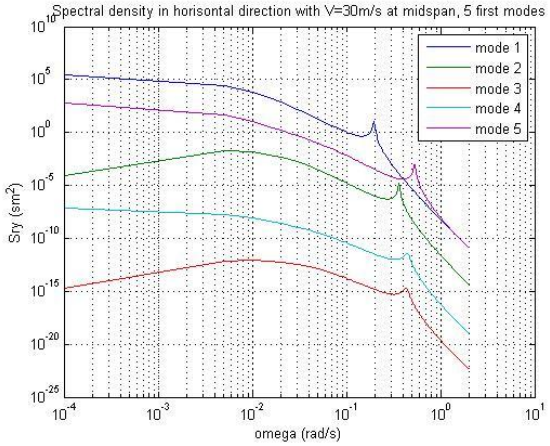

TFM

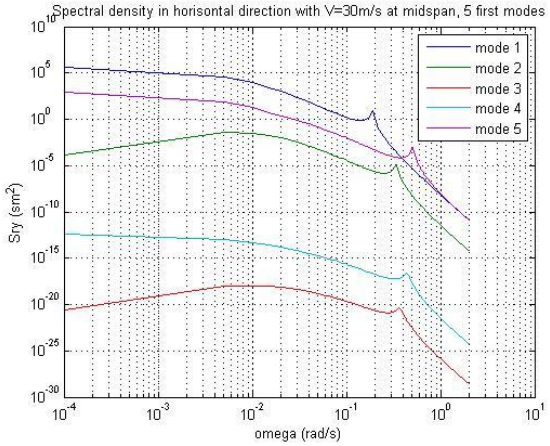
Spectral density in horisontal direction with V=30m/s at midspan, 5 first modes
mode 1
mode 2
mode 3
mode 4
mode 5
Sry (sm²)
omega (rad/s)

B20

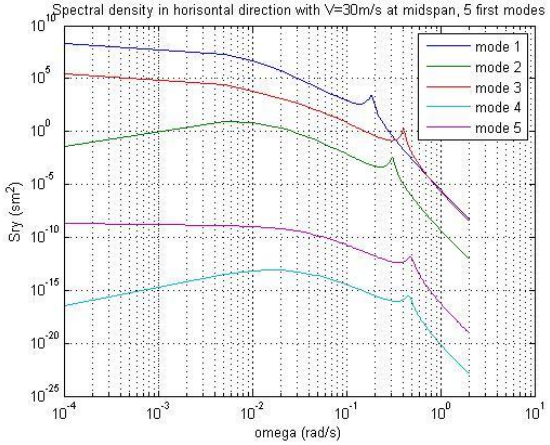
Spectral density in horisontal direction with V=30m/s at midspan, 5 first modes
mode 1
mode 2
mode 3
mode 4
mode 5
Sry (sm²)
omega (rad/s)

B30

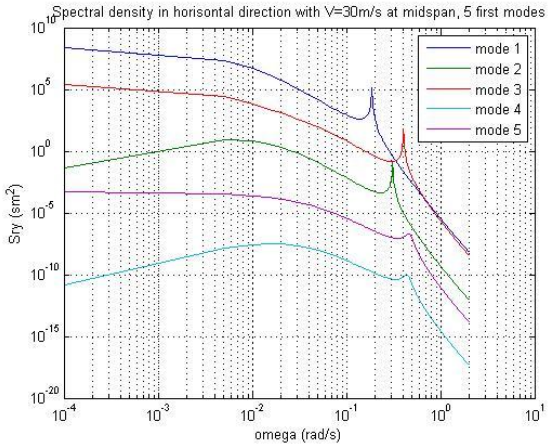
Spectral density in horisontal direction with V=30m/s at midspan, 5 first modes
mode 1
mode 2
mode 3
mode 4
mode 5
Sry (sm²)
omega (rad/s)

B6 comparison of frequency step

Omega=0.5

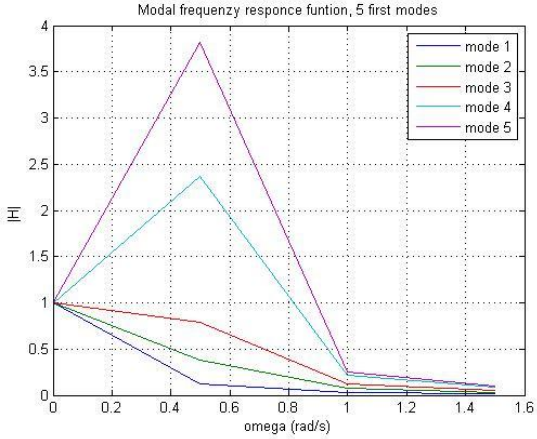

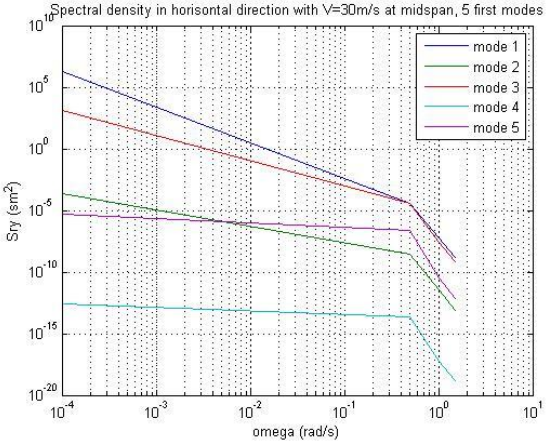

Omega=0.05

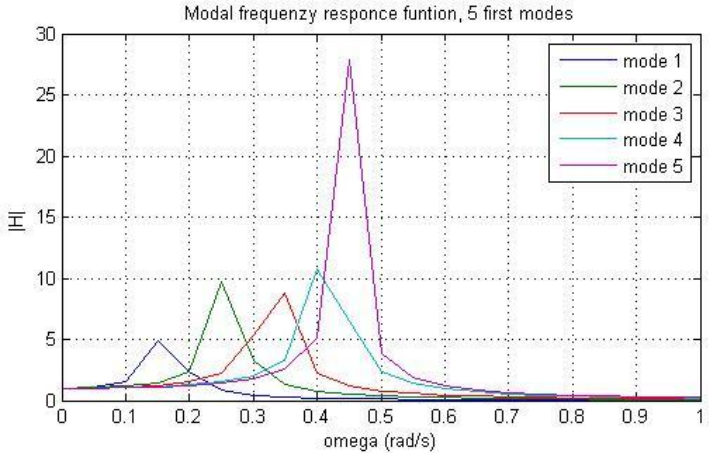

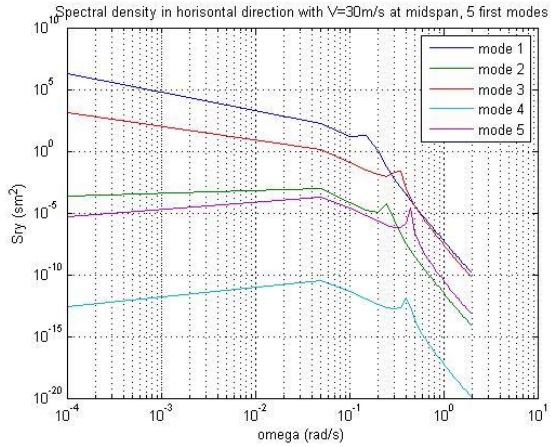

Omega=0.005

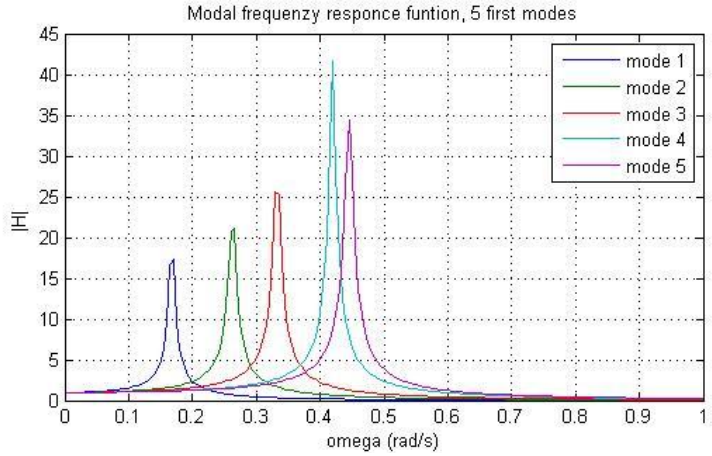

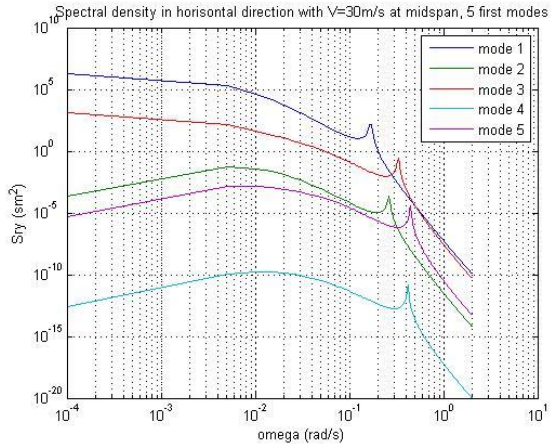

Omega=0.001

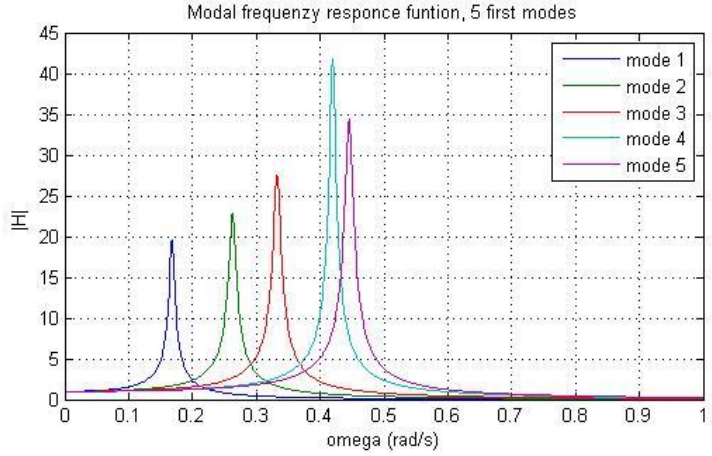

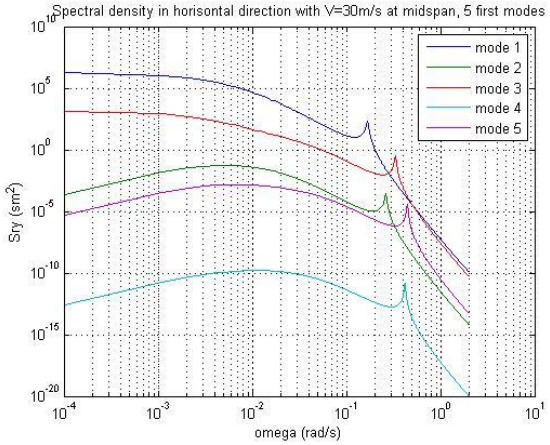
Spectral density in horisontal direction with V=30m/s at midspan, 5 first modes
mode 1
mode 2
mode 3
mode 4
mode 5
Sry (sm²)
omega (rad/s)